

**ELECTROSTATIC ELASTOMER DEVICES FOR
RECONFIGURABLE HIGH-DENSITY MICROFLUIDICS**

by

Meng-Ping Chang

A dissertation submitted in partial fulfillment
of the requirements for the degree of
Doctor of Philosophy
(Mechanical Engineering)
in The University of Michigan
2008

Doctoral Committee:

Assistant Professor Michel M. Maharbiz, Co-Chair
Professor Yogesh B. Gianchandani, Co-Chair
Associate Professor Katsuo Kurabayashi
Associate Professor Shuichi Takayama
Ernest F. Hasselbrink, First Marblehead Corporation

© Meng-Ping Chang
All rights reserved
2008

To my family

ACKNOWLEDGEMENTS

I would like to express my sincere gratitude to those who have provided support and encouragement during my Ph.D study. First and foremost, I want to thank my advisor, Dr. Michel M. Maharbiz, for his guidance and assistance in my research. His great enthusiasm, working ethics and insightful perspective are not only an inspiration but also a model to me. He also made some of my dreams come true.

I thank my committee co-chair, Dr. Yogesh B. Gianchandani, for being there at the critical moment, providing invaluable help and encouragement to me. Special thanks have to go to my thesis committee: Dr. Katsuo Kurabayashi and Dr. Shuichi Takayama, and especially Dr. Ernest F. “Charlie” Hasselbrink, who was my advisor during my early stage of Ph.D career. I am grateful for their advice and help in their precious comments to me. I also want to thank Dr. Daryl R. Kipke for his time, effort, and care during my pre-lim exam. In addition, I want to give my sincere thanks to Dr. Edward T. Zellers for his generous support, gracious encouragement, and wonderful guidance during my first year in Michigan. He was, in effect, my “*Creator Spiritus*”.

Thanks go to Wise/Najafi Laboratory and Neural Engineering Laboratory for assistance in experimental setup. I also want to thank staff of WIMS ERC and SSEL/LNF for creating a superb environment to carry out my research. They are real unsung heroes.

I would like to thank Tushar Bansal for his all-out effort and numerous time working

together to make Chapter 3 possible, co-authorship of the *Lab Chip* article and unselfish sharing; Ruba T. Borno for her generous support being my grammar checker and sincere friendship; Hirotaka Sato for his assistance in experiments, whole-hearted encouragement and memorable every-now-and-then-boogie-woogie time. I also want to give thanks to other fellow *Maharbeans*: Brendan Casey, Taesung Kim, Jaehyun Park, Mike Pinelis, Prashant Padmanabhan, Joay K. Singhal, Joseph Steinmeyer, Gabriel Lavella, Whijae Roh, Patricia M. Pacheco, Chris Berry, Nick Collins, and Abdel Srouji, for all sweet memories.

In no particular order I would like to thank my friends in Michigan: Vincent Lu, Yi-Chung Tung, Chih-Ting Lin, Wen-Lung Huang, Steven Emanuel, Anders Brask, Sheng-Shian Li, Larry Cheng, Taegyun Moon, Gayatri Perlin, Scott Wright, Steve Yin, Pai-Chen Lin, Hui-Chia Yu, Robert Bartz, Greg Sommer, Hsien-Yeh Chen, Chao Yun Fan, Wei-bin Zhu, Tao Li, Chen-Chun Kao, Chia-Yuan Chang, Yong-Song Chen, Yao-Te Huang, Kyusuk Baek, Robert D. White, Sun Min Kim, Niranjan Deo, Yu-Wei Lin, Zeying Ren, Roel Huerta, Neil Welch, Robert Littrel, Erkan Aktakka, Jae Yoong Cho, Lei Cheng, Christine Eun, Scott Green, Naveen Gupta, Tzeno Galchev, Hanseup Kim, Razi Haque, Angelique Johnson, Anurag Tripathi, Willie Steinecker, Judy Zhong, and Jamie Nichols. You all mean a lot to me.

Special thanks go to brothers and sisters in Ann Arbor Chinese Christian Church for their care, sharing, and prayers over the years. May God bless them.

With tremendous gratitude, I would like to thank my parents and brother. Your immeasurable love and support are the sole motivation for me to walk through this long and

winding road. You have always been there cheering and comforting me. Lastly, I want to thank my loving wife, Hsin-Yuan Chen. Thank you for your endless love and unlimited tolerance of my childish temper. You are the wind beneath my wings- without you, I would not make it.

TABLE OF CONTENTS

DEDICATION	ii
ACKNOWLEDGEMENTS	iii
LIST OF FIGURES	ix
LIST OF TABLES	xv
LIST OF APPENDICES	xvi
CHAPTER 1 INTRODUCTION	1
1.1 Motivation	1
1.2 Thesis Objective	3
1.3 Thesis Organization.....	6
CHAPTER 2 LITERATURE REVIEW OF RELATED RESEARCH.....	8
2.1 Polymer Micro Valves	8
2.2 Polymer Micro Pumps.....	15
2.3 Reconfigurable Microfluidics for Large-Scale Integration.....	20
2.4 Conclusion.....	26
CHAPTER 3 RADIO-FREQUENCY ELECTROSTATIC “WET” MICRO ACTUATORS.....	27
3.1 Introduction	27
3.2 Electrostatic Actuation in Water Dielectric.....	28
3.2.1 Pull-in Voltage with Water Dielectric	28
3.2.2 Spring Constant k of a Rectangular Plate.....	31
3.2.3 Residual Stress of Capacitor Plates	32
3.3 Device Concept and Design Strategy	33
3.4 Fabrication.....	36
3.5 Experiment Results	39

3.5.1 Device Actuation and Surface Profilometry of Actuated Devices	39
3.5.2 Power Consumption and Current Draw	41
3.5.3 Applications as Micro Valve and Drug Doser	42
3.6 Conclusion.....	44
CHAPTER 4 PDMS MICRO VALVE AND PERISTALTIC PUMP	45
4.1 Introduction	45
4.2 Device Operation and Design.....	46
4.3 Device Fabrication	50
4.4 Experiment Setup	52
4.4.1 Fluorescent Microscopy and Fluidic Characterization.....	52
4.4.2 Control Circuitry	52
4.5 Results and Discussion.....	54
4.5.1 Valve Performance.....	54
4.5.2 Pumping.....	56
4.5.3 Discussions of System Applicability	57
4.6 Summary and Conclusion	58
CHAPTER 5 RECONFIGURABLE ELASTOMER MICROFLUIDICS.....	59
5.1 Introduction	59
5.2 Device Concept and Design	61
5.3 Fabrication.....	62
5.4 Experiment Apparatus and Control Circuitry	64
5.5 Valve and Pump Performance.....	66
5.6 Reconfigurable Distributed Microfluidics	67
5.6.1 Distributed Valving.....	68
5.6.2 Fluidic Switch.....	70
5.6.3 Mixing of Liquids.....	71
5.6.4 Comparisons with Current Technologies.....	76
5.7 Summary of Contribution.....	77

CHAPTER 6 CONCLUSION.....	78
6.1 Summary of the Thesis Work.....	78
6.2 Future Work Directions.....	81
6.3 Concluding Remarks	85
 APPENDICES	 86
BIBLIOGRAPHY.....	147

LIST OF FIGURES

- Figure 1.1: One of the first micro total analysis systems: a micro fabricated chip for capillary electrophoresis. The chip is bonded by two glass substrates: one with etched channels and the other one as the cover. The dimension of this chip is 15 cm by 4 cm by 1 cm, with a 13.5 cm long micro channel for capillary electrophoresis. Adapted from [1]. 2
- Figure 2.1: Schematic illustration of two configurations of PDMS membrane pneumatic micro valve (adapted from [7]). The bottom displacement chamber is connected to a vacuum/pressure source to actuate the deformable PDMS membrane, opening and closing the valve..... 10
- Figure 2.2: Schematic diagram of a thermo-pneumatic micro valve (adapted from [38]). The actuation chamber was separated from the heater chamber to prevent heat transfer into the fluidic flow.....11
- Figure 2.3: An electromagnetically driven pressure regulating valve (adapted from [39]). This device used a pair of coils with a transmitter coil outside and a receiver coil inside. The power was produced by using magnetic induction to generate sufficient current to drive the pressure regulating valve. 13
- Figure 2.4: Schematic of a piezoelectric polymer valve (adapted from [40]). This actuator was deflected upwards when an electric field was applied. The chamber between the piezo actuator and the valve membrane was filled with a silicone gel. When the valve was closed the silicone gel was at elevated pressure to ensure an effective valve seal. When the actuator deflected upwards, the diaphragm was deflected off the wall and hence opened the valve. 14
- Figure 2.5: Classification of pumps and micro pumps (adapted from [72]). 16
- Figure 2.6: Two reciprocating displacement micro pumps (A) check-valve type and (B) peristaltic type (adapted from [72]). Both these two types of pumps produce pulsatile flow, and the flow rate depends on the pump actuation frequency..... 17
- Figure 2.7: A check-valve silicone diaphragm pump (adapted from [41]). This micro pump could be actuated by external pneumatics or solenoid driver. 18
- Figure 2.8: The schematic of a multi-layered PDMS peristaltic pump (adapted from [5]). The top blue channels are pneumatic control channels and the bottom

	brown channel is fluid flow channel. Peristaltic pumping is achieved by alternating the actuation of pneumatic channels.	19
Figure 2.9:	Conceptual views of electrostatically actuated parylene peristaltic pump (adapted from [30]). The actuation chamber was separated from the fluid channel so that working liquid was isolated from the electric field.	20
Figure 2.10:	A pneumatic powered PDMS large-scale microfluidic integration (adapted from [10]). The fluidic network was integrated with a fluid multiplexor so that the number of required pneumatic control could be reduced.	22
Figure 2.11:	A computerized microfluidic pump and valve powered by Braille display (adapted from [36]). The fabricated PDMS channel was aligned with a refreshable Braille-display system underneath. As the Braille pin actuated, it pressed the above PDMS channel bottom to seal the valve.	22
Figure 2.12:	Electrowetting on dielectric: LEFT: adapted from [69]; RIGHT: adapted from [34]. This kind of device, for a single unit, consists of a pair of electrodes, both of which are insulated by dielectric and hydrophobic layers. Liquid droplets move as the local wetting condition changes. It is possible to build an array of control electrodes to use this device for large scale microfluidic integration.	24
Figure 2.13:	Droplet actuation using thermal-induced Marangoni flow (adapted from [37]). A programmable system for noncontact droplet actuation including a 128-pixel array of resistive heaters suspended above the oil layer.	25
Figure 3.1:	Perspective-view schematic of a plate-spring system for electrostatic pull-in. The top mobile plate is held by a spring while the bottom plate is fixed. The two plates are separated with a gap, g	30
Figure 3.2:	Relative Permittivity of water at different frequencies. Adapted from [91].	31
Figure 3.3:	Conceptual view of a PDMS-based device. The bottom electrode is ITO which is insulated by a layer of oxide. The top electrode is made of chrome-gold, etched into spiral spring to reduce structure stiffness.	34
Figure 3.4:	Fabrication process flow.	36
Figure 3.5:	WL-5150 thickness vs. spinning speed (Solitec spinner).	38
Figure 3.6:	WL-5150 thickness before and after critical point drying. The PDMS thickness reduced 25 % (16 μm to 12 μm) after CPD.	38
Figure 3.7:	Device Actuation. (a) Unactuated PDMS device after sacrificial channel photoresist has been removed. (b) Unactuated PDMS device filled with DI water. Fluorescent ruthenium compound is added for visualization. (c)	

	Actuated PDMS device. Deflection is clearly visible as the dark region. (d) All gold devices after release. (e) All gold devices with DI water and fluorescent compound. (f) An actuated all gold device.	40
Figure 3.8:	RIGHT: Profilometry cross-section along dashed line in Figure 3.7 (a). LEFT: Cross-section profilometry along dashed line in Figure 3.7 (d). Most PDMS channel experienced sagging ($\sim 2 \mu\text{m}$) after release.	40
Figure 3.9:	Deflection vs. voltage plot for all gold and PDMS devices. Pull-in is indicated on each plot with dashed lines.	41
Figure 3.10:	Fluorescent micrograph of devices operated as a micro valve. (a) Microspheres ($0.5 \mu\text{m}$ diameter) mixed with fluorescent solution were loaded in to the micro channel. As the valve was open, the microspheres moved with liquid flow under an unactuated valve. (b) At $t = 50 \text{ s}$ the valve was closed, and the flow stopped. Microspheres were expelled by the valve and accumulated at the valve boundary, as pointed by the arrowhead. (c) As the valve was opened at $t = 100 \text{ sec}$, the liquid flow resumed and the microspheres moved again.	43
Figure 3.11:	Drug Doser. The device can be used as effective drug dosers. (a) An unactuated device (open gap) with an etched hole at its center can behave as an open pore and diffuse chemicals into medium. (b) An actuated valve (closed gap) can close the pore and shut off the diffusion.....	43
Figure 4.1:	Top view of fabricated valve and pump devices. LEFT: a micro valve filled with green water (food color). RIGHT: a three-valve peristaltic pump.	46
Figure 4.2:	Conceptual view of an electrostatically-actuated PDMS micro pump. The middle micro valve is actuated and this is a 010 actuation step (0: unactuated; 1: actuated).	47
Figure 4.3:	Actuation sequence cycle of a peristaltic pump. Images (a)-(f) show the liquid movement in a complete actuation scheme. Red arrows in (a)-(f) indicate liquid in an un-actuated valve. Detailed actuation process of each valve is in figure (g).....	48
Figure 4.4:	Fabrication process flow. Dow Corning® WL-5351 spin-on PDMS ($6.7 \mu\text{m}$) was used to make micro channel structures.	51
Figure 4.5:	Properly (left) and insufficiently (right) cured WL-5351 membrane after solvent soaking. Insufficient UV photo-activation, baking time and temperature resulted in poor cross-linking or reduced film retention.	51
Figure 4.6:	(a) Schematic of experiment setup for liquid flow characterization. The actuation signal is synthesized and switched by pre-programmed USB-interfaced micro controller and optical relay switch. (b) and (c)	

	Photograph of experiment apparatus. The upstream and downstream fluidic networks were built on height-adjustable stages to balance hydrostatic pressure.	53
Figure 4.7:	Circuit diagram for generating the actuation signal for peristaltic pump. For a single switch circuitry, signals of Ports Pi and Pi+1 from BS1 micro controller were always out of phase to ensure the top capacitor plate was either grounded or actuated.....	54
Figure 4.8:	LEFT: open valve (un-actuated). White arrowhead indicates the fluid flow in an open valve. RIGHT: closed valve (actuated). White arrowheads are the microspheres trapped in a closed valve, and black arrowheads are the expelled microspheres piled-up against the valve boundary.	55
Figure 4.9:	Pressure vs. valve leak rate. An actuated valve was able to hold pressure up to ~ 6 psi (39.3 KPa).	55
Figure 4.10:	Pump performance. LEFT: pumping indication by the movement of microspheres. The scale bar is 100 μm . RIGHT: flow rate vs. actuation frequencies. The maximum flow rate was 1 nL/min at 1.6 Hz pumping frequency.....	56
Figure 5.1:	A conceptual view of microfluidic large-scale integration. Each single valve developed previously had a 300 μm by 300 μm area so it is possible to fabricate a chip with more than 10^3 discrete 1 cm by 1 cm valve components.	60
Figure 5.2:	Conceptual view of a reconfigurable microfluidic device built on a glass substrate. The top PDMS-metal membrane with metal flexure and the bottom ITO form the capacitor plate pairs. Each valve component is connected to six other adjacent component and can be electrostatically actuated independently. A valve seat is made by glass wet etching. An insulating oxide layer is deposited on the ITO electrode.....	62
Figure 5.3:	Fabrication flow. A 1 μm glass recess was etched to form a valve pocket.	63
Figure 5.4:	Diagram of experiment apparatus. The upstream and downstream fluidic network was only present for flow rate characterization.....	64
Figure 5.5:	Control circuitry. A user-programmable micro controller (Parallax BS2) with 16 output ports was used to generate the synthesized actuation patterns for each valve component.	65
Figure 5.6:	Valve and pump performance. (a) Top: an open valve filled with blue liquid. Bottom: as the valve closed, the liquid was expelled. (b) Average flow rate versus pumping frequency. The maximum average flow rate was found at 0.4 Hz actuation. After this frequency the flow rate decreased as	

actuation frequency increased. The measured flow rate was on the order of nL/min. (c) Flow rate versus time with 1.11 Hz actuation frequency. Peristaltic pumping generated pulsating flow, as indicated by the positive and negative spikes in the plot. The span between the two negative spikes was exactly the same time span as the actuation period (0.9 second). 66

- Figure 5.7: Single valve circulation actuation. Ruthenium dye was used for fluorescence microscopy. Image A is an un-actuated background image, B – G are each actuation as indicated by the white circle. Image b – g are the background-subtracted images of B – G respectively. Time frame is 150 ms and scale bar is 200 μ m. 68
- Figure 5.8: Pattern of two valve circulation actuation. Two diagonal valve components were actuated simultaneously and followed a counter-clockwise actuation sequence. The timeframe was 150 ms. 69
- Figure 5.9: Pattern of full vertical actuation. Each row of valves was actuated sequentially for 150 ms. 69
- Figure 5.10: Full horizontal actuation from right to left. Time frame was 150 ms. 69
- Figure 5.11: Flow splitting. Valves 1, 3, 5, 7 were operated as two-outlet peristaltic pump. White circles indicate the actuated valve components, while X denotes permanently closed valves (2, 4, 6) as barriers of liquid path. Image (a) – (f) are background-subtracted; numbers denote actuated components. Time frame was 150 ms, and pumping frequency was 1.1 Hz. 70
- Figure 5.12: Fluid being switched to the right. Numbers in each frame denotes the un-actuated valve. The working liquid was blue water. Arrows in image (a) indicates liquid inlet and outlet, and arrowheads in (b) shows leakage between each actuated valve components. Time frame was 150 ms. 71
- Figure 5.13: A single mixing cycle of blue and yellow liquids in the central chamber (valve 7). Blue liquid was filled from valve 3 and yellow liquid from valve 5. Valves 1 and 6 were permanently closed. 72
- Figure 5.14: (a) - (d) fluorescent micrograph of active mixing by actuating diagonal valve pairs periodically. (e) Histogram of normalized light (concentration) intensity. 74
- Figure 5.15: (a) - (d) fluorescent micrograph of passive mixing by pure diffusion. (e) Histogram of normalized light (concentration) intensity. 75
- Figure 5.16: Normalized average concentration vs. time. 75
- Figure 6.1: An example of reconfigurable VLSI microfluidic device with multiple inlets and outlets for samples/buffers (red, green, and blue lines) and

wastes (grey lines). An integrated device has the capability to manipulate multiple liquids simultaneously, mix selectively, and transport pre-mixed liquids to different position for parallel analysis. 84

Figure 6.2: A conceptual view of reconfigurable liquid surface acoustic sensor (SAW) sensor array. The SAW sensor in the call-out is a one-port design..... 84

LIST OF TABLES

Table 2.1	Classification of Micro Valves (adapted from [67])	10
Table 3.1	Material Properties of Dow Corning® WL-5150 (adapted from [26]).....	35
Table 3.2	Device Design Parameters	35
Table 4.1	Material Properties of Dow Corning® WL-5351 (adapted from [26]).....	49
Table 4.2	Device Design and Dimensions	50
Table 4.3	Comparison with Parylene Systems in [30].....	58
Table 5.1	Device Operation and Actuation Patterns	67
Table 5.2	Comparisons with Other Reconfigurable Microfluidic Systems	76

LIST OF APPENDICES

APPENDIX A	ELECTROKINETIC PUMPS	87
APPENDIX B	PULL-IN VOLTAGE WITH WATER DIELECTRIC	129
APPENDIX C	FABRICATION FLOW AND EXPERIMENTAL PROTOCOL	131

CHAPTER 1

INTRODUCTION

1.1 Motivation

The concept of Micro Total Analysis Systems (MicroTAS, μ TAS), sometimes also known as lab-on-a-chip systems, refers to microsystems capable of performing efficient chemical sampling, transport, and analysis [1, 32, 33], through control and manipulation of fluidic flows at a sub-millimeter scale [19]. This idea was originally applied mainly to analytical chemistry (e.g. the capillary electrophoresis chip shown in Figure 1.1), but recently has broadened to the area of biological analysis due to large research and commercial interests. This technology is receiving intense scientific and engineering attention because (1) it is an interdisciplinary technology integrating knowledge in chemistry, biotechnology, engineering, material science and micro fabrication techniques, (2) it has wide applications in biological, chemical analysis and synthesis (3) the size of a single chip is much smaller than an ordinary laboratory equipment, and the cost can significantly decrease by mass production of micro devices. In addition, advances in microelectromechanical systems (MEMS) and microfluidics also result in rapid growth of μ TAS.

Among various developments in μ TAS, very-large-scale integration (VLSI) of microfluidics is by far one of the most challenging tasks. This is because although numerous micro pumping technologies have been developed, there is still no simple solution to in-

tegrate large number micro pumps and valves into a single microfluidic chip without the need for cumbersome external components. Some of the hurdles come from fabrication integration; some techniques have other incorporation issues such as bio-compatibility or involved chemistry of working liquids. This question becomes more problematic as the system scale advances toward high-density microfluidic integration. For a typical large-scale integrated microfluidic system, there usually exist thousands of micro valves [10] that have to be controlled individually. For such large number of independent devices, the only way to control is computerized automation, which adds another difficulty in integration of interface between the chip and control mechanism.

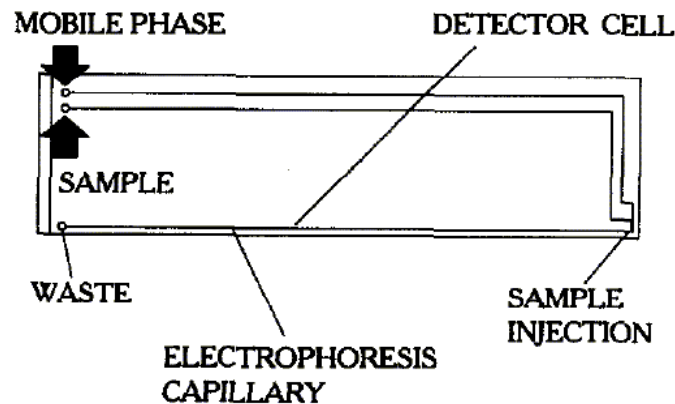


Figure 1.1: One of the first micro total analysis systems: a micro fabricated chip for capillary electrophoresis. The chip is bonded by two glass substrates: one with etched channels and the other one as the cover. The dimension of this chip is 15 cm by 4 cm by 1 cm, with a 13.5 cm long micro channel for capillary electrophoresis. Adapted from [1].

The current research work related to large-scale microfluidic integration can be divided into three major categories according to its actuation mechanism: external pneumatic control [5, 10], external mechanical power [36], and droplet transport by surface

tension gradients such as electrowetting on dielectric (EWOD) [8, 34, 35] and thermo-induced Marangoni flows [37]. These technologies have focused on either (1) the scaling and modification of conventional pneumatically-driven elastomer microfluidics or (2) the development of electrically or magnetically addressable fluidic components and systems. The first category of devices has arguably come the farthest through advances in component design, multiplexing and pneumatic circuits [5, 9, 10]. Modern pneumatic elastomer microfluidic systems have thousands of micro scale valves, driven by off-board high pressure pneumatics [5, 10]. Non-pneumatic components have been developed, but they suffer largely from expensive or time-consuming processing [84], hand-assembly [36], poor scalability [36, 37], performance degradation [8, 34, 35] or new materials [84]. A survey of background research works, together with issues discussed above, can be found in Chapter 2.

1.2 Thesis Objective

With all these challenges and needs in mind, this thesis work is aimed at developing a computerized reconfigurable microfluidic system for very-large-scale integration. We first investigated component level devices (Chapter 3), exploring appropriate working mechanisms and materials, developing micro fabrication techniques, and characterizing device performance. We then investigated computerized control and large-scale reconfigurable microfluidic integration of multi-valve system.

Electrostatic, electromagnetic and piezoelectric are the most commonly used mechanism for micro actuators and both operations are electromechanical, so no chemi-

cal reaction is involved. While electromagnetic and piezoelectric actuations are limited by the material choices, electrostatic is applicable for all conductive materials with a dielectric gap. Therefore, the problem becomes how to replace those off-chip pneumatic controls with on-chip electrostatic power.

Among existing polymer materials commonly used for microfluidic devices, polydimethylsiloxane (PDMS), an organic elastomer, has become the most used one because of its easy handling processes and excellent material properties. PDMS is usually processed using a fast prototyping process called “soft lithography” [83], a technique based on replica molding of elastomeric materials. PDMS precursors can also be spun coated onto a substrate and then cured to form a thin film. Material wise, PDMS is transparent to visible light and some UV (< 300 nm wavelength); this allows for laser optical fluidic measurements. PDMS possesses a low Young’s modulus (0.75 MPa – 360 MPa) but a high maximum strain ($\sim 40\%$); a high dielectric strength (3.3 V/ μm at 1 MHz), high gas permeability, high compressibility and low chemical reactivity. PDMS also has very good adhesion strength for bonding with a glass substrate.

Based on these observations, we developed an electrostatically-actuated reconfigurable PDMS microfluidic system that requires no external pneumatics and is free from involving chemistry for large scale integration. The individual objectives of this thesis work can be categorized as:

1. *To realize low voltage electrostatically-actuated micro actuator for ‘wet’ environment:* Electrostatic actuation is widely used in dry MEMS applications, but it has not received much attention for ‘wet’ applications due to electrical double

layer (EDL) screening of electrostatic force and possible involved electrochemistry. For sensing needs frequency dependence of liquid dielectric properties has been applied for years [89, 90, 92], but for micro actuators it was not reported until recent research works [14, 15, 22], demonstrating that it is possible to use a low voltage AC signal in MHz range to avoid EDL screening. This issue is further discussed in Chapter 3. A new fabrication technique has to be developed to make traditional MEMS fabrication compatible with PDMS process.

2. *To design, fabricate, and characterize electrostatic micro valves and pumps:* This work is to develop electrically-actuated PMDS valves and peristaltic pumps for liquid transport. The valves and pumps have to facilitate low power consumption and low actuation voltage (10-20 V) integration with on-chip electronics for portable microfluidics.
3. *To produce an integrated reconfigurable elastomer microfluidic system for high-density application:* The ultimate goal of this thesis work is to develop a new platform for μ TAS microfluidics: electrostatically-actuated reconfigurable distributed elastomer microfluidics for high-density applications. This reconfigurable microfluidic system requires no external pneumatic connections to operate and is scalable for large scale integration. Moreover, the microfluidic system can perform many programmable manipulations for rapid parallel analysis.

1.3 Thesis Organization

This thesis will focus on electrostatically-actuated PDMS micro actuators (basic unit) and its integration of micro valves, micro pumps (individual components) and reconfigurable high-density microfluidics (integrated systems). The contents of the following chapters include:

Chapter 2 -Literature Review of Related Research: This chapter reviews previous research related to this thesis with a particular focus in (1) polymer micro valves and pumps, and (2) reconfigurable high-density microfluidics.

Chapter 3- Electrostatic PDMS micro actuator: This chapter presents electrostatic actuation in a wet environment utilizing radio-frequency (RF) electrostatic force to avoid electrical double layer screening and electrode polarization. Careful geometry design was conducted to make the pull-in voltage low enough to prevent involved electrochemistry. Experiment results successfully demonstrate devices with water dielectric could be actuated by radio-frequency electrostatic force. Two applications of this device as micro valves and drug dosers are also introduced.

Chapter 4- Electrostatically-Actuated PDMS Micro Valves and Peristaltic Pumps: This chapter introduces integration of the PDMS actuator developed in Chapter 2 into discrete micro valves and peristaltic pumps. A new improved design was made by using a thinner PDMS (Dow Corning® WL-5351) so that the dimension of the device was reduced by 75% volumetrically. Characterizations of fabricated micro valves and pumps are presented and the results compared well with previous works [30].

Chapter 5- Electrostatic reconfigurable PDMS microfluidics: This chapter presents an electrostatic reconfigurable microfluidic system that is capable of doing assorted liquid movement manipulations such as distributed valving, fluidic switching, and mixing of liquids. The proposed microfluidic system requires no external pneumatic connection for operation which is a prominent advantage when grouping numerous discrete micro valves for large scale integration.

Chapter 6- Conclusion and outlook: This chapter summarizes the achievements of this thesis and provides ideas of possible future works.

In addition to electrostatic PDMS microfluidic actuators presented in the main text, a research work on electrokinetic pumps is presented in Appendix A. Electrokinetic pumping is a commonly used microfluidic transport technology especially for drug delivery purposes. This appendix outlines fundamental theories, application hurdles such as electrolysis and pH drift and potential solutions.

CHAPTER 2

LITERATURE REVIEW OF RELATED RESEARCH

This chapter surveys background research works related to the main theme of this thesis. This literature review starts with micro valves and followed by micro pumps, with a particular focus in polymer-based devices. Finally, we review several reconfigurable microfluidic systems for large-scale integration.

2.1 Polymer Micro Valves

A valve is a mechanical device that starts, stops, checks, and regulates fluidic flow (liquid, gas, or slurry) by opening, shutting, and partially obstructing one or more ports or passageways [42]. The first miniaturized valve, reported by Terry *et al* in 1979 [43], was an electromagnetic gas valve built on a silicon substrate for chromatographic air analyzer. The micro valve technology grew rapidly after the 1980's due to advances in micro fabrication techniques and MEMS technology, and has become a very important on-chip element for microfluidic devices.

Several parameters and criteria can be used to characterize a valve depending on the applications [44]. First, a valve needs to have a very low flow resistance R_{hyd} when open for free flow and very high or infinite resistance when closed. The ratio of flow resistance

in closed mode and open mode, termed *diodicity*, should to be very large for a good valve. In addition, the dead volume, defined as the volume of stagnant liquid when a valve is open, needs to be minimized. A dead volume tends to trap gas bubbles which not only adds compliances to the fluidic network but causes a possibility to stop the flow in the system.

Currently micro valve technology can be classified into two major categories: active and passive valves [67]. A classification of micro valves is tabulated in Table 2.1. An active valve uses external power for active operation to open and close, while a passive valve, mostly a check valve, does not have an active actuation function and is passively controlled by the pressure difference according to the direction of fluidic flows. The most common operation mechanisms for active micro valves are pneumatic, electromagnetic, piezoelectric, thermal pneumatic and electrostatic actuation. This section presents an overview of various miniaturized valve technologies with a particular focus in polymer-based active micro valves.

Pneumatic micro valves use volume expansion or contraction caused by external pressure sources, usually integrated with electrically-controlled solenoid valves, to deflect an elastic membrane to seal or open a micro chamber or channel. This elastic membrane can be made by micro fabricated silicon [45, 46, 47], spin-on PDMS [5, 7, 48-52], and other polymer materials such as think latex membrane [53], silicone rubber [54], and 3M tape [55]. Figure 2.1 shows the schematic of the pneumatic micro valve in reported by Grover *et al* [7]. The elastomer diaphragm was made of PDMS sandwiched by two etched glass substrates. Two designs, a three layer structure and a four layer structure, were presented. When the displacement chamber, as indicated in Figure 2.1, was under

Table 2.1
 Classification of Micro Valves (adapted from [67])

Categories			
Active	Mechanical	Magnetic	External magnetic fields Integrated magnetic inductors
		Electric	Electrostatic Electrokinetic
		Piezoelectric	
		Thermal	Bimetallic Thermopneumatic Shape memory alloy
		Bistable	
	Non-mechanical	Electrochemical	
		Phase change	Hydrogel Sol-gel Paraffin
		Rheological	Electro-rheological Ferrofluids
	External	Modular	Built-in Rotary
		Pneumatic	Membrane In-line
Passive	Mechanical	Check valve	Flap Membrane Ball In-line mobile structure
		Capillary	Diffuser Abrupt Liquid triggered Burst Hydrophobic valve
	Non-mechanical		

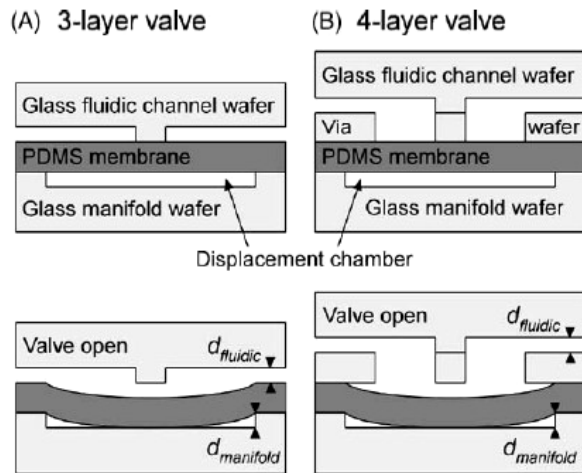


Figure 2.1: Schematic illustration of two configurations of PDMS membrane pneumatic micro valve (adapted from [7]). The bottom displacement chamber is connected to a vacuum/pressure source to actuate the deformable PDMS membrane, opening and closing the valve.

vacuum, the PDMS membrane deflected and opened the valve. The actuated device had a less than 10 nL dead volume, provided 380 nL/s flow rate at 30 kPa pressure, and held up to 75 kPa fluid pressure.

Volume change as a result of the thermal expansion of air was also applied to deform valve diaphragms. Heat was generated by Joule heating from a local thermal heater made by micromachined metal causing an increase in the temperature of the micro chamber. This type of valve has found applications mostly for gas flow. A typical thermal pneumatic micro valve, reported by Takao *et al* [38], is shown in Figure 2.2. In their design, they separated the drive chamber and thermal chamber to prevent direct heat transfer from the micro heater to the flow channel. The PDMS membrane functioned not only as the valve diaphragm but also the adhesion layer between the glass and silicon substrates. Leakage rate was reported to be less than 1 $\mu\text{L}/\text{min}$ at 30 kPa. Other PDMS based thermopneumatic micro valves were reported by Baechi *et al* [56] and Kim *et al* [57].

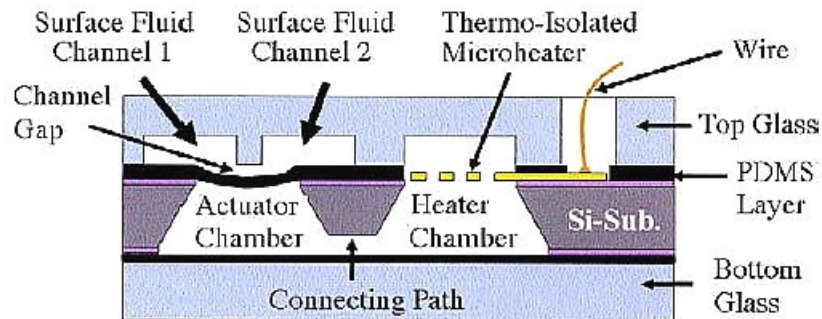


Figure 2.2: Schematic diagram of a thermo-pneumatic micro valve (adapted from [38]). The actuation chamber was separated from the heater chamber to prevent heat transfer into the fluidic flow.

Electromagnetic actuation is another commonly used mechanism for micro valves. It uses solenoid coils connecting to the valve diaphragm to generate electromagnetic force to actuate the membrane. The first micro valve, developed by Terry *et al*, belongs to this family. Some magnetic micro valves integrate with permanent magnets to increase actuation force and reduce power consumption. Most magnetic valves use metal as mechanical moving parts, such as nickel-iron respectively by Yanagisawa *et al* [59], Choi *et al* [60], and Shikida *et al* [61], nickel by Oh *et al* [62], iron by Fu *et al* [63], and gold by Meckes *et al* [64]. As for polymer based magnetic valve, Figure 2.3 shows a permanent magnet coupled magnetic PDMS pressure regulating valve developed by Bae *et al* [39]. The membrane deflection was controlled by supplying current pulse, resulting in modulation of pressure release rate. A 2.3 kPa pressure was obtained with a supplied 60 mA current. Beside membrane based magnetic micro valves, Oh *et al* [58] developed a miniaturized pinch-type valve. This pinch-type valve, utilizing a solenoid magnetic actuator and spring plunger with a silicone tube, had excellent characteristics of no detectable leakage flow up to 200 kPa and zero dead volume.

Piezoelectricity is a phenomenon in which mechanical stress (and corresponding strain) results when a material is subjected to an electric field; such materials are known as *piezoelectric*. Usually these piezoelectric materials are crystals such as quartz or lithium niobate ($LiNbO_3$). Piezoelectric actuation is widely used in micro pump technologies. Piezoelectric actuation is capable of generating very large stresses but the stroke is, on the contrary, very limited. Shao *et al*, using silicone rubber, developed a piezoelectric polymer micro valve [40] as shown in Figure 2.4. The reported dead volume was less than 6 nL and the response time was less than 1 ms for gas and liquid flows. They used a

silicone rubber layer applied by a stamping technique to promote the sealing of the valve and define the assembly gluing area. The maximum flow through the valve was 70 sccm nitrogen at a pressure difference of 50 kPa. In addition, Stehr *et al*, have developed a VAMP (Valve And Micro Pump) device for active valve and both forward and reverse pumping [65].

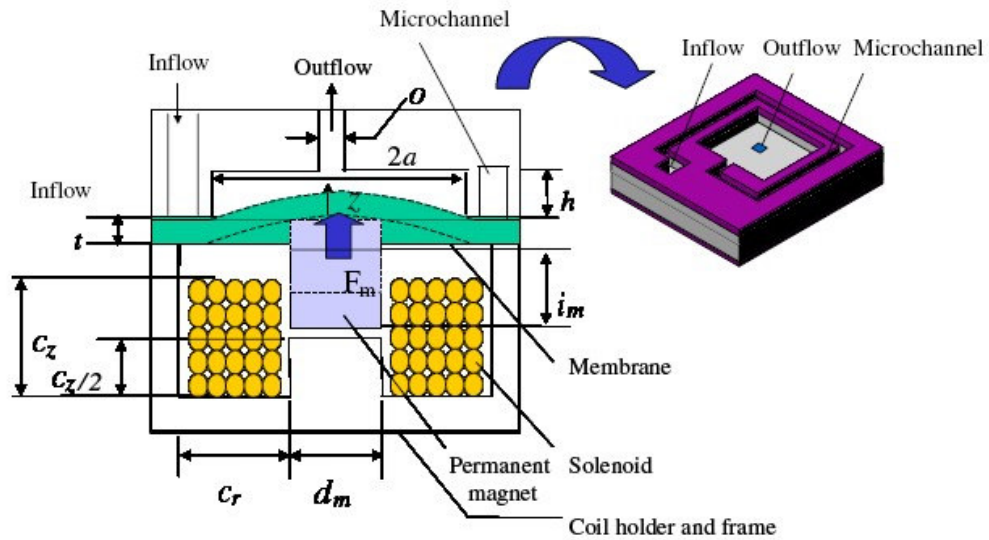


Figure 2.3: An electromagnetically driven pressure regulating valve (adapted from [39]). This device used a pair of coils with a transmitter coil outside and a receiver coil inside. The power was produced by using magnetic induction to generate sufficient current to drive the pressure regulating valve.

Tamanaha et al [66] has developed a PDMS valve actuated by an array of cantilevers operated by shape memory alloy (SMA) wires. This valve, capable of generating 2.35 N of force with a displacement of 406 μm , operated like pinch-type valves and required no micromachining to fabricate. There are some other types of active micro valves operated

by different driving mechanisms such as electrostatic and bimetallic actuation, both of which do not have any literature reporting any integration with polymer materials. Electrostatic actuation, a commonly used valve mechanism, is a field that needs to be more deeply explored. A very informative review of micro valves is reported by Oh *et al* [67].

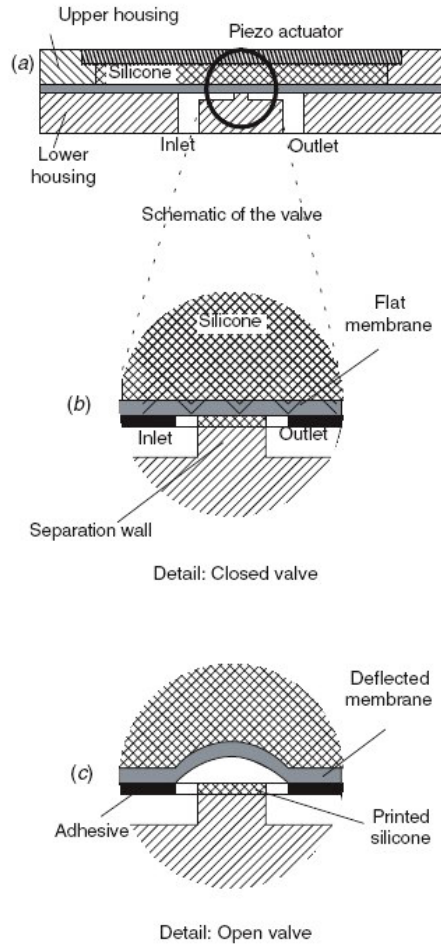


Figure 2.4: Schematic of a piezoelectric polymer valve (adapted from [40]). This actuator was deflected upwards when an electric field was applied. The chamber between the piezo actuator and the valve membrane was filled with a silicone gel. When the valve was closed the silicone gel was at elevated pressure to ensure an effective valve seal. When the actuator deflected upwards, the diaphragm was deflected off the wall and hence opened the valve.

2.2 Polymer Micro Pumps

A pump is a device that raises, transfers, delivers, or compresses fluids (liquid, gas, slurry) from a low pressure location to a higher pressure location [70]. One of the first miniaturized pump devices was reported by Smits [71], which was designed for insulin drug delivery to replace daily injection syringes for diabetic patients. This micro pump, fabricated on a silicon substrate, employed piezoelectric actuation of three valves operating peristaltically. There has since been much progress. By their operation principles, micro pumps can be generally classified into two major categories [72]: (1) displacement pumps: exerting forces directly on working fluid by one or more moving parts (diaphragms; pistons) and (2) dynamic pumps: adding energy to working fluid continuously to increase its pressure or momentum directly. A classification of micro pumps is presented as Figure 2.5. This section aims to review these miniaturized pumping technologies, particularly focusing on polymer-based micro pumps.

Among the displacement micro pumps, the majority of reported work belongs to the family of reciprocating displacement micro pumps that periodically actuate moving boundaries to exert pressure on working fluids. The flow rate of displacement micro pumps is also related to the actuation frequency. This moving boundary is normally an edge-fixed plate or a diaphragm made of micromachined silicon, glass, or polymer materials. The pump diaphragm can be driven by piezoelectric, electromagnetic, pneumatic or thermopneumatic, and electrostatic actuation. Two representative operation schemes of reciprocating displacement micro pumps are check-valve micro pumps and peristaltic pumps, as shown in Figure 2.6 (A) and (B) respectively. A check-valve type micro pump has two modes: discharge mode and suction mode. During the suction stroke, the dia-

phragm actuates causing expansion of the pump chamber, opening the inlet valve and drawing working fluid in. During the discharge stroke, the pump chamber contracts, expelling working fluid through the outlet valve. On the other hand, operation of a peristaltic pump typically has three phases with six modes: (100) → (110) → (010) → (011) → (001) → (101), where 1 means an open valve and 0 means a close valve. This scheme is also known as 120 degree pattern [5].

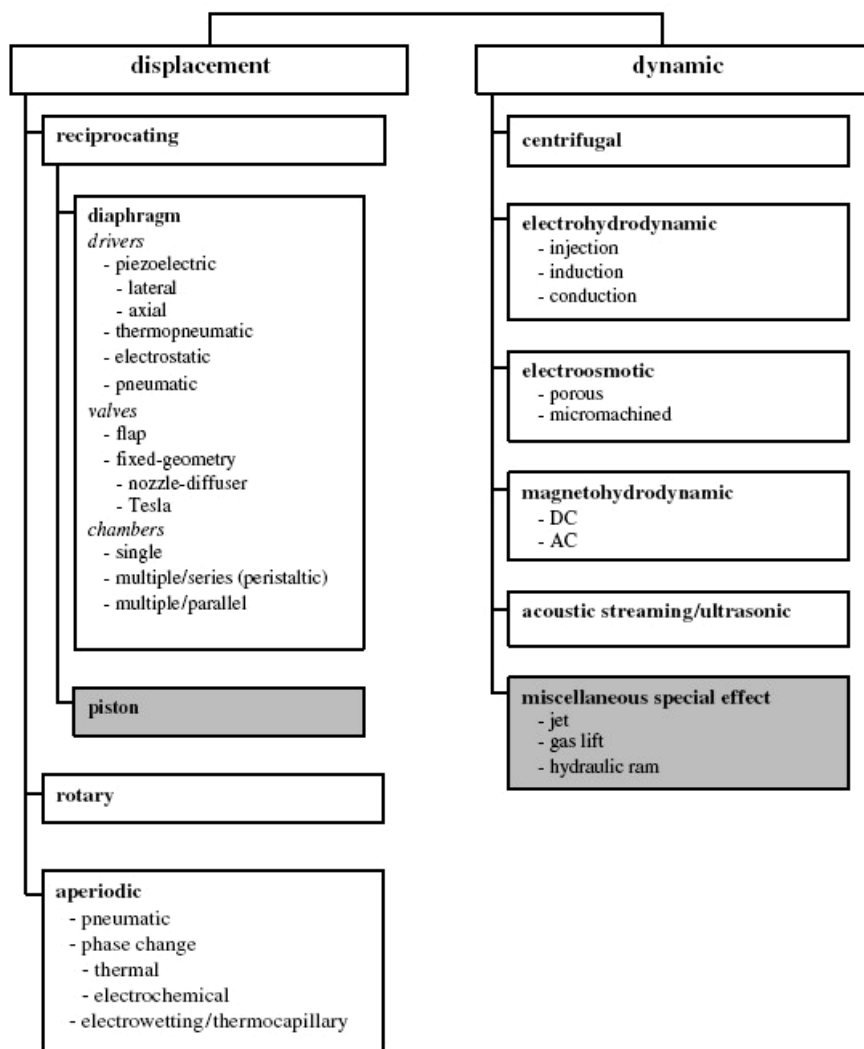


Figure 2.5: Classification of pumps and micro pumps (adapted from [72]).

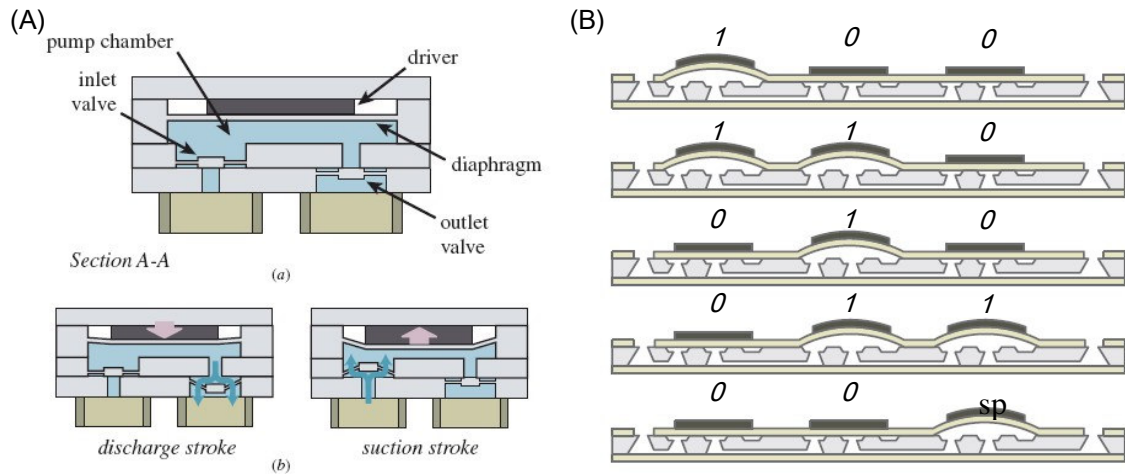


Figure 2.6: Two reciprocating displacement micro pumps (A) check-valve type and (B) peristaltic type (adapted from [72]). Both these two types of pumps produce pulsatile flow, and the flow rate depends on the pump actuation frequency.

Meng *et al* presented a two check-valve pump [41] using silicone rubber as the pump diaphragm that can be actuated by either external pneumatics or solenoid drivers. The schematic is shown in Figure 2.7. Water flow rates of 13 ml/min and a maximum back pressure of 5.9 kPa were reported with external pressure sources. When using a solenoid driver, flow rates of up to 4.5 ml/min and a maximum back pressure of 2.1 kPa have been demonstrated. On the other hand, Unger *et al* has demonstrated a pneumatic peristaltic pump [5] with a multi-layer elastomer structure, as seen in Figure 2.8. The top channels were for external pneumatic controls, while the bottom channels were for fluid flow. When the control channel was pressurized, it expanded and sealed the liquid channel underneath. The dimension of each single micro valve was 100 μm by 100 μm (overlapped area of the control and fluid channel) and the channel height was 10 μm . The

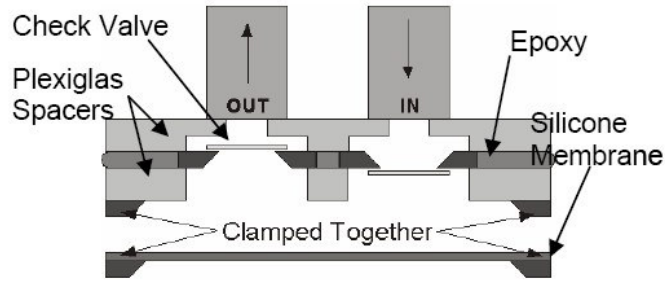


Figure 2.7: A check-valve silicone diaphragm pump (adapted from [41]). This micro pump could be actuated by external pneumatics or solenoid driver.

applied air pressure was 50 kPa. This device had a 140 nL/min maximum flow rate. Grover *et al* demonstrated a self-priming PDMS diaphragm pump with a flow rate ranging from 1 to 100 nL/s and 42 kPa pump pressure [7]. Berg *et al* presented a two-stage PDMS peristaltic micro pump [73] actuated by off-chip compressed nitrogen sources. They also found out that two stage peristaltic pumping generate $2/3$ pressure head of that generated by a normally three-valve counterpart, and could be used for low pressure applications.

A surface micromachined electrostatically-actuated micro peristaltic pump is reported by Xie *et al* [30] based on the multi-layer parylene technology, as shown in Figure 2.9. This micro pump isolated the pumped fluid from the electric field. Electrostatic actuation of the parylene membrane used both DC and 20 Hz voltages to generate a three phase peristaltic sequence. A maximum flow rate of 1.7 nL/min and an estimated pumping pressure of 1.6 kPa were demonstrated at 20 Hz phase frequency.

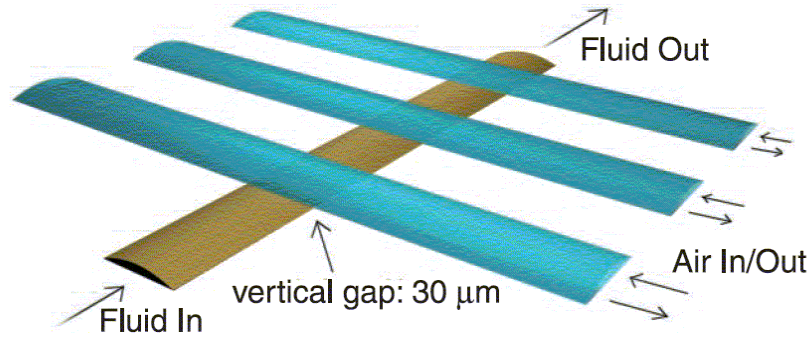


Figure 2.8: The schematic of a multi-layered PDMS peristaltic pump (adapted from [5]). The top blue channels are pneumatic control channels and the bottom brown channel is fluid flow channel. Peristaltic pumping is achieved by alternating the actuation of pneumatic channels.

Wego *et al* presented a micro pump based on printed circuit board technology driven by thermopneumatic actuation [74]. This pump had two passive check valves and one pump chamber. Due to the large deflections of the polyimide membrane, the device could pump liquids even with gas bubbles. A maximum flow rate of 530 ml/ min and a back-pressure of 119 mbar were reported with an actuation frequency of 1 Hz. Schomburg *et al* also used polyimide as the pump diaphragm material [75]. Other thermopneumatic micro pumps using polymer materials include: silicone rubber by Yoon *et al* [76] and parylene/silicone rubber by Grosjean *et al* [77].

Among other polymer-based micro pump technologies, an electromagnetically actuated pump has been demonstrated by Boehm [78], and a low-voltage surface-tension driven pump was reported by Yun *et al* [79], both of which used silicone rubber. For mi-

cro pumps made by silicon or other materials, several comprehensive reviews of micro pumps are available [72, 80, 81, 82].

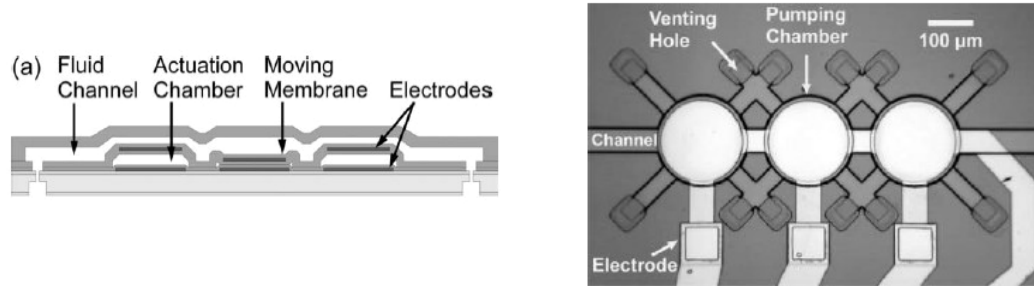


Figure 2.9: Conceptual views of electrostatically actuated parylene peristaltic pump (adapted from [30]). The actuation chamber was separated from the fluid channel so that working liquid was isolated from the electric field.

2.3 Reconfigurable Microfluidics for Large-Scale Integration

The large-scale integration of microfluidic systems was essentially inspired by VLSI electronics technology, a process of integrating thousands of transistors into a single micro fabricated chip. If we compare the component level devices of these two systems (electronic and microfluidic), the transistor, arguable the most important invention in the 20th century [68], is in a direct analogy to discrete micro valves that switch and regulate fluidic flow. Moreover, with the developments of micro fabrication techniques and new materials it is now possible to manufacture a true large-scale integrated microfluidic system composed of thousands of micro valves [10] that can be controlled independently. This section presents an overview of several integrated microfluidic systems that has been or has potential to be suitable for VLSI microfluidics.

Current research works developed for the large-scale microfluidic integration purpose can be classified into two categories: manipulations of continuous liquid columns [9, 10, 36] and manipulations of liquid droplets [8, 34, 35, 37]. The droplet-based microfluidic system is also known as *digital microfluidics* because it controls discrete droplets. Systems aiming for controlling liquid columns usually consist of an array of micro actuators that can be actuated independently to perform valve actuation or integrated peristaltic pumping in the region of interest. Droplet systems use local surface tension gradients generated by various means, such as electrowetting or thermal-induced Marangoni effect, to create a local pressure difference [35] to transport a single droplet.

Figure 2.10 presents a pneumatic large-scale integrated microfluidic systems developed by Thorsen *et al* [10]. The fabricated microfluidic chip, which is an multi-layered elastomer structure, used external pneumatic for operation control [5]. This device contained fluidic networks with thousands of micromechanical valves and hundreds of individually addressable chambers. A fluidic multiplexor, made by an array of binary valve patterns, allowed for complex fluid manipulations with a minimal number of inputs so that the processing power of a network increases exponentially (order of 2^n). This integrated microfluidic network could be used to construct a microfluidic analog of a comparator array and a microfluidic memory storage device.

Gu *et al* has demonstrated a computerized Braille-display powered micro pump and valve system [36], as shown in Figure 2.11. They used a reconfigurable Braille display, with a grid of 320 vertically moving pins, to power integrated pumps and valves through localized deformations of channel networks made of elastic silicone rubber (PDMS). The channels in the PDMS chip were aligned right above corresponding Braille pins. Actu-

ated pins were displaced upward against the PDMS sheet, closing channels directly above it, while retracted pins rested directly below channels. This computerized fluidic control is capable of rapid mixing between liquids and segmented plug-flow of immiscible fluids within the same channel architecture.

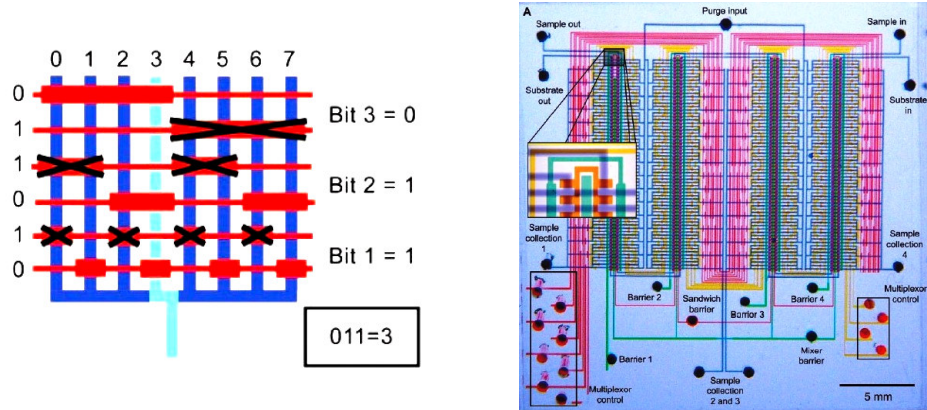


Figure 2.10: A pneumatic powered PDMS large-scale microfluidic integration (adapted from [10]). The fluidic network was integrated with a fluid multiplexor so that the number of required pneumatic control could be reduced.

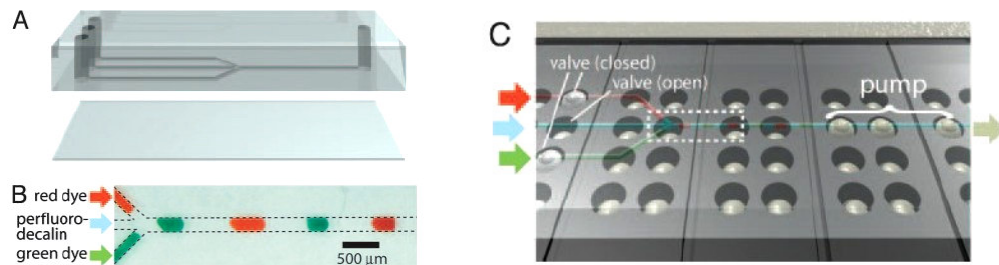


Figure 2.11: A computerized microfluidic pump and valve powered by Braille display (adapted from [36]). The fabricated PDMS channel was aligned with a refreshable Braille-display system underneath. As the Braille pin actuated, it pressed the above PDMS channel bottom to seal the valve.

Transport of liquid droplets by electrowetting has been a popular research topic recently. Generally speaking this is achieved by creating a pressure unbalance at a droplet interface, which is caused by a surface tension gradient. Surface tension changes when an external electric field is applied between the solid and the liquid, resulting in a redistribution of surface charge of solid surface and changes in wetting ability of the surface. This phenomenon is called electrowetting. Changes in surface tension also lead to changes in the contact angle between liquid and solid interface, and hence create a pressure difference. Based on electrowetting it is possible to actuate a discrete liquid droplet by locally changing the wetting ability of the surface. In an electrowetting device, the electrodes are insulated by a dielectric layer and a hydrophobic layer. It is necessary to maintain constant surface chemistry at hydrophobic surface for consistent electrowetting actuation.

A representative electrowetting device is presented in Figure 2.12 [34, 69]. It consists of a pair of electrodes on the top and bottom of the channel gap, both of which are insulated by dielectric and hydrophobic layers. The contact angle of the liquid and an unactuated solid surface is, because of the hydrophobic layer, larger than 90 degrees. This contact angle decreases as a potential difference is applied across the top and bottom electrodes. Pollack *et al* [34] reported electrowetting-based actuation of discrete droplets of aqueous electrolyte at voltages between 15–100 V. The average velocity of droplet transport exceeds 10 cm/s. Creation, mixing, and splitting of droplets was also reported using the same micro actuator structures. Meanwhile, Cho *et al* [35] has demonstrated an electrowetting on dielectric (EWOD) based device capable of creating, transporting, cutting, and merging liquid droplets in air environment at a 25 V DC applied voltage. All the fluidic movement is confined within the parallel-plate channel gap. Since the droplet

transport is dependent on the layout of the electrodes, it is possible to expand the electrode array for high-density microfluidic applications.

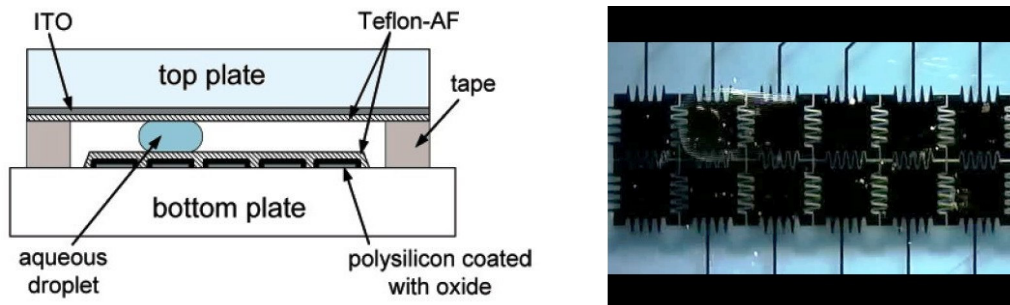


Figure 2.12: Electrowetting on dielectric: LEFT: adapted from [69]; RIGHT: adapted from [34]. This kind of device, for a single unit, consists of a pair of electrodes, both of which are insulated by dielectric and hydrophobic layers. Liquid droplets move as the local wetting condition changes. It is possible to build an array of control electrodes to use this device for large scale microfluidic integration.

Several derivative research areas in droplet transport by electrowetting have been investigated. Chiou *et al* reported 2-D droplet manipulation using light on optoelectrowetting devices (OEW) [84]. Optically controlled injection, transport, separation, and multiple droplet manipulation on a photosensitive surface were reported for nanoliter-size droplets, realized by sandwiching the droplets between two optoelectrowetting surfaces. A maximum transport speed of 78 mm/s for a 100-nL droplet was achieved by using a scanning laser beam. This optoelectrowetting mechanism has potential to be scaled up to process a large number of liquid droplets by projected optical images for high-density applications.

In addition to the family of electrowetting family, another way to transport a single liquid droplet is to employ active controls of thermal-induced gradients in surface tension, resulting in Marangoni flows that can be used to transport droplets without physical contact to the samples or the surrounding oil. Basu *et al* [37] have developed and tested a 128-pixel digital microfluidics system using Marangoni flows to manipulate and merge micro droplets with volumes less than 800nL at speeds up to 200 μ m/s. A schematic diagram of this device is shown in Figure 2.13. The developed system allowed for contact free manipulation of droplets, achieved by an array of heaters that locally changed the temperature and hence produced a local surface tension gradient. Flow velocities larger than 1 mm/s and with less than 5 degree change in surface temperature was reported.

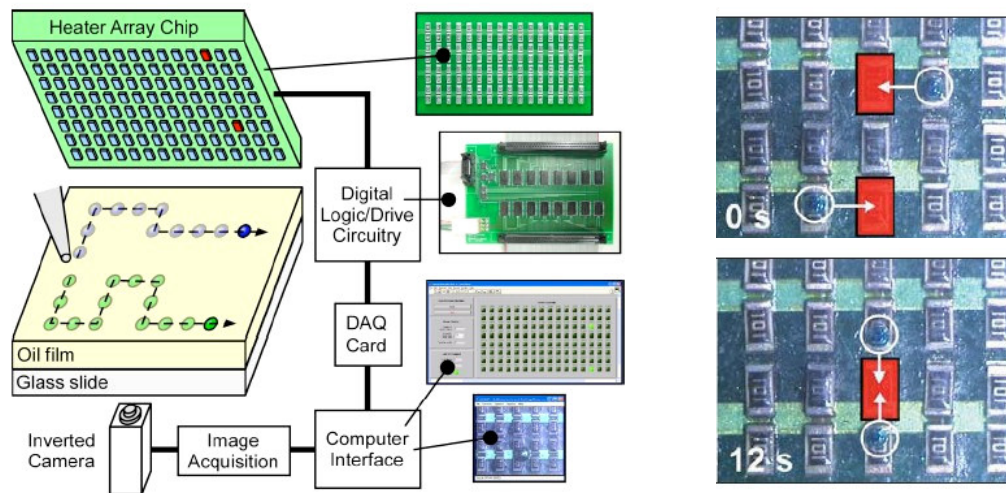


Figure 2.13: Droplet actuation using thermal-induced Marangoni flow (adapted from [37]). A programmable system for noncontact droplet actuation including a 128-pixel array of resistive heaters suspended above the oil layer.

2.4 Conclusion

This chapter reviewed polymer based micro valves and pumps, as well as several reconfigurable microfluidic systems for large-scale integration. Surprisingly, with one exception [30], electrostatic actuation is barely used in polymer microfluidic systems. This is because electrostatic actuation usually conflicts with water electrochemistry involved in the microfluidic system, generating gas bubbles by electrolysis and causing electrodes polarized. In addition, electrostatic forces are shielded by the water electrical double layers in a microfluidic channel, which prevents possible actuation of the devices. Integration of polymer material with electrostatics is another challenging problem. All these issues will be discussed in Chapter 3.

CHAPTER 3

RADIO-FREQUENCY ELECTROSTATIC “WET” MICRO ACTUATORS

This chapter presents a class of low voltage ‘wet’ MEMS elastomer-metal electrostatic micro actuators. Electrostatic actuation was historically limited to ‘dry’ MEMS applications because of (1) electrical double layer shielding of electrostatic force and (2) involved electrochemistry such as electrolysis and electrode polarization. The work presented in this chapter aims to correct these problems by employing low voltage radio-frequency electrostatics. The fabricated devices were able to actuate in water environments with no external fluidic connections and have actuation voltages as low as 15 – 20 V amplitude. This technology is compatible with conventional PDMS microfluidics, scalable down to nanofluidic regimes, and CMOS drive voltages. In addition to basic characterizations, two applications of the developed electrostatic actuator are also presented.

3.1 Introduction

Liquid manipulation plays an essential role in micro total analysis systems [19] (Chapter 1). A wide variety of valve and pump technologies have been developed for use in miniaturized systems for the life sciences [1, 3, 4] and analytical chemistry [2]. Among these, devices and systems made of elastomer, such as PDMS and parylene, have become

popular due to their simplicity of fabrication [5], low equipment costs and ready compatibility with existing lab equipment [5, 6, 7]. Some of these devices, however, depend on pneumatically-actuated pumps and valves which require multi-layer PDMS processes and many pressurized gas lines (40 – 100 kPa) to operate, even when employing a variety of clever multiplexing techniques [5, 8, 9]. The dependence on external pneumatic actuation is becoming increasingly problematic with the push towards integrated, high-density microfluidic systems which require thousands of independent valves [10]. Additionally, the lack of on-chip low power actuation schemes has prevented the adoption of these polymer devices for use in vivo [11].

This chapter presents design theory and characterization results of the electrostatically actuated elastomer-metal devices [17, 20]. The devices actuated using a 5 MHz, 15 – 20 V amplitude sinusoidal signal. This technology requires no external pneumatic connections for actuation. Individual devices can be readily integrated into discrete micro valves and peristaltic pumps (Chapter 3), and high-density microfluidic integration (Chapter 4). These devices are scalable into nanofluidic regimes and are compatible with CMOS processes.

3.2 Electrostatic Actuation in Water Dielectric

3.2.1 Pull-in Voltage with Water Dielectric

Electrostatic actuation is one of the most commonly used actuation mechanisms in MEMS technologies. Most electrostatic actuators consist of two oppositely charged par-

allel capacitor plates or beams separate by a dielectric gap. When a voltage bias is supplied across the capacitor, a parallel-plate field generates, and the plates and beams deform or move close accordingly by the attractive electrostatic force to close the gap [86]. Electrostatic actuators have a fast response time, generally on the order of ms, and the fabrication can be integrated with standard MEMS micromachining process [14].

However, electrostatic actuation has historically been limited to “dry” MEMS applications. Even though filling the space between the capacitor plates with water (relative permittivity $\epsilon_{rL} = 80$) would provide very low pull-in voltages, electrostatic operation in water was ignored due to the problems related with electrolysis [12], anodization [12] and electrode polarization [13]. Moreover, for an ionic solution, counter ions will be attracted to accumulate by the surface and forms an electrical double layer screening that diminishes the electrostatic forces [14, 21, 22]. Thanks to recent research progress, these problems can be solved by employing AC signals which has frequency high enough (MHz range) to prevent electrode polarization and electrical double layer screening, and low voltage to reduce electrochemistry [14, 15]. This makes electrostatic actuation underwater possible and generates a reliable actuation mechanism for “wet” MEMS and microfluidic applications.

Consider a plate-spring system shown in Figure 3.1. On applying a voltage between two parallel plates separated by a gap, g , electrostatic forces, counter balanced by the spring force, pull both plates together and decrease the gap. As the applied voltage increases the electrostatic force increases and at a critical point the spring force is no longer

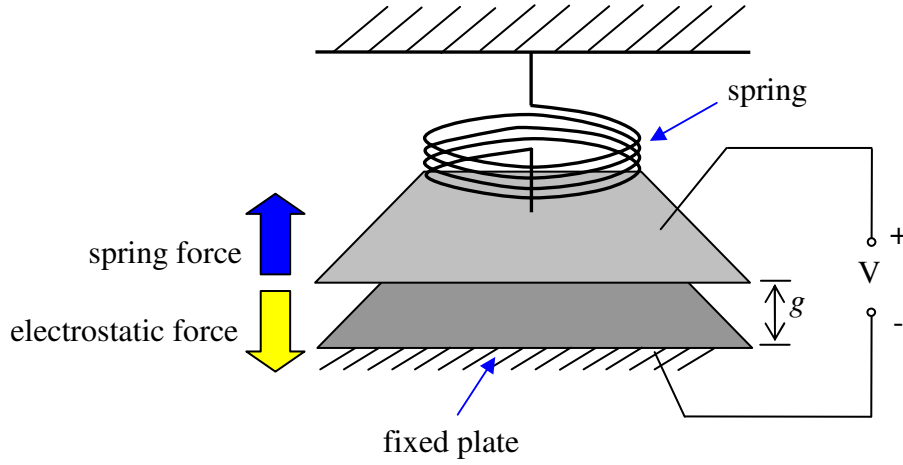


Figure 3.1: Perspective-view schematic of a plate-spring system for electrostatic pull-in. The top mobile plate is held by a spring while the bottom plate is fixed. The two plates are separated with a gap, g .

sufficient to counteract the electrostatic force, and the mobile plate collapses to the fixed plate. This effect is called *pull-in* and the applied voltage at this point is called *pull-in voltage*. The pull-in voltage is given as [22]

$$V_{PI} = \sqrt{\frac{8k(g + t_{ox}\epsilon_L/\epsilon_{ox})}{27\epsilon_0\epsilon_L A}} \quad (3.1)$$

where k is the mechanical spring constant of the spring holding the plates apart, g is the initial distance between the plates, t_{ox} is the thickness of any solid insulating layer covering the plates, ϵ_{ox} is the relative permittivity of the solid insulating layer, ϵ_L is the relative permittivity of the material between the plates, A is the area of overlap between the capacitive plates, and ϵ_0 is the absolute permittivity. The maximum range of travel of the mobile plate is limited to 1/3 of the original gap after which electrostatic force exceeds

the spring force. Note that as water has a relative higher dielectric constant, the thickness of any passivated dielectric cannot be ignored without comparing the original gap in the pull-in voltage calculations. It is also known that permittivity of water decreases nonlinearly with frequency [91] (Figure 3.2). A detailed derivation of pull-in voltage is in Appendix B.

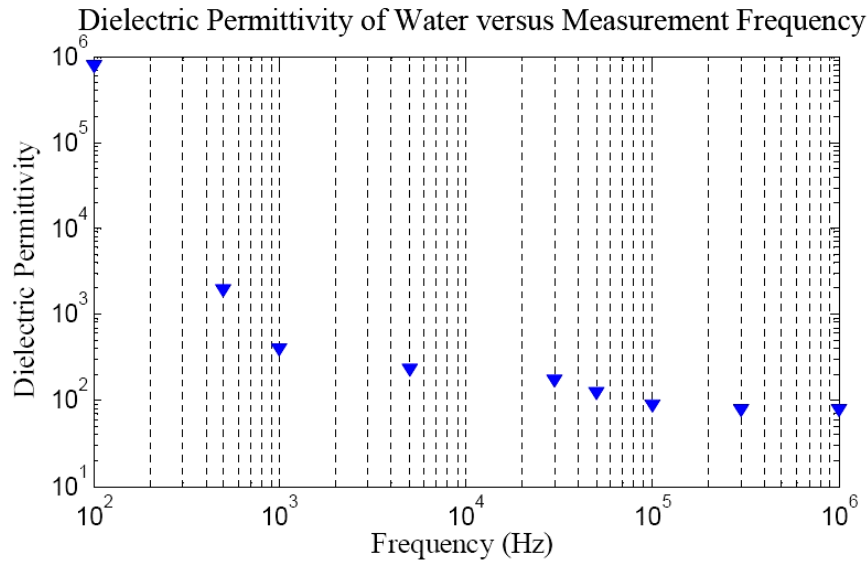


Figure 3.2: Relative Permittivity of water at different frequencies. Adapted from [91].

3.2.2 Spring Constant k of a Rectangular Plate

For a rectangular plate, the spring constant k in Equation (3.1) depends on several parameters: types of loading (point or distributed loading, in-plane or anti-plane, moment or torque), plate dimensions (lengths and thickness), material properties, and boundary conditions (fixed or simply supported). For a rectangular linear elastic plate with either

fixed or simply supported boundaries, the spring constant can be calculated using closed form equations. Consider a square plate under anti-plane distributed loading, the spring constant k is expressed as [16]

$$k = \frac{E \cdot t^3}{\alpha \cdot b^2} \quad (3.2)$$

where E is the Young's modulus of the plate, t is the plate thickness, b is the edge length, and α is a boundary condition coefficient. Boundary coefficients for different ratios of plate length and width are in [16]. For all simply supported edges, $\alpha = 0.444$; for all fixed edges, $\alpha = 0.0138$. Substitute Equation (3.2) into (3.1) yields

$$V_{PI} = \sqrt{\frac{8Et^3(g + t_{ox}\epsilon_L/\epsilon_{ox})}{27\alpha \cdot b^2 \epsilon_0 \epsilon_L A}} \quad (3.3)$$

3.2.3 Residual Stress of Capacitor Plates

Intrinsic stress is the stress of a thin film caused by the atomic structure mismatch between the film and substrate during deposition [23]. This stress is dependent on different matches of thin films and substrates and deposition conditions. For a free standing structure the tensile residual stress causes an increase in pull-in voltage that can be approximated as [24, 25]

$$V_{PI} = \sqrt{\frac{8Et^3(g + t_{ox}\epsilon_L/\epsilon_{ox})}{27\alpha \cdot b^2 \epsilon_0 \epsilon_L A} \cdot \left(1 + \frac{2(1-\nu^2)\sigma_R A}{9Et^2}\right)} \quad (3.4)$$

where σ_R is the residual tensile stress, ν is Poisson's ratio of the capacitor plate.

3.3 Device Concept and Design Strategy

Figure 3.3 shows the conceptual view of the basic device. The device structure was composed of glass substrate and metal-coated PDMS micro channels. In order to eliminate the rigidity contributed from the metal, the top metal electrode was patterned as spiral flexure to reduce its stiffness so that the whole channel structure was supported only by PDMS. The bottom electrode was formed by transparent ITO that allowed for microscopy from underneath. The metal-coated PDMS roof served as one capacitive plate and the ITO electrode formed the other. A layer of oxide was deposited on ITO for dielectric passivation. As a potential was biased between the top and bottom electrodes, the devices used electrostatic pull-in phenomenon to collapse the elastic channel roof onto the floor to close the channel gap. This collapse can be used as a valve in the same way that ‘Quake’ valves [5] use off-chip supplied pressure to collapse a PDMS membrane and seal a micro channel. Essentially by using electrostatic pull-in as the actuation mechanism the device is a self-actuating ‘Quake’ valve. This purely electrically-controlled approach also avoids external pneumatic connections.

In addition to PDMS based device, an all-metal micro channel design was also explored. The top metal electrode in this design was not patterned into spiral or meander spring to maintain a closed micro channel. However all-metal devices could plastically deform permanently and fail above the yield strength. It was thus important to ensure that the maximum stress generated during actuation did not exceed the yield strength (120 MPa) and deformed the devices permanently.

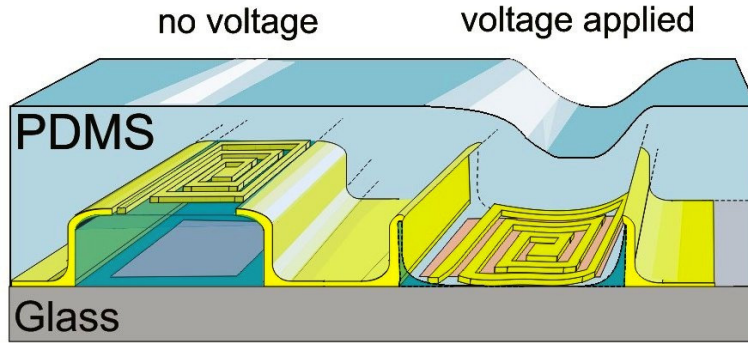


Figure 3.3: Conceptual view of a PDMS-based device. The bottom electrode is ITO which is insulated by a layer of oxide. The top electrode is made of chrome-gold, etched into spiral spring to reduce structure stiffness.

The most critical design parameter that needs to be optimized is the pull-in voltage. Ideally, the pull-in voltage of the device has to be low enough to be generated by on-chip electronics and not to induce electrochemistry. According to Equation (3.4), assuming no residual stress in the PDMS channel, this goal can be achieved by adjusting the dimensions of the capacitor area and each thin film. The PDMS material used in this work was Dow Corning® WL-5150, which we found had better adhesion to metal materials than normally used Dow Corning® Sylgard 184 silicone. It is worth noting that this silicone is also photo-patternable [87, 88]; basic material properties of WL-5150 is in Table 3.1. The final designed parameters and target pull-in voltage are listed in Table 3.2.

Based on parameter value in Table 3.2, the desired pull-in voltages were calculated as 13 V for PDMS membrane and 25 V for all-metal (gold) membrane. However, attempting to increase the area or decrease the thickness of the membrane to lower the pull-in voltage below 15 V resulted in devices that were so flimsy that Laplace-Young

pressure collapsed [28] the channel during conventional release. This issue was partially solved by using critical point drying (CPD) with optimized CO₂ purge time.

Table 3.1
Material Properties of Dow Corning® WL-5150 (Adapted from [26])

MATERIAL PROPERTY	VALUE
Nanoindentation modulus (MPa)	301
Nanoindentation hardness (MPa)	9.5
Film Residual Stress on Si Wafer (MPa)	2.6
Young's Modulus	160
Bulk Tensile Strength (MPa)	6.0
Bulk Elongation (%)	37.6
Dielectric Constant (1 MHz)	3.2
Dissipation Factor (1 MHz)	0.007
Leakage Current (A/cm ²)	1 × 10 ⁻¹¹
Breakdown Voltage (V/cm)	3.9 × 10 ⁵
Film Thickness (μm)	15-40

Table 3.2
Device Design Parameters

Device configuration	PDMS	All-metal (gold)
Membrane length	600 μm	600 μm
Membrane thickness	16 μm	2 μm
Channel height gap	8 μm	5 μm
Oxide permittivity	3.9	3.9
Oxide thickness	0.45 μm	0.45 μm
Liquid permittivity (water)	78	78
Membrane Young's modulus	160 MPa [26]	78 GPa
Membrane residual stress	2.6 MPa [26]	40.1 MPa [27]
Membrane Poisson's ratio	~ 0.5	0.42
Designed Spring Constant	6.76 N/m	26.36 N/m
Target Pull-in Voltage	6.29 V	9.79 V

3.4 Fabrication

Device fabrication followed standard MEMS micromachining process, as shown in Figure 3.4. Detailed process procedures are in Appendix C. 4-inch borosilicate glass substrates (Plan Optik) were piranha cleaned for 15 minutes. Indium tin oxide (ITO) electrodes were sputtered (1500 Å, Ener-Jet) on cleaned glass wafer and patterned through lift-off process in Shipley 1112A photoresist remover. The patterned ITO was then annealed at 750 °C in a rapid thermal anneal oven (Jet-first 150 RTP). The purpose of annealing ITO was to improve its conductivity and transparency. Afterward, a thin layer (4500 Å) of high-temperature (380 °C) oxide was deposited via PECVD (GSI) and annealed in the anneal oven at 700 °C. Contacts were timed etched through the oxide in 49% buffered hydrofluoric acid (BHF). The etch rate was about 0.1 μm/min. The wafer was then ready for patterning metal or metal-PDMS micro channels.

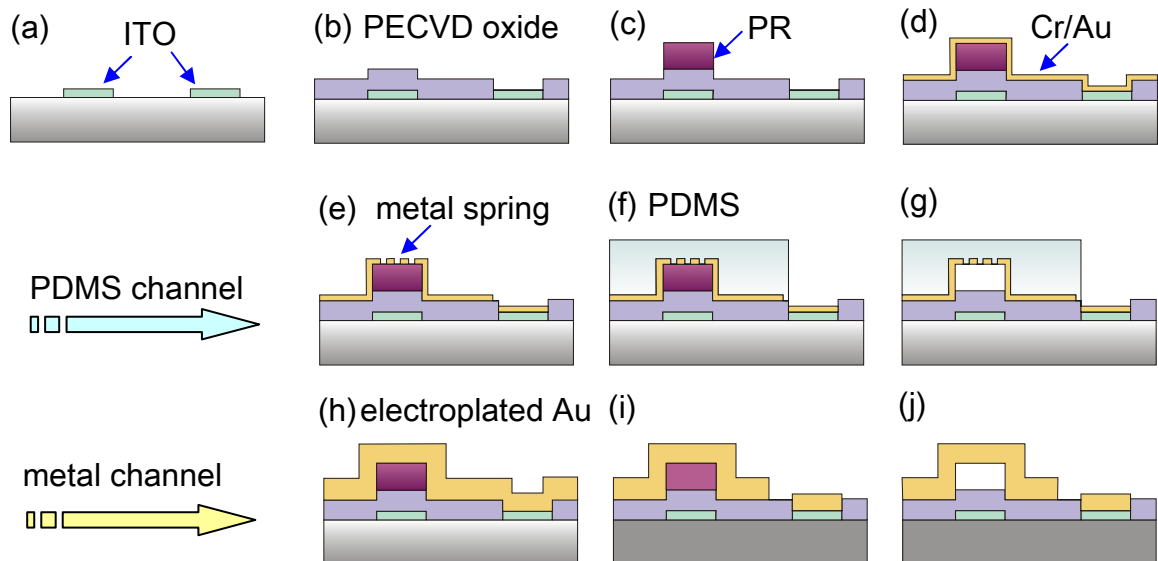


Figure 3.4: Fabrication process flow.

A 10 μm thick AZ® 9260 photoresist for metal-PDMS devices or a 5 μm Shipley 1827 for all metal-channel devices (Figure 3.3 h) was spun and patterned into desired micro channel geometries. Cr/Au (150 \AA /5000 \AA) was then evaporated (Ener-Jet) onto the substrate to form the top electrode. For metal-PDMS devices, the gold flexures were masked by patterned photoresist (Shipley 1813) and wet etched to form spiral springs. The patterned photoresist was flood exposed; developed and new resist was spun on the wafer. The wafer was then diced and the top photoresist was flood exposed and developed. Cr was removed from individual dies with standard Cr etchant. 16 μm of Dow-Corning® WL-5150 photopatternable PDMS was spun on each die, and then exposed and cured at 60 °C in an oven. Figure 3.5 is the WL-5150 thickness vs. spinning speed. Sacrificial channel photoresist (AZ-9260) was then removed by soaking the chip overnight in acetone and rinsed in methanol. Standard critical point drying (Tousimis Automegasamdri®-915B) was performed to release devices. The final thickness of WL-5150 was reduced to 12 μm because of compression by high pressure (1350 psi) during CPD process (Figure 3.6). Released chips were mounted onto a custom printed circuit board and wire bonded.

On the other hand, for all metal-channel devices, a 2 μm thick gold layer was electroplated and patterned to form desired micro channels. The sacrificial photoresist (Shipley 1827) was dissolved in acetone and rinsed in methanol. The chips were also dried by critical point drying.

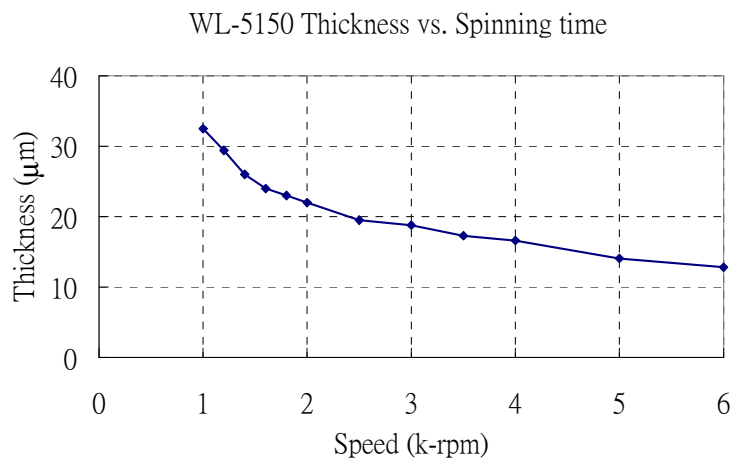


Figure 3.5: WL-5150 thickness vs. spinning speed (Solitec spinner).

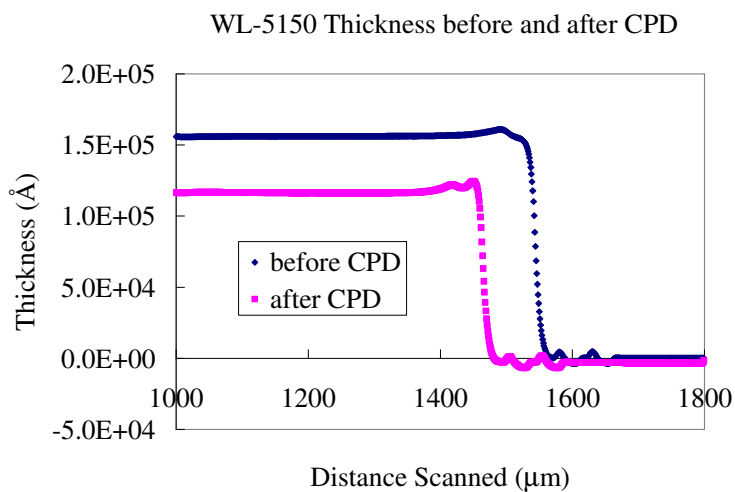


Figure 3.6: WL-5150 thickness before and after critical point drying. The PDMS thickness reduced 25 % (16 μm to 12 μm) after CPD.

3.5 Experiment Results

Inverted fluorescent microscopy was performed with a Nikon TE2000 for visual indication of device actuation. For fluorescent imaging and dosing, a mixture of de-ionized water and a Tris(2,2'-bipyridyl)dichlororuthenium(II) hexahydrate (Sigma) fluorophore was loaded in a reservoir and entered the micro channels through capillary action. Surface profilometry of a deflected membrane was carried out using a Zygo New View 5000. DC voltages were applied using a Keithley 2400 source meter. Radio-frequency voltages were applied with Agilent 33250A Function/Arbitrary Waveform Generator, 80 MHz.

3.5.1 Device Actuation and Surface Profilometry of Actuated Devices

Figure 3.7 is inverted white-light and fluorescent micrographs of un-actuated PDMS and all-metal devices, respectively. On applying a potential between the top gold electrode and bottom ITO electrodes, the deformable channel top collapsed and closed the gap. As the gap closed, the fluorescent solution was expelled out of the chamber so the closed region was dark in the fluorescent micrograph (c and f). Figure 3.7 c shows a PDMS device under actuation at 13 V, while image (f) shows device deflection with a supplied voltage at 18 V.

Figures 3.8 show the deflection profiles for both types of devices obtained in water with the Zygo non-contact profilometer, measured along the white dashed line in Figure 3.7. As can be seen, the device gap started to close when supplied with a voltage at the pull-in amplitude, and sealed better as the voltage increased. Comparing the two un-actuated surface profile, the PDMS device sagged about 2 μm . This is because the device was released in solvent that was absorbed by PDMS and resulted in volume dilation.

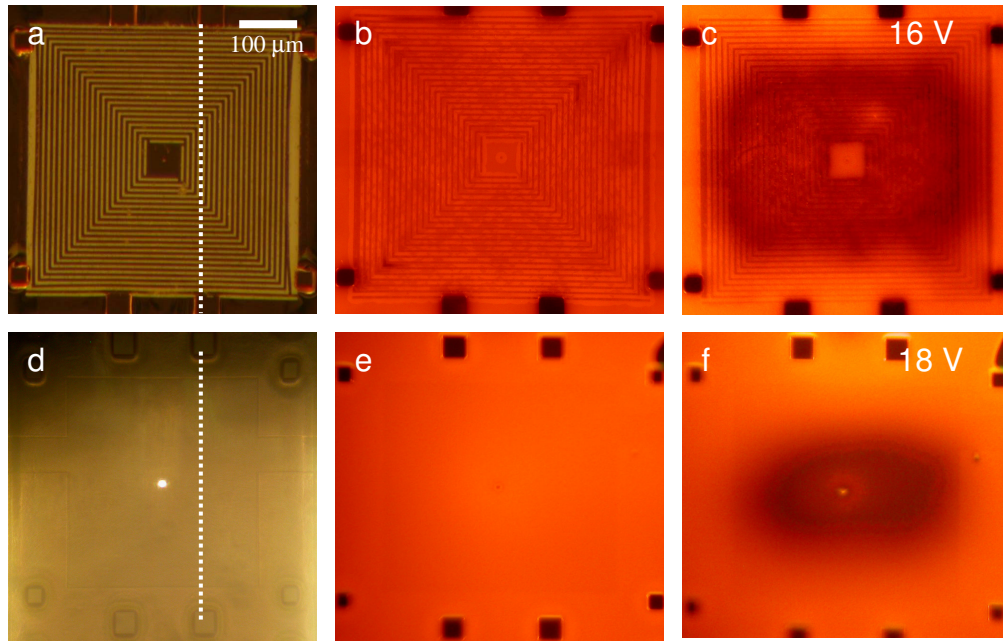


Figure 3.7: Device Actuation. (a) Unactuated PDMS device after sacrificial channel photoresist has been removed. (b) Unactuated PDMS device filled with DI water. Fluorescent ruthenium compound is added for visualization. (c) Actuated PDMS device. Deflection is clearly visible as the dark region. (d) All gold devices after release. (e) All gold devices with DI water and fluorescent compound. (f) An actuated all gold device.

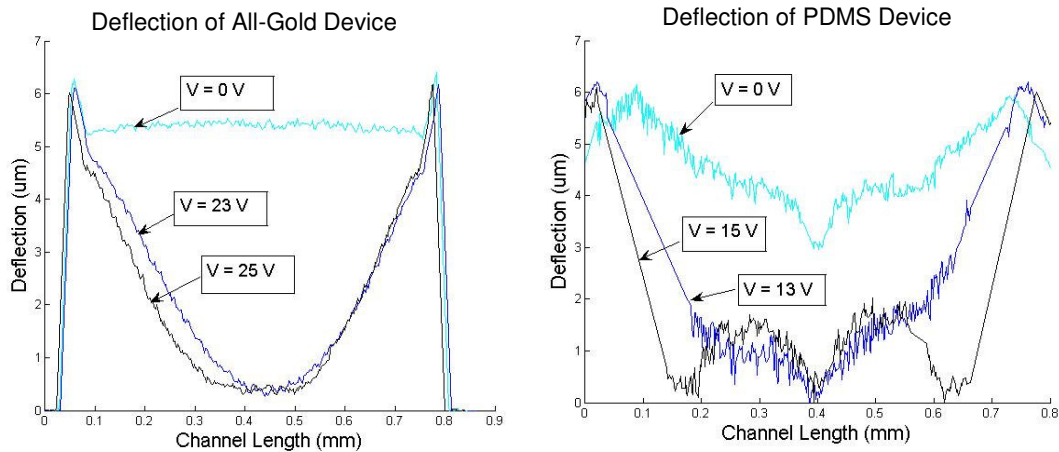


Figure 3.8: RIGHT: Profilometry cross-section along dashed line in Figure 3.7 (a). LEFT: Cross-section profilometry along dashed line in Figure 3.7 (d). Most PDMS channel experienced sagging ($\sim 2 \mu\text{m}$) after release.

Deflections of the PDMS and all-gold device, in both air and water dielectric, are presented in Figure 3.9. The pull-in voltages are marked by dashed lines. It was found that with a channel height (4-5 μm) and oxide thickness (0.4 μm), water dielectric allowed for a lower pull-in voltage. This also can be shown by examining Equation (3.1).

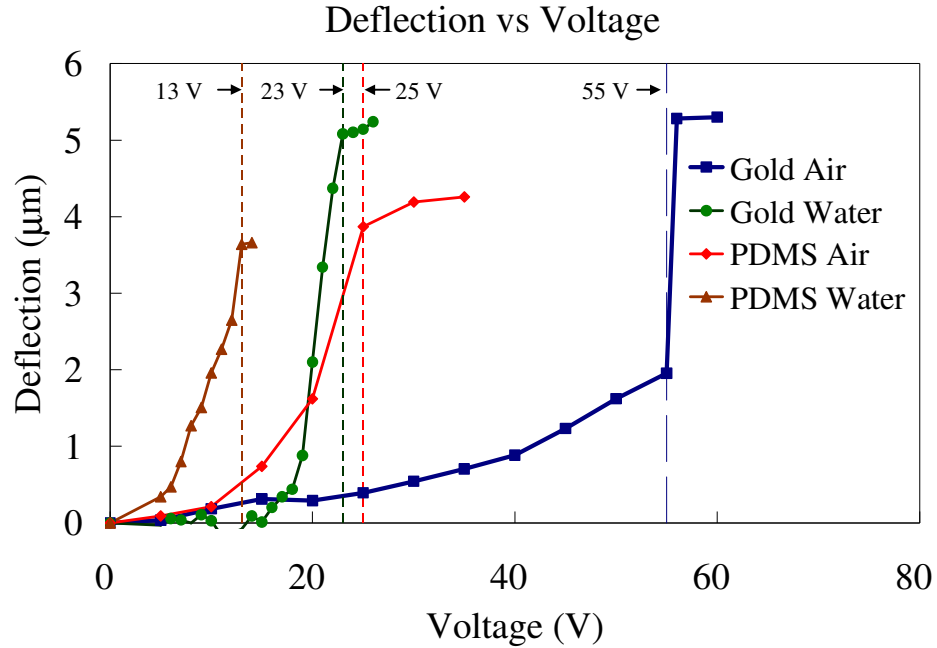


Figure 3.9: Deflection vs. voltage plot for all gold and PDMS devices. Pull-in is indicated on each plot with dashed lines.

3.5.2 Power Consumption and Current Draw

Given a spring constant k , an overall gap of g and a final remaining gap of thickness of the insulation layer after pull-in, the energy E expended to close an actuator is

$$E = \frac{1}{2}k(g - t_{ox})^2 \quad (3.5)$$

For the devices presented here, this corresponds to energies ranging from 0.55 nJ to 0.67 nJ for all-gold and PDMS-gold devices. All gold devices closed within 1 second (25 V); PDMS devices took about 5 seconds to close completely (13 V). Using (3.5) and the definition of average power ($P = E/t$), this corresponds to an average power consumption of 110 pW. The peak currents for all actuations were less than 1 μ A.

3.5.3 Applications as Micro Valve and Drug Doser

Figure 3.10 demonstrates the operation of the device as an effective valve. For visualization purposes, fluorescent water mixed with microspheres (0.5 μ m diameter, PolySciences) was used to fill a 6 mm long micro channel. The liquid flow was observed by detecting the movement of the microspheres. Fluid flow was induced by evaporative pumping across the micro channel. Upon valve actuation, the liquid movement stopped, the microspheres were expelled, and piled up against the boundary of the ITO electrode as pointed in Figure 3.10 (b). Once unactuated, the valve opened and the microspheres continued their flow. Valve and pump performance characterization with an improved design will be addressed in Chapter 4.

Figure 3.11 shows the device can also be used for programmed drug dosing. A single 10 μ m diameter pore was etched into the center of the micro channel roof. When the devices were unactuated, the contents of the micro channel could diffuse through the pore and into an aqueous medium above the channel. If actuated, the pore is sealed shut against the floor of the micro channel, preventing diffusion. These arrays are capable of

patterning the spatiotemporal dosing profile of aqueous molecules into cell or tissue culture [17, 18].

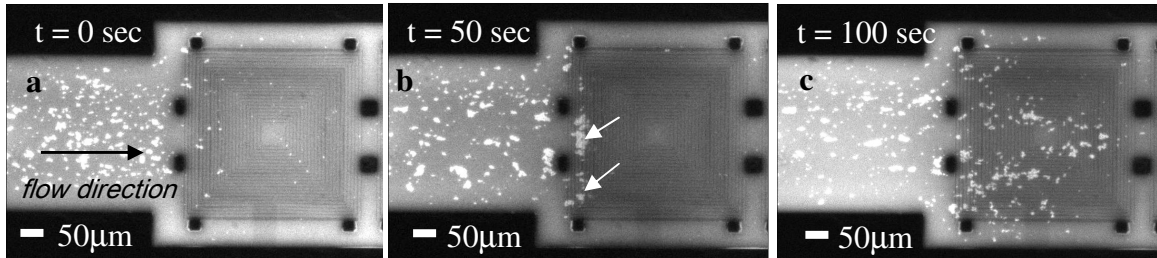


Figure 3.10: Fluorescent micrograph of devices operated as a micro valve. (a) Microspheres (0.5 μm diameter) mixed with fluorescent solution were loaded in to the micro channel. As the valve was open, the microspheres moved with liquid flow under an unactuated valve. (b) At $t = 50$ s the valve was closed, and the flow stopped. Microspheres were expelled by the valve and accumulated at the valve boundary, as pointed by the arrowhead. (c) As the valve was opened at $t = 100$ sec, the liquid flow resumed and the microspheres moved again.

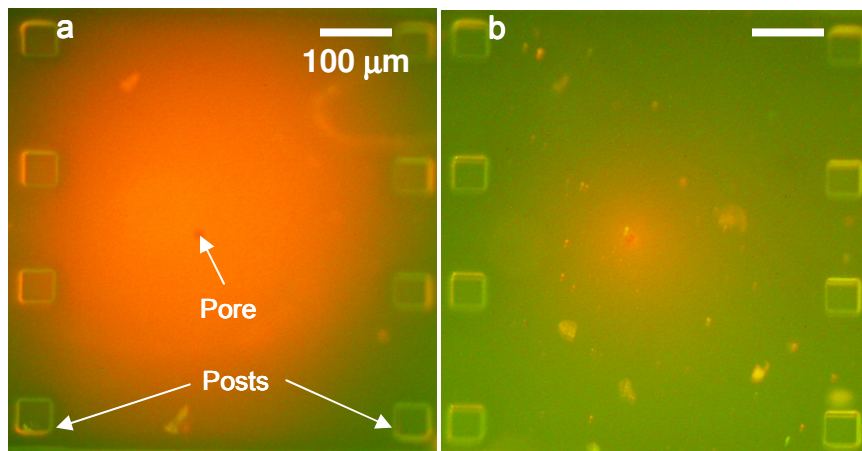


Figure 3.11: Drug Doser. The device can be used as effective drug dosers. (a) An unactuated device (open gap) with an etched hole at its center can behave as an open pore and diffuse chemicals into medium. (b) An actuated valve (closed gap) can close the pore and shut off the diffusion.

3.6 Conclusion

The work included in this chapter presented a class of 'wet' MEMS elastomer-metal electrostatic actuators. The electrostatic actuation underwater was studied and the pull-in voltage was successfully lowered (less than 20 V) by optimizing design of the device geometry. Two configurations, all-gold and metal-coated PDMS micro structures were explored. The devices were micro fabricated and tested using inverted fluorescent microscopy. These independent valves work at low pull-in voltages (15 V), are capable of integrating with PDMS microfluidic devices and can be assembled into pumps and valves. Applications of the developed device in micro valve and drug dosing were demonstrated. The developed device is ready to be integrated into discrete micro valves and peristaltic pumps, which will be discussed in the next chapter.

CHAPTER 4

PDMS MICRO VALVE AND PERISTALTIC PUMP

This chapter presents a PDMS micro valve-pump technology based on the electrostatic micro actuator developed in Chapter 3. The devices operate by electrostatic gap-closing of a thin-film metal embedded PDMS micro channel. The presented pump and valve technology requires no external pneumatic connections for operation and is compatible with conventional PDMS microfluidics. The devices have actuation voltages low enough to be driven by a pre-programmed USB-interface microcontroller and IC amplifier, which makes possible the design of VLSI microfluidics and portable μ TAS.

4.1 Introduction

Micro pumps and valves are essential elements for liquid transport in micro total analysis systems. Among various micro pumps, polymer-based pumps are the most popular found in microfluidic systems [5, 29, and 30] due to widespread usage of elastomer as microfluidic channel structure. However, these elastomer pumps usually use off-board pressure/vacuum pneumatic control and lack scalability and portability. Based on the technology developed in Chapter 3, this chapter presents an electrostatic PDMS micro pumps and valves, as shown in Figure 4.1, that can actuate water, oil, and air at low actuation voltage. Self-actuation ability of each individual valve makes possible the design of fluidic systems with thousands of actuated components each driven by digitally syn-

thesized control signals. Moreover, since the actuation is based on MHz frequency electrostatics, the electrical double layer (EDL) shielding of electrostatic force and electrode polarization are avoided. Further, the devices: a) are scalable into the nanofluidic regime, and b) can be driven by conventional CMOS on-chip electronics.

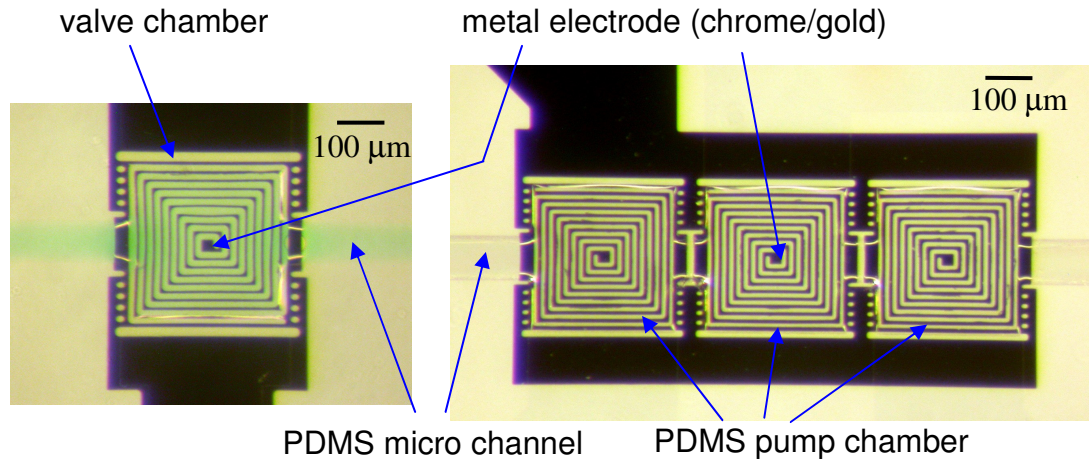


Figure 4.1: Top view of fabricated valve and pump devices. LEFT: a micro valve filled with green water (food color). RIGHT: a three-valve peristaltic pump.

4.2 Device Operation and Design

Peristaltic pumping, using sequential compression on a continuous fluid channel or successive valve chambers, is a widely used technology to pump various fluids. The chamber (channel) of a peristaltic pump is generally flexible so that it can deform to close the gap with external driving force. Peristaltic pumps are especially suitable to pump chemical-sensitive and sterile liquid because this pumping mechanism is purely mechanical with no electrochemical reaction involved, so no contamination will be generated dur-

ing liquid transport. For micro scale peristaltic pumps, they are usually composed of discrete actuatable micro chambers instead of using a continuous deformable chamber or channel. Typical actuation mechanisms of micro peristaltic pumps include electrostatic, piezoelectric, pneumatic, thermopneumatic, electromagnetic actuations.

The peristaltic pump developed in this work consists of three identical valve chambers each of which can be actuated independently by electrostatic actuation. Figure 4.2 shows the concept view of design of this peristaltic pump. As described in Chapter 3, the oxide-insulated ITO forms the bottom capacitor plate and the metal spiral (Cr/Au) form the other. Since the metal is patterned as spiral spring, the stiffness contributed by the metal layer can be neglected and the structure rigidity is mainly supported by the PDMS channel. As a biased potential larger than the pull-in voltage is applied, the flexible channel top collapses and then seal the gap, and thus peristaltic pumping can be achieved by sequentially actuating the three chambers.

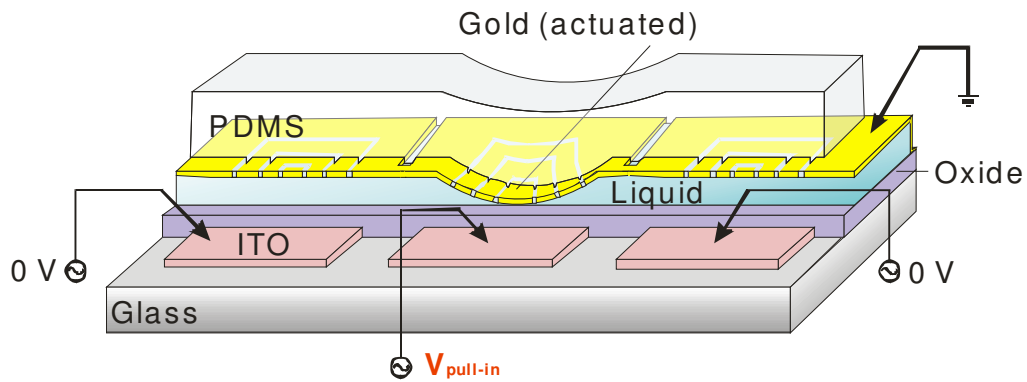


Figure 4.2: Conceptual view of an electrostatically-actuated PDMS micro pump. The middle micro valve is actuated and this is a 010 actuation step (0: unactuated; 1: actuated).

The peristaltic actuation signal is a series of synthesized digital signals, as shown in Figure 4.3. For a three-chamber peristaltic pump, a complete pumping cycle has three phases with six individual equally-timed steps: $011 \rightarrow 001 \rightarrow 101 \rightarrow 100 \rightarrow 110 \rightarrow 010$. This scheme is also known as 120 degree pattern [5]. In each of the actuation step, 0 stands for an open, unactuated valve with liquid inside; 1 stands for a closed, actuated valve that has no liquid. Generally speaking, the flow rate of peristaltic pumping is dependent on the period of one complete pumping cycle.

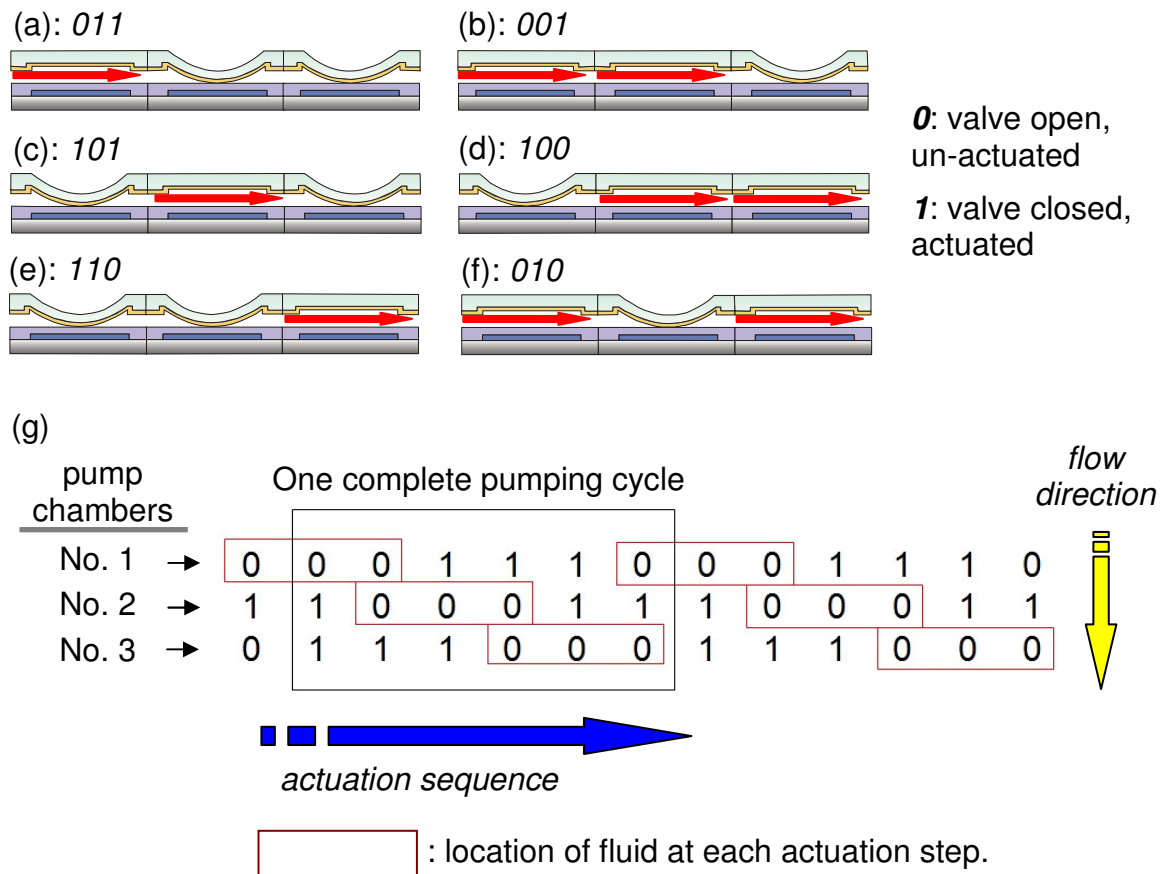


Figure 4.3: Actuation sequence cycle of a peristaltic pump. Images (a)-(f) show the liquid movement in a complete actuation scheme. Red arrows in (a)-(f) indicate liquid in an un-actuated valve. Detailed actuation process of each valve is in figure (g).

Similar to the electrostatic micro PDMS-metal actuator presented in Chapter 3, the design of these micro peristaltic pump and valve was aimed at a 15 V pull-in voltage. In the new design, the area of the deformable PDMS membrane was decreased to 300 μm by 300 μm (originally 600 μm by 600 μm). According to Equation (3.4), decrease in the area of the capacitor plates will lead to an increase in the pull-in voltage. In order to maintain a low pulling voltage, the thickness of the 300 μm by 300 μm PDMS membrane had to be reduced. Dow Corning® WL-5351, a less viscous spin-on silicone that allows for making a 6 to 18 μm film, was thus used to make a thinner capacitor membrane (6 μm compared to 16 μm of WL-5150 in Chapter 3). The basic material properties of WL-5351 [26] are listed in Table 4.1. Based on the material property of WL-5351, with a target of pull-in voltage lower than 15 V, the designed device dimensions are tabulated in Table 4.2.

Table 4.1
Material Properties of Dow Corning® WL-5351 (adapted from [26])

MATERIAL PROPERTY	VALUE
Nanoindentation modulus (MPa)	538
Nanoindentation hardness (MPa)	29
Film Residual Stress on Si Wafer (MPa)	6.4
Young's Modulus	371
Bulk Tensile Strength (MPa)	10.3
Bulk Elongation (%)	7.4
Dielectric Constant (1 MHz)	3.3
Dissipation Factor (1 MHz)	0.014
Leakage Current (A/cm^2)	7.9×10^{-11}
Breakdown Voltage (V/cm)	8.3×10^5
PCT Moisture Absorption (%)	<0.2
Film Thickness (μm)	6-18

Table 4.2
Device Design and Dimensions

Membrane length	300 μm
Membrane thickness	6.7 μm
Channel height gap	4 - 8 μm
Oxide thickness	0.4 μm
Designed spring Constant	27.10 N/m
Target Pull-in Voltage	16.85 V

4.3 Device Fabrication

Figure 4.4 shows the fabrication flow of a basic valve device. Indium tin oxide (ITO) electrodes (1500 Å) were patterned and insulated by 4000Å PECVD oxide. Oxide was etched to expose the contact pads. Photoresist (AZ-9260, 10 μm) was used as micro channel mold for subsequent metal and PDMS deposition. The metal layer was composed of Cr/Au (150/5000 Å) and etched into spiral flexure. A thinner PDMS precursor, DOW CORNING® WL-5351, was spun coated and UV exposed (i-line radiation, $\lambda = 365 \text{ nm}$, 1000 mJ/cm^2) to form the micro channel structure. The hardbake condition of WL-5351 silicone was optimized to 30 minutes in a 110 °C oven. Compared with WL-5150 used in the work of Chapter 3, we found out the process condition (UV wavelength, exposure time and energy, baking time and temperature) of WL-5351 was more critical because this thin silicone tended to be attacked during acetone and methanol soaking. Figure 4.5 shows properly and insufficiently cured WL-5150 membrane respectively. The final thickness of the PDMS membrane was 6.7 μm .

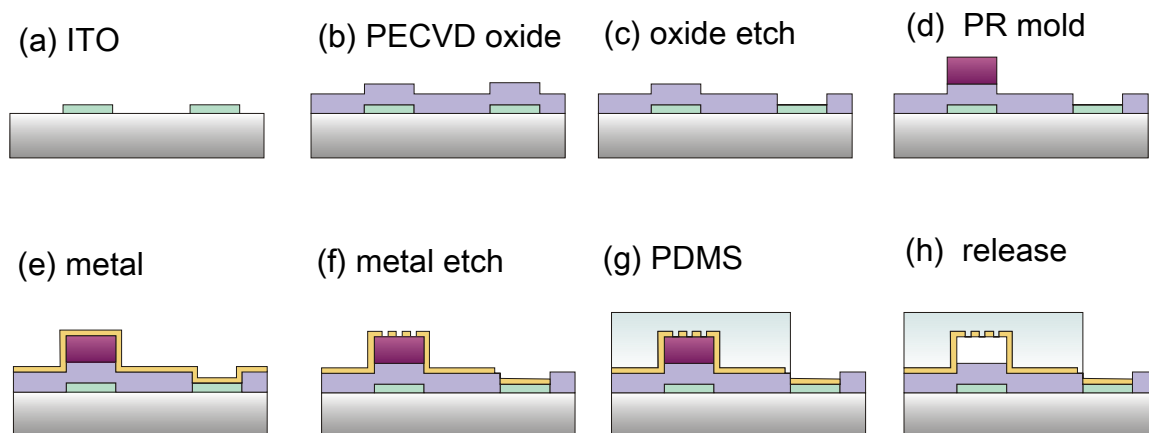


Figure 4.4: Fabrication process flow. Dow Corning® WL-5351 spin-on PDMS (6.7 μm) was used to make micro channel structures.

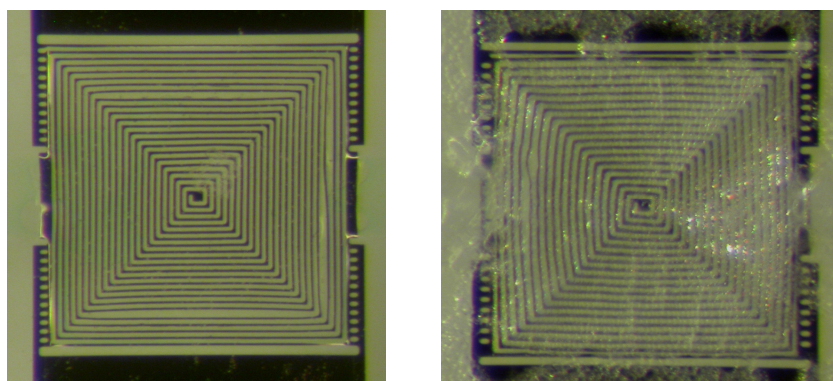


Figure 4.5: Properly (left) and insufficiently (right) cured WL-5351 membrane after solvent soaking. Insufficient UV photo-activation, baking time and temperature resulted in poor cross-linking or reduced film retention.

4.4 Experiment Setup

4.4.1 *Fluorescent Microscopy and Fluidic Characterization*

All fluidic measurement was made with fluorescent microscopy. Figure 4.6 (a) shows the schematic of experiment setup and the photographs of the apparatus are shown in Figure 4.6 (b) and (c). Flow rate was acquired by measuring the average velocity of 0.5 μm diameter microspheres (PolySciences) in the solution on an inverted fluorescent microscope (Nikon TE2000-U). Two pressure transducers (40PC150, Honeywell) were installed both upstream and downstream of the fabricated device to measure pressure difference across. Fluidic connectors (TEE and CROSS), shut-off valves, tubing (Upchurch Scientific) are used to construct the fluidic network. A syringe pump (KD Scientific) was used to flush and fill the whole system. The pressure source is generated by a compressed gas bottle that connected to a sealed bottle with half-filled liquid. Fluorescein sodium and Tris(2,2'-bipyridyl)dichlororuthenium(II) hexahydrate (Sigma) were used for visual indication of fluid flow.

4.4.2 *Control Circuitry*

The peristaltic pump was driven by digitally synthesized signals. The original signal was a sinusoidal wave generated by a function generator (Agilent 33220) and then amplified by an RF amplifier (Amplifier Research) with a fixed gain 20. This amplified sine wave was then send to a three parallel optical relay (PVA 1352N, International Rectifier) switch circuitry, as shown in Figure 4.7. Each switch circuitry used two relay IC's individually controlled by a pair of out-of-phase digital signals generated from the programmable USB interfaced micro controller (BS1 USB, Parallax), to ensure the output signal

is either high (15 V peak-to-peak) or ground. Since the actuation voltage is low enough to be generated by an IC amplifier, the actuation signal can also be amplified by a two-stage differentially amplifier built around AD-815 (Analog Devices).

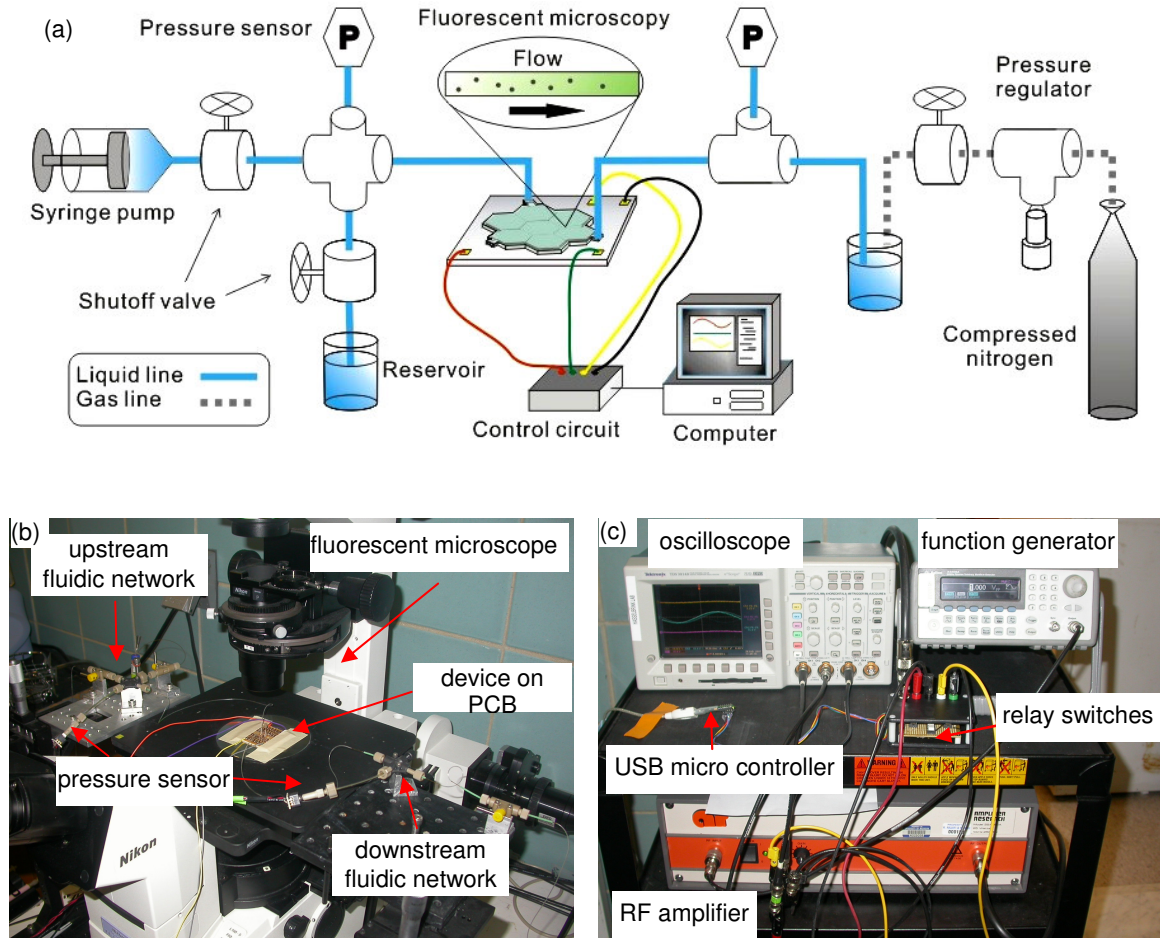


Figure 4.6: (a) Schematic of experiment setup for liquid flow characterization. The actuation signal is synthesized and switched by pre-programmed USB-interfaced micro controller and optical relay switch. (b) and (c) Photograph of experiment apparatus. The upstream and downstream fluidic networks were built on height-adjustable stages to balance hydrostatic pressure.

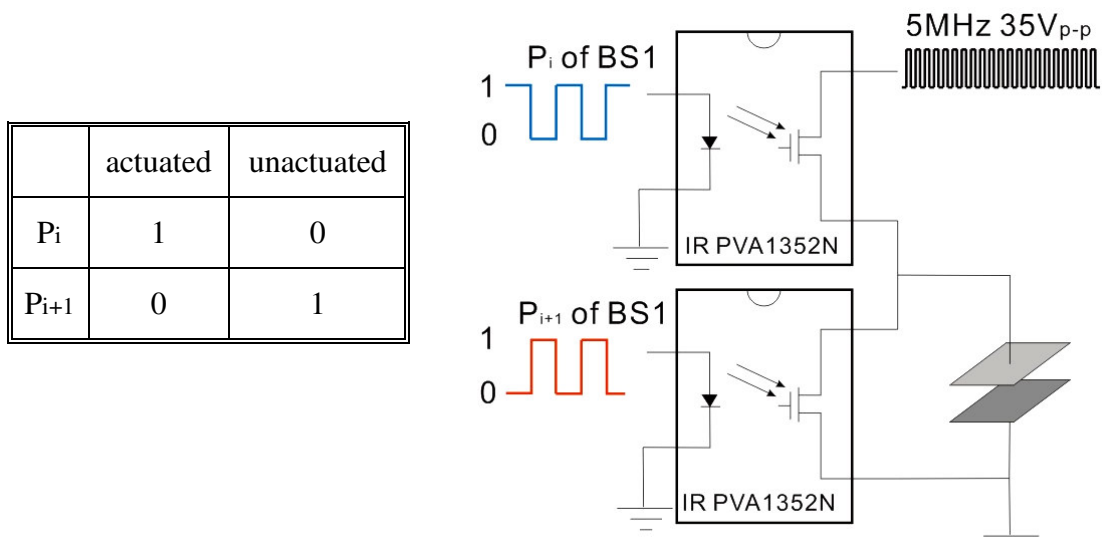


Figure 4.7: Circuit diagram for generating the actuation signal for peristaltic pump. For a single switch circuitry, signals of Ports P_i and P_{i+1} from BS1 micro controller were always out of phase to ensure the top capacitor plate was either grounded or actuated.

4.5 Results and Discussion

4.5.1 Valve Performance

Figure 4.8 shows the basic valve operation. $0.5\ \mu\text{m}$ microspheres were used for indication of liquid flow (green arrowhead). As the valve closed, the PDMS-metal membrane collapsed to seal the channel gap and the microspheres were either expelled or trapped inside the valve (yellow arrowhead). Expelled microspheres accumulated at the upstream valve boundary, as pointed out by the red arrowhead. In order to measure the initial open pressure of the valve, a compressed nitrogen source was connected to a half-filled sealed liquid bottle to provide constant pressure (gas line of Figure 4.6 (a)). The hydraulic resistance of the external fluidic network and the valve chip had at least 3 order of magnitude

differences so the pressure drop in the fluidic loop can be neglected. The initial open pressure of an actuated valve was measured to be about 5.7 psi (39.3 KPa).

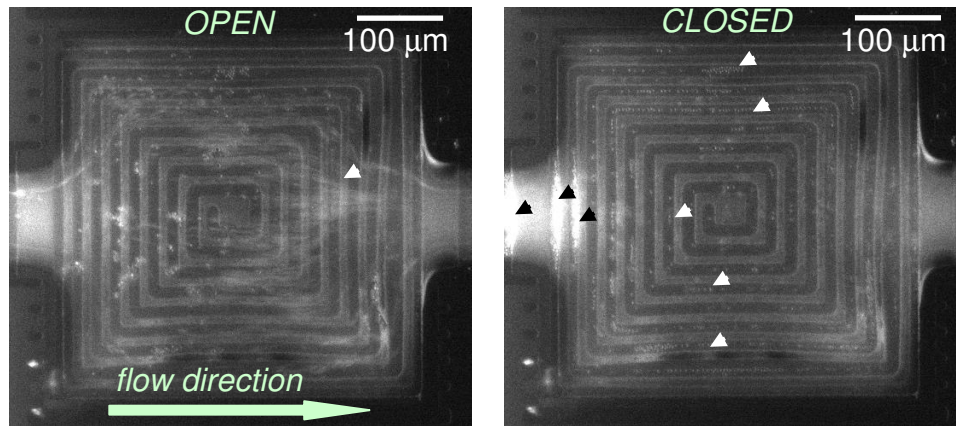


Figure 4.8: LEFT: open valve (un-actuated). White arrowhead indicates the fluid flow in an open valve. RIGHT: closed valve (actuated). White arrowheads are the microspheres trapped in a closed valve, and black arrowheads are the expelled microspheres piled-up against the valve boundary.

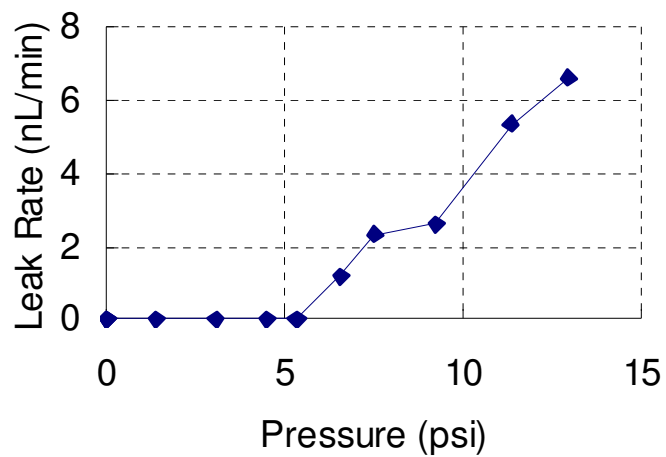


Figure 4.9: Pressure vs. valve leak rate. An actuated valve was able to hold pressure up to ~ 6 psi (39.3 KPa).

4.5.2 Pumping

Figure 4.10 shows the operation of a three-valve peristaltic pump (LEFT) and the flow rate at different actuation frequencies (RIGHT). Microspheres (diameter = $0.5\ \mu\text{m}$) were used for flow indication and flow rate measurement. Before turning on the pump the hydrostatic pressure was carefully balanced by tuning the height of upstream and downstream fluidic network stages. The pump was activated (pump frequency = 1.6Hz) at $t = 1\text{ s}$ and at $t = 10\text{ s}$ it can be clearly seen that the microspheres moved toward down stream. When $t = 100\text{ s}$ most microspheres had been pumped out. The flow rate was dependent on actuation frequency and the maximum flow rate is 4.44 valve-volumes per minute (about 1 nL/min) at 1.6 Hz actuation frequency. After this critical frequency the flow rate decreases as pumping frequency increases.

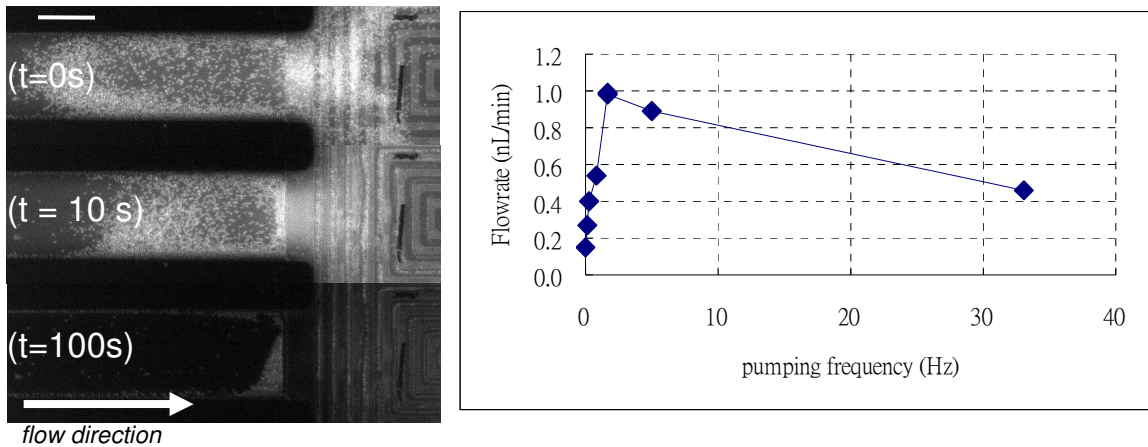


Figure 4.10: Pump performance. LEFT: pumping indication by the movement of microspheres. The scale bar is $100\ \mu\text{m}$. RIGHT: flow rate vs. actuation frequencies. The maximum flow rate was 1 nL/min at 1.6 Hz pumping frequency.

4.5.3 Discussions of System Applicability

There are several ways to lower the pull-in voltage by (1) reducing the channel gap (2) increasing the area of the capacitor plates and (3) reducing the stiffness of the channel structure. However adjustment in these parameters has some limitations. While reducing the channel gap is the most effective way to reduce the pull-in voltage, it also reduces the volume and displacement of each stroke resulting in a decrease in volume flow rate and may cause difficulties in releasing the device such as membrane stiction. Increase in component area prevents large scale integration of the μ TAS system, and also have potential stiction problems. Lowering the stiffness of membrane material of the may lower the reliability and robustness of the device structure and reduce the lifetime of the device. The lifetime of current device is more than 25,000 cycles (about 7 hours of continuous operation at 1.1 Hz).

Table 4.3 compares the PDMS system with parylene system by Tai *et al* [30]. In addition to difference in membrane materials, the parylene system is a multilayer structure and the capacitor plates are separated with air as dielectric so that working liquid of this system is isolated from the electric field. This design and high Young's modulus of parylene (3.2 GPa) lead to a higher pull-in voltage (80 - 130 V) for actuation. The PDMS system developed here has only one layer of micro channel, directly uses working liquid as dielectric. The Young's modulus is also smaller than that of parylene by two to three orders of magnitude (0.75 – 160 MPa vs. 3.2 GPa). Therefore the pull-in voltage of the PDMS system is much lower (15 - 20 V) than that of the parylene system. Our PDMS system also benefits from a more common usage of PDMS in most microfluidic applications.

Table 4.3
Comparison with Parylene Systems in [30]

	PDMS System	Parylene System [30]
Chamber volume	0.225 nL	0.094 nL
Pull-in Voltage	15 – 20 V	110 V
Actuation Frequency	1.6 Hz	20 Hz
Max. Flow rate	1nL/min	1.7 nL/min

4.6 Summary and Conclusion

This chapter presented electrostatically-actuated PDMS micro valves and peristaltic pumps. The devices operated only low pull-in voltages that can be provided by on-chip electronics and requires no external pneumatic connections for operation. The driving circuit was composed of optical relay switches controlled by a user-programmable USB-interfaced micro controller for different actuation frequencies. Pump and valve performance compares well with previous polymer electrostatic micro pumps [30]. The next chapter will present a reconfigurable microfluidic system for high density integration based on these self-actuatable electrostatic liquid valves and pumps.

CHAPTER 5

RECONFIGURABLE ELASTOMER MICROFLUIDICS

This chapter presents the design, fabrication, and characterization of an electrostatically actuated user-reconfigurable PDMS elastomer microfluidic system. By adding metal flexures into the PDMS polymer, individual channels could be made to self-close without the use of pneumatics via the application of 10 – 20 V, 5 MHz signals synthesized digitally by a microcontroller and a radio-frequency op amp. These valves were arranged into hexagonal or quadricular arrays with 75% fill factor. During use, valves were selected to be permanently closed, permanently open or addressable; this allows for the on-the-fly determination of channels, valves and pumps. We present characterization of flow and pressure data for valves, pumps and demonstrate various multi-component configurations of the system. The presented technology is compatible with standard PDMS microfluidics, has actuation voltage low enough to be driven by commercial CMOS IC's and can be used to displace aqueous, gaseous and lipid phases. The primary contribution of this technology is to provide a scalable platform for the very large scale integration of micro total analysis systems.

5.1 Introduction

This chapter presents a technology that can be easily integrated into conventional

PDMS microfluidics and uses no exotic materials or processes. The technology presented is a completely reconfigurable distributed elastomer microfluidic network system that requires only low voltage on-chip control. This integrated technology, based on the electrostatic wet actuators developed in Chapters 3 and 4, was achieved by grouping identical micro valve components for large-scale integration as shown in Figure 5.1. The device used radio-frequency electrostatics for actuation. With the aid of the control circuitry built around a user-programmable micro controller, this reconfigurable microfluidic system is capable of doing various user-defined patterns of liquid manipulations and controls.

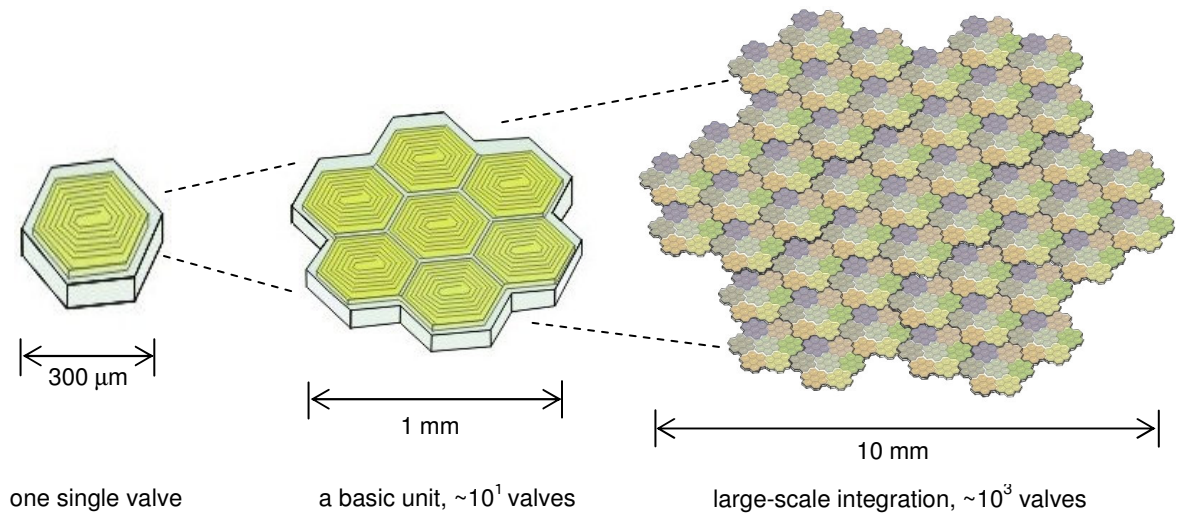


Figure 5.1: A conceptual view of microfluidic large-scale integration. Each single valve developed previously had a $300\ \mu\text{m}$ by $300\ \mu\text{m}$ area so it is possible to fabricate a chip with more than 10^3 discrete $1\ \text{cm}$ by $1\ \text{cm}$ valve components.

5.2 Device Concept and Design

Compared with devices designed in Chapters 3 and 4, here we have made an improvement in device configuration by using hexagons. Hexagonal chambers were found preferable to squares because (1) flexible hexagons chamber top has a more uniform deflection for better valve seal (2) hexagons has more connections to adjacent valve chambers that shortens liquid transport path, and (3) hexagons is a very compact footprint that can be expanded indefinitely. Figure 5.2 shows the conceptual view of a basic unit. The device consists of 7 hexagon micro chambers which can be actuated independently by electrostatic pull-in of a PDMS-metal membrane [20]. The reconfigurable distributed microfluidics was achieved with many actuated components each driven by digitally synthesized signals. The embedded metal flexure forms the top capacitor plate and the ITO electrode forms the bottom plate. When a voltage above the pull-in voltage is applied, the PDMS-metal “roof” collapses onto the “floor” and liquid within this actuated chamber is expelled into adjacent open micro chambers. This applied signal had a 5 MHz frequency to prevent electrical double layer screening of the electrostatic forces [15]. The patterned spiral metal lines (5-8 μm wide, 5000 Å thick) were only for electric conduction of the PDMS, and its stiffness could be neglected when compared to that of PDMS membrane.

The spring constant of hexagon membrane was calculated by finite element method (FEM) via commercial FEM software COMSOL® Multiphysics because it could not be directly obtained from a closed-form equation. The spring constant of a PDMS hexagon membrane with a 200 μm edge length and a 7.2 μm thickness was calculated to be 20 - 30 N/m and the corresponding pulling voltage with a 2.5 - 5 μm thick water dielectric

was found to be about 15 - 20 V. The inlets connecting to each micro chamber were 50 μm in width and 5 mm in length.

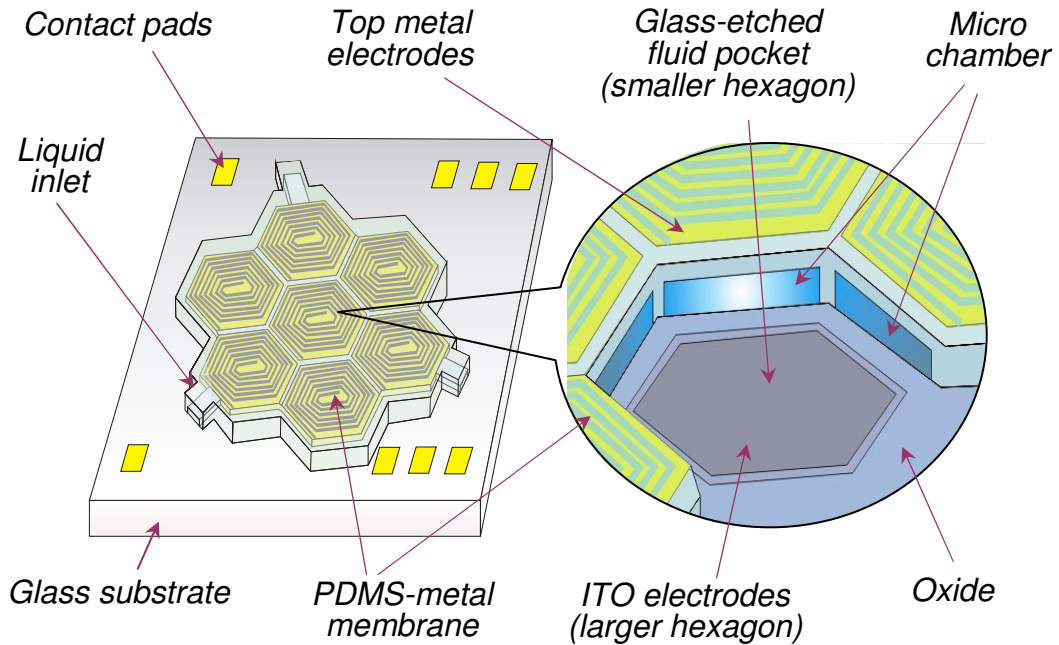


Figure 5.2: Conceptual view of a reconfigurable microfluidic device built on a glass substrate. The top PDMS-metal membrane with metal flexure and the bottom ITO form the capacitor plate pairs. Each valve component is connected to six other adjacent component and can be electrostatically actuated independently. A valve seat is made by glass wet etching. An insulating oxide layer is deposited on the ITO electrode.

5.3 Fabrication

The fabrication process of this reconfigurable microfluidic system started with making a valve pocket. A piranha-cleaned glass substrate was first patterned with photoresist mask (Shipley 1827, 3 μm) and wet etched in diluted HF (HF : DI = 1 : 10) to form a 1 μm recess. Indium tin oxide (ITO, 1000 \AA thickness) was deposited via sputtering, pat-

terned by lift-off, annealed at 700 ° C in RTA, and covered with a layer of 4000 Å plasma-enhanced chemical vapor deposition (PECVD) oxide. This oxide layer was annealed at 550 ° C in a RTA to reduce pinholes, increase breakdown voltage and increase the effective dielectric constant. Photoresist (AZ-9260, ~10 μm) was then spun, baked and patterned into a micro channel mold. The thickness of this photoresist mold was reduced to 8 μm after hardbake. A thin film of Cr/Au (150/5000 Å) was then sputtered and patterned using wet-etching to form the top capacitor plate. A stiff PDMS (Dow Corning® WL-5351, E = 370 MPa) was then spun and cured to form the micro chambers and channels. After releasing in acetone and methanol, the chip was released on a hot plate at 80 ° C for 2 min. The final channel height and the thickness of PDMS-metal membrane were 2.5 - 5 μm and 7.2 μm, respectively. The device was mount and wire bonded onto a custom printed circuit board. The fabrication process is shown as Figure 5.3.

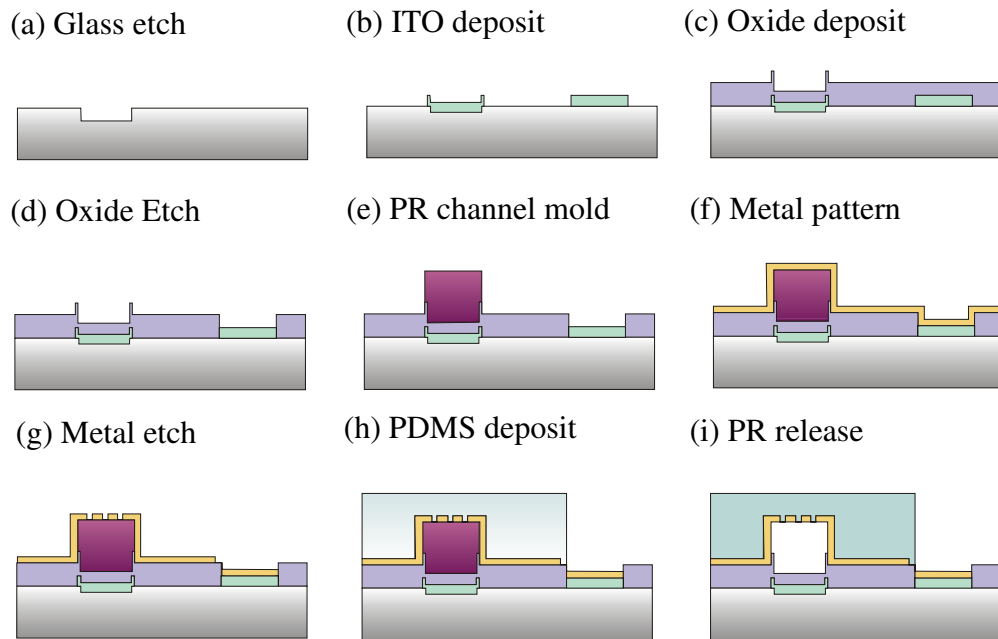


Figure 5.3: Fabrication flow. A 1 μm glass recess was etched to form a valve pocket.

5.4 Experiment Apparatus and Control Circuitry

Figure 5.4 shows the experiment apparatus of flow measurement by fluorescence or white-light microscopy on a Nikon TE-2000 inverted microscope. Food color (blue and yellow) and fluorescent dyes (fluorescein sodium and ruthenium tris(bipyridine) chloride, mixed with water into 1 mM concentration) were used respectively as visual indications of device actuation, flow direction and liquids mixing. Surfactant (Triton X-100) was mixed with water into 1% w/w to reduce surface tension between PDMS and pure DI water, and filled the device by capillary force. Flow rate measurement was performed by micro particle-imaging-velocimetry (μ -PIV) using polystyrene microspheres (Polysciences, 0.5 μ m diameter) mixed in the Trion-water solution. A syringe pump (KD Scientific) was used to flush and fill the fluidic network. The counter pressure could be generated by a nitrogen bottle or hydrostatic pressure for pressure and flow rate characterization. Two pressure transducers (Honeywell 40PC-150) were placed on both stream sides of the device to measure pressure drop across the device.

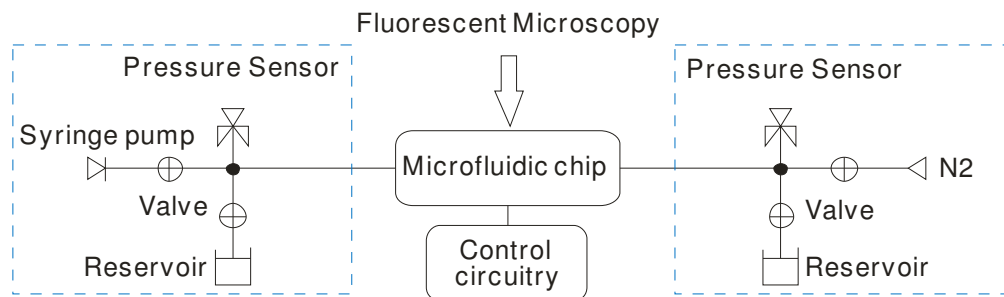


Figure 5.4: Diagram of experiment apparatus. The upstream and downstream fluidic network was only present for flow rate characterization.

The control circuitry, shown in Figure 5.5, is an improved eight channel version of the circuitry described in Chapter 4. A single valve requires a 5 MHz signal, 15-20 V amplitude signal to actuate. An initial 5 MHz, 5 V peak-to-peak signal was generated by a function/arbitrary waveform generator (Agilent 33250A, 80MHz) or an off-the-shelf oscillator IC, and amplified to 35-40 V peak-to-peak by either high speed IC amplifiers (Analog Devices AD815) or commercial RF amplifiers (Amplifier Research). This amplified signal was then sent to a pair of photovoltaic relay IC's (International Rectifier PVA13N) each of which was simultaneously controlled by two out-of-phase digital signals from the micro controller (Parallax BS2) respectively. The micro controller was programmed to provide the various actuation sequence outputs used for different actuation patterns.

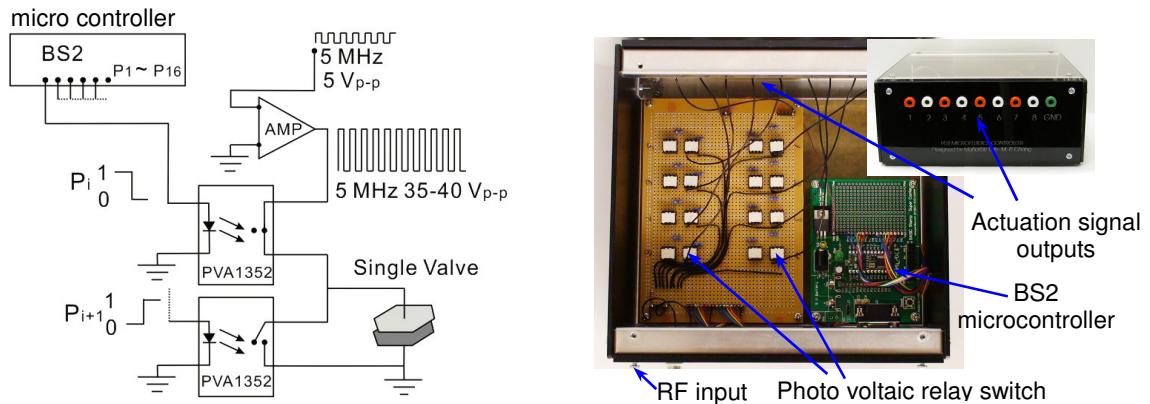


Figure 5.5: Control circuitry. A user-programmable micro controller (Parallax BS2) with 16 output ports was used to generate the synthesized actuation patterns for each valve component.

5.5 Valve and Pump Performance

We present valve and pump results for hexagonal arrays. Figure 5.6 (a) shows the basic valve operation of blue water. Figure 5.6 (b) shows the average flow rate versus actuation frequency of a three-valve peristaltic pump. Each component has a volume of about 0.4 nL. The maximum flow rate is 4.45 valve volumes/min (1.85 nL/min) at 0.37 Hz. After this frequency the flow rate decreased as frequency increased. Figure 5.6 (c) presents the time response of the pump flow rate at 1.1 Hz actuation frequency. The liquid movement was a pulsating flow, with a nominal flow rate about 1.5 nL/min. As expected, positive and negative velocity peaks were observed at the same frequency as the pump actuation frequency.

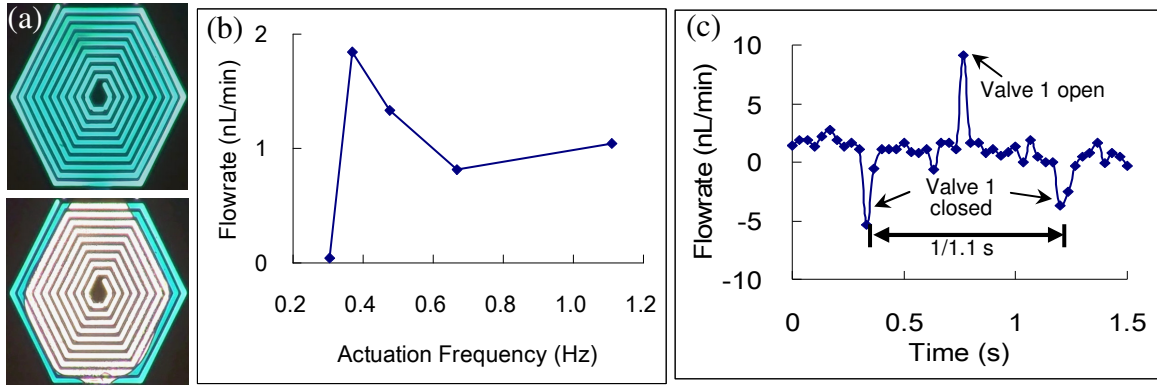
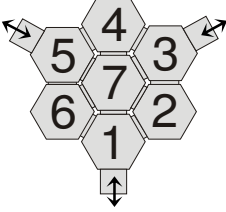
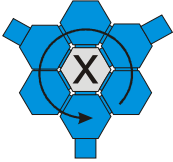
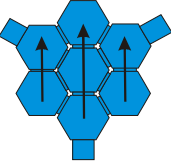
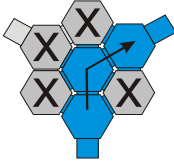
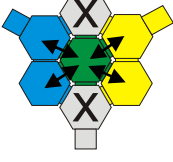
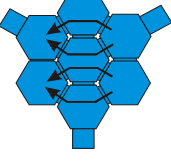
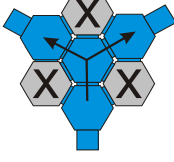


Figure 5.6: Valve and pump performance. (a) Top: an open valve filled with blue liquid. Bottom: as the valve closed, the liquid was expelled. (b) Average flow rate versus pumping frequency. The maximum average flow rate was found at 0.4 Hz actuation. After this frequency the flow rate decreased as actuation frequency increased. The measured flow rate was on the order of nL/min. (c) Flow rate versus time with 1.11 Hz actuation frequency. Peristaltic pumping generated pulsating flow, as indicated by the positive and negative spikes in the plot. The span between the two negative spikes was exactly the same time span as the actuation period (0.9 second).

5.6 Reconfigurable Distributed Microfluidics

The validity of reconfigurable distributed microfluidics is based on the ability to control each valve component independently, and generate various liquid manipulation patterns by applying different actuation sequences of a group of valves. With a reconfigurable system, many such manipulations are possible. Many flow directions and flow paths are possible simply by selecting which components will act in sequence as valves and peristaltic pumps. In addition, it is also possible to reconfigure the micro channels themselves by closing valves on both sides of a putative liquid transport path. Table 5.1 provides a basic scheme for some fundamental liquid manipulation and control patterns such as independent discrete valving, selective peristaltic pumping for switching fluids, and mixing of liquids.

Table 5.1
Device Operation and Actuation Patterns

 <p>Liquid inlet and outlet are valves 1, 3, and 5. Number notation is used through the chapter.</p>	 <p>Circulation</p>	 <p>Vertical Pumping</p>	 <p>Fluid Switching</p>
	 <p>Mixing</p>	 <p>Horizontal Pumping</p>	 <p>"Y" Pumping</p>

5.6.1 Distributed Valving

This section presents different patterns of reconfigurable distributed valving. Figure 5.7 shows a single-valve circulation pattern using a ruthenium tris(bipyridine) chloride fluorescent solution as a fluorescent indicator. Un-actuated valves are filled with dye and are bright in the micrographs; actuated devices are dark. Figure 5.7 (A) is an unactuated device as the background image, and images (B) – (G) show independent actuation of each valve; the white dashed circles indicate the actuated valve. The time span of each frame was approximately 150 ms, which is one single actuation time period. Actuation intervals can be altered by modifying the program for the microcontroller. The actuation voltage was 5 MHz 20 V peak to peak. The motion of fluorophore is more apparent when each actuation image is subtracted from the unactuation background (Figure 5.7 A), as grey scale images shown in Figure 5.7 (b) to (g). We also achieved two-valve circulation, full vertical and full horizontal manipulation patterns. These results are shown in Figures 5.8, 5.9 and 5.10. The time span of each frame was also 150 ms.

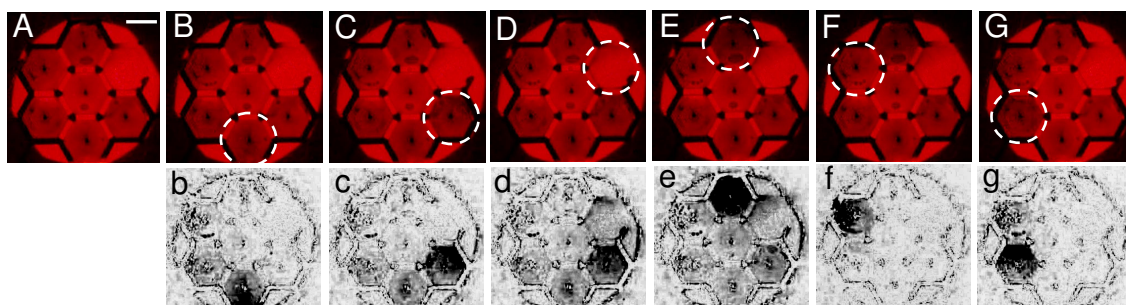


Figure 5.7: Single valve circulation actuation. Ruthenium dye was used for fluorescence microscopy. Image A is an un-actuated background image, B – G are each actuation as indicated by the white circle. Image b – g are the background-subtracted images of B – G respectively. Time frame is 150 ms and scale bar is 200 μm .

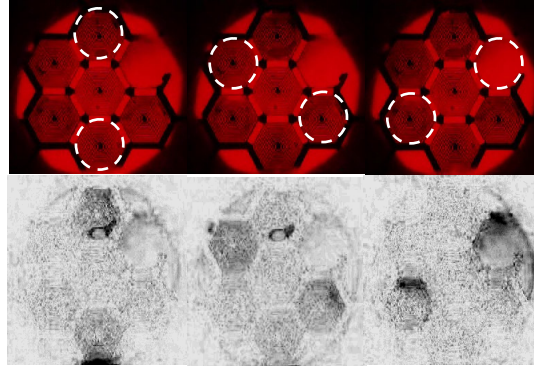


Figure 5.8: Pattern of two valve circulation actuation. Two diagonal valve components were actuated simultaneously and followed a counter-clockwise actuation sequence. The timeframe was 150 ms.

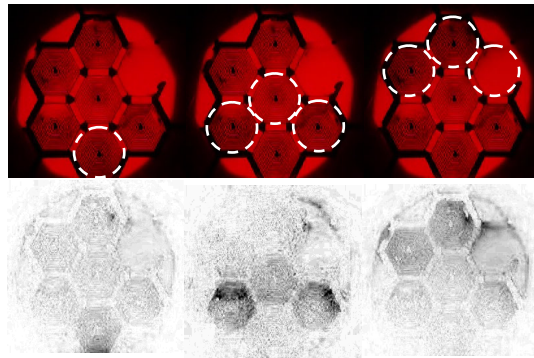


Figure 5.9: Pattern of full vertical actuation. Each row of valves was actuated sequentially for 150 ms.

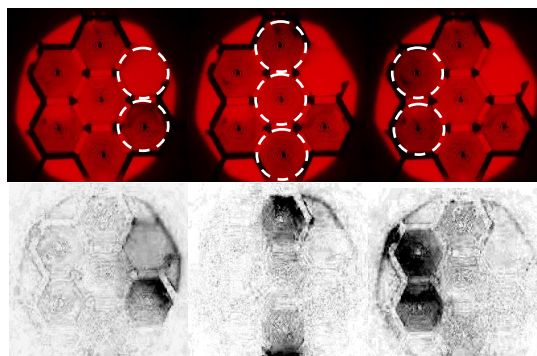


Figure 5.10: Full horizontal actuation from right to left. Time frame was 150 ms.

5.6.2 Fluidic Switch

Figure 5.11 shows flow splitting; images (A) – (F) are fluorescence micrographs (ruthenium fluorescent dye) each actuation frames and (a) – (f) are the corresponding background-subtracted images of each actuation step for better indication. Each time frame was 150 ms so a complete pumping cycle was 0.9 second (1.1 Hz frequency). Flow entered the device in valve 1 and was pumped out separately to two valve outlets 3 and 5. This was achieved by first shutting off valves 2, 4 and 6 (X marks in images (a) – (f)) to form barriers of liquid path, and using the other 4 valves 1, 7, 3 and 5 as a two-outlet peristaltic pump. The peristaltic actuation sequence was $1+3+5 \rightarrow 1 \rightarrow 1+7 \rightarrow 7 \rightarrow 3+5+7 \rightarrow 3+5$, as indicated by the white circles in Figure 5.10 A – F. It is also possible to reverse the flow splitting actuation sequence to operate the device as a flow concatenator.

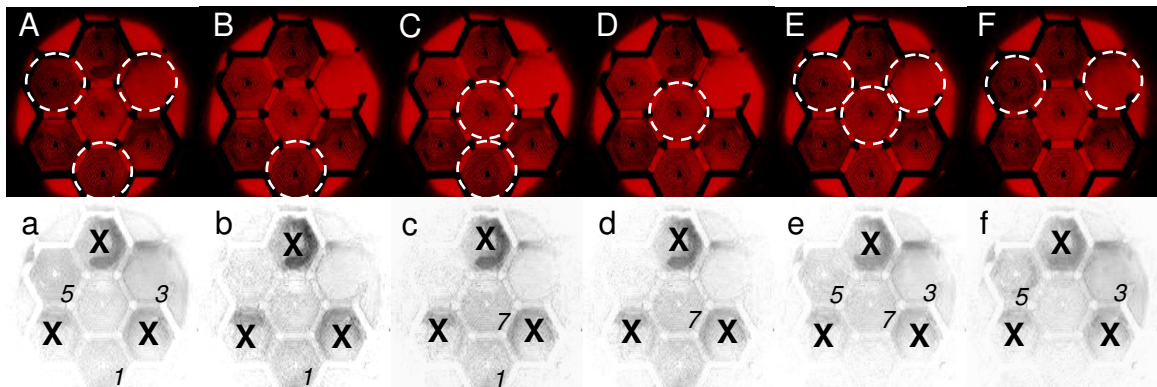


Figure 5.11: Flow splitting. Valves 1, 3, 5, 7 were operated as two-outlet peristaltic pump. White circles indicate the actuated valve components, while X denotes permanently closed valves (2, 4, 6) as barriers of liquid path. Image (a) – (f) are background-subtracted; numbers denote actuated components. Time frame was 150 ms, and pumping frequency was 1.1 Hz.

Figure 5.12 shows a fluid being switched to the top right outlet. This was achieved by permanently closing the left four valves (valve 4, 5, 6, and 7) and using the right three valves (valve 1, 2, 3) as a single peristaltic pump. The peristaltic actuation sequence was $1+2 \rightarrow 2 \rightarrow 2+3 \rightarrow 3 \rightarrow 1+3 \rightarrow 1$. Before actuation, a blue water was induced from valve 1 first, as indicated by the red arrow in Figure 5.12 (a), and the white arrow denotes the liquid outlet. The numbers show the un-actuated valve for that phase of the peristaltic pumping. The time period between each frame was 150 ms, and a complete pumping cycle was 0.9 second (1.1 Hz). It was noted that leakage (red arrowhead in Figure 5.12 (b)) occurred between the actuated chambers.

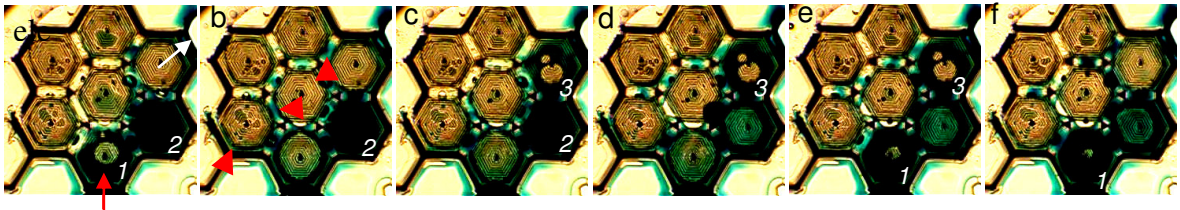


Figure 5.12: Fluid being switched to the right. Numbers in each frame denotes the un-actuated valve. The working liquid was blue water. Arrows in image (a) indicates liquid inlet and outlet, and arrowheads in (b) shows leakage between each actuated valve components. Time frame was 150 ms.

5.6.3 Mixing of Liquids

Figure 5.13 shows mixing of blue and yellow water (food color solution), and the time interval between each frame is 200 milliseconds. Blue color solution was induced into the device from valve inlet 3 (red arrow) and yellow solution was filled in valve 5 (blue arrow), respectively, to attain a half-half filled condition (Figure 5.13 (a), $t = 0$ s).

The device was then actuated at two diagonal valves sequentially (valve 5 and 2) to mix the two liquids. At $t = 200$ millisecond (Figure 5.13 (b)), valve 5 was actuated and the yellow liquid in that valve was pumped into the central valve (Figure 5.13 (c)) and started to mix with blue liquid. This semi-mixed liquid was kept moving into the lower-right valve (valve 2, Figure 5.13 (d), $t = 600$ ms). At $t = 800$ ms, valve 2 was actuated (Figure 5.13 (e)) liquid was pushed back into valve 7, and the blue and yellow liquids were actively mixed into green liquid (Figure 5.13 (f), $t = 1$ s). This process completed one mixing cycle, finished within 1 second, and the volume of mixed liquid was about 0.3 nL. This actuation cycle could be repeated to achieve better mixing results.

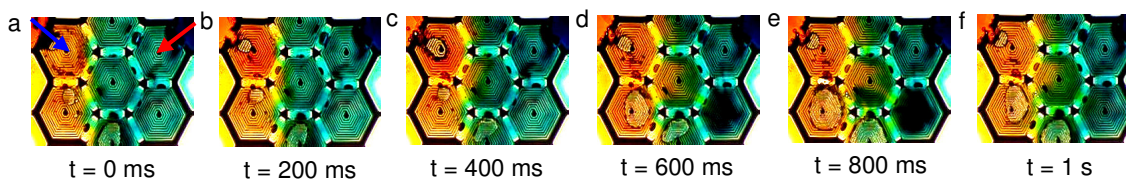


Figure 5.13: A single mixing cycle of blue and yellow liquids in the central chamber (valve 7). Blue liquid was filled from valve 3 and yellow liquid from valve 5. Valves 1 and 6 were permanently closed.

To quantify the mixing rate, we repeated the above procedure over many mixing cycles with 0.1 mM fluorescein solution and normal DI water. Here, the liquid concentration can be represented by the intensity of fluorescent light (higher intensity = higher concentration of fluorescein solution). The intensity histogram in a region of interest (central valve component in the device) shows the concentration distribution of mixed fluorescein solution.

Figure 5.14 presents the results of active mixing. The device was filled with fluorescein solution first and then DI water was filled in valve 5. For active mixing, valve 5 and 2 were actuated periodically at a 1 Hz frequency. As can be seen in Figures 5.14 (b) – (d), within 1 minute the central hexagon of the device became darker quickly and this is because the fluorescein concentration was decreasing due to DI water. Figure 5.14 (e) is the histogram of light intensity of the central hexagon, and it can be noticed that the intensity profile, originally more evenly distributed, started to generate a peak after 2 minutes and became more acute when $t = 3$ minutes. A perfectly mixed solution would exhibit a sharp intensity peak at the final intensity (leptokurtic distribution), while an unmixed solution would have a broad distribution (indicating both dark and bright areas exist in the area).

We also performed tests of mixing by pure diffusion as the control group. The 0.1 mM fluorescein solution was filled in the device first from valve 3 and the DI water was then filled from valve 5 inlet. The fluorescent micrograph of mixing by pure diffusion at different time is shown in Figure 5.15 (a) – (d). As in Figure 5.15 (b), after 5 minutes the DI water from the upper left inlet was mixed noticeably with the fluorescent solution and the brightness in the central chamber (red hexagon) was reduced. Figure 5.15 (e) shows the histogram of light intensity at different time (0, 5, 10, 15 minutes) corresponding to images (a) to (d). It can be clearly seen that the light intensity started to build up a peak value at about 10 minutes, which implies the two liquids were mixed to a certain concentration. This intensity peak is more prominent after 15 minutes.

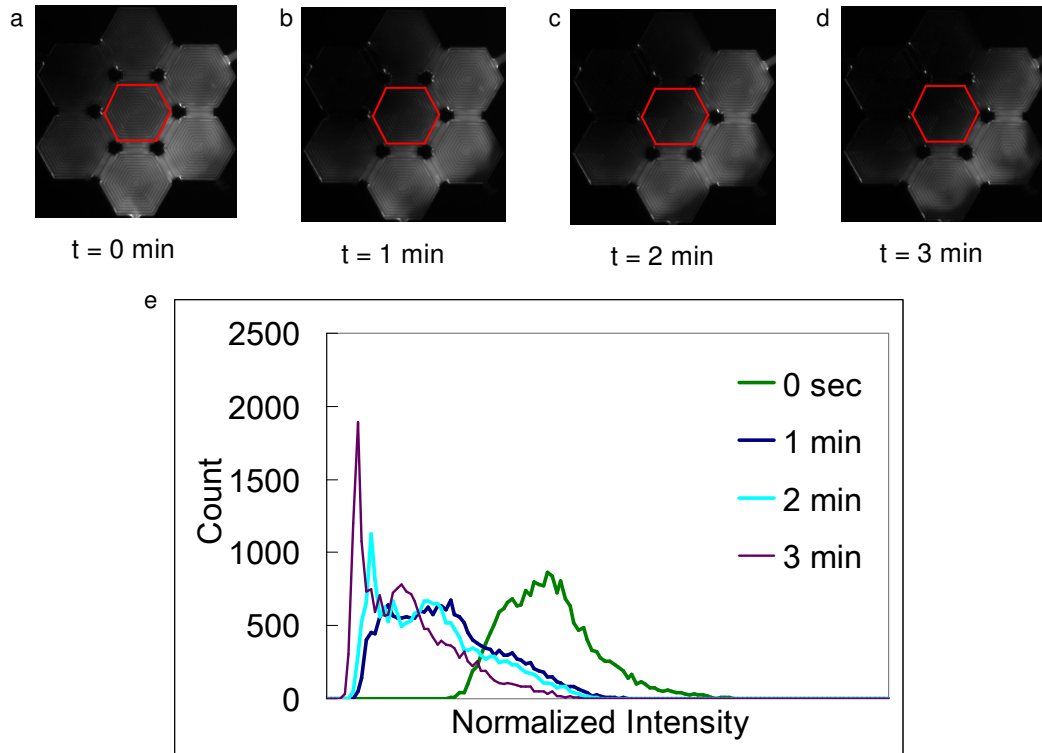


Figure 5.14: (a) - (d) fluorescent micrograph of active mixing by actuating diagonal valve pairs periodically. (e) Histogram of normalized light (concentration) intensity.

Figure 5.16 is the normalized average concentration of the central component valve (red hexagon in Figures 5.14 and 5.15) as a function of time. For active mixing the average concentration decreased to below 50% of initial within 2 minutes, while for diffusive mixing it took more than 10 minutes. Comparing the time required to produce a final concentration (red line), it is apparent that active mixing is about 5X faster in this device than mixing by pure diffusion of two liquids.

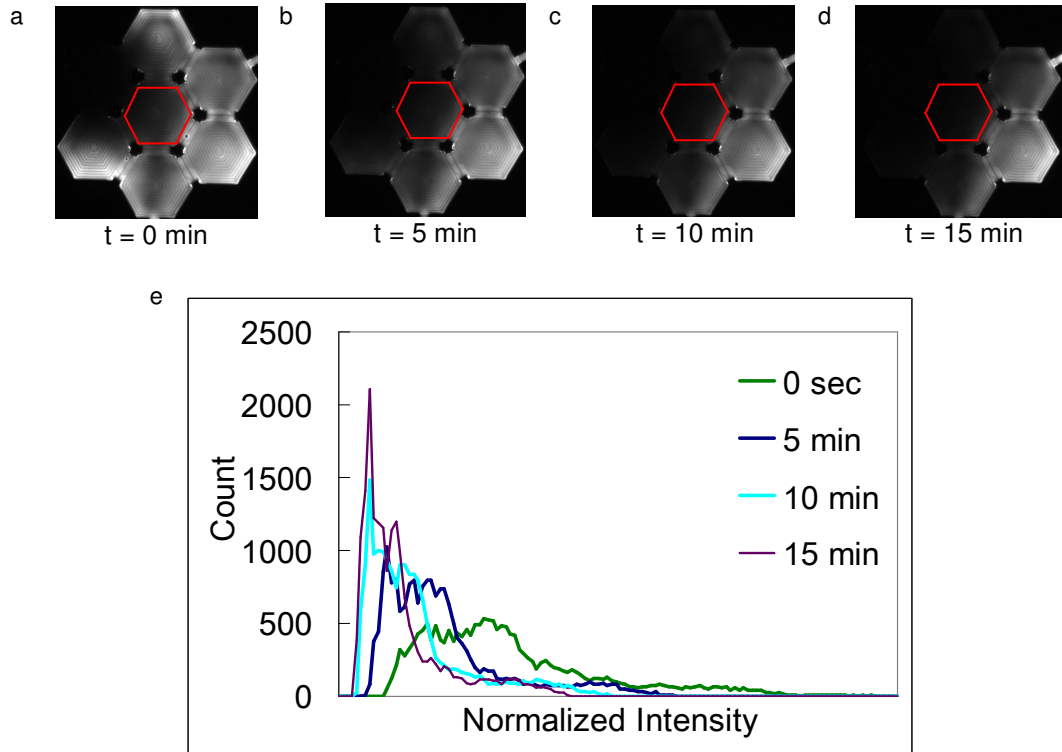


Figure 5.15: (a) - (d) fluorescent micrograph of passive mixing by pure diffusion. (e) Histogram of normalized light (concentration) intensity.

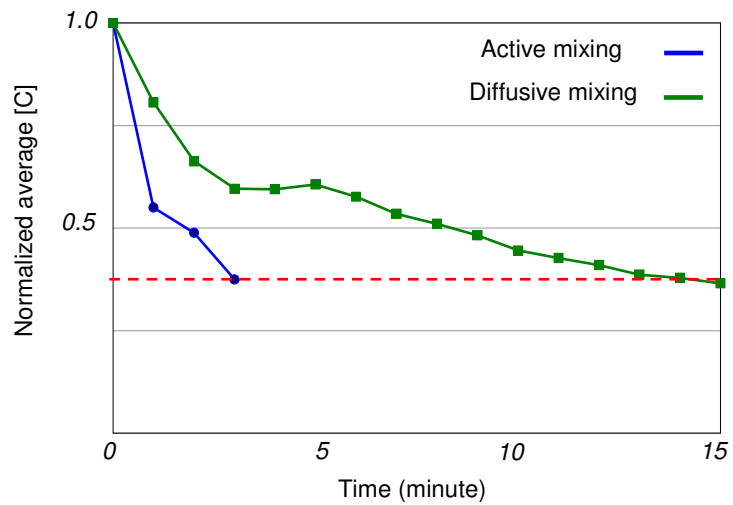


Figure 5.16: Normalized average concentration vs. time.

5.6.4 Comparisons with Current Technologies

Table 5.2 compares the reconfigurable microfluidic system with other current technologies. The developed system benefits from (1) completely post-fabrication reconfigurable (2) no pneumatic connections required and (3) system scalable into the nanofluidic regime. However this system requires an improved design of valve seats [9] to prevent leakage into closed components. A more simplified fabrication technique also needs to be established.

Table 5.2
Comparisons with Other Reconfigurable Microfluidic Systems

	PROS	CONS
Electrostatic PDMS	<ol style="list-style-type: none"> 1. Reconfigurable 2. No pneumatics 3. Scalable into nano regime 	<ol style="list-style-type: none"> 1. Processing 2. Needs better valve seats 3. E-field passed working liquid
Pneumatic PDMS Valves [10]	<ol style="list-style-type: none"> 1. Most mature technology 2. High flow rate and pressure 3. Fast prototyping process 4. Pure mechanical actuation 	<ol style="list-style-type: none"> 1. Many pneumatic connections 2. Complicated control
Braille-PDMS [36]	<ol style="list-style-type: none"> 1. Most mature technology 2. Fast prototyping process 3. Pure mechanical actuation 	<ol style="list-style-type: none"> 1. Scalability 2. Hand-assembly
Electrowetting on Dielectric [34, 69]	<ol style="list-style-type: none"> 1. Reconfigurable 2. No pneumatics 	<ol style="list-style-type: none"> 1. Easy surface contamination 2. E-field passed working liquid
Thermal Marangoni Flow [37]	<ol style="list-style-type: none"> 1. Reconfigurable 2. No pneumatics 	<ol style="list-style-type: none"> 1. Scalability 2. Hand-assembly

5.7 Summary of Contribution

This chapter presented an electrostatically-actuated reconfigurable elastomer microfluidic system. We have designed, fabricated, and tested an electrostatically-actuated reconfigurable elastomer distributed microfluidic system. This technology is compatible with modern PDMS microfluidics and CMOS drive voltages. The device requires no external pneumatic connections, operates at low voltage and is conceptually scalable to nanofluidic regime. We have demonstrated the device is capable of various liquid control patterns including multi-position serial valving, fluid switching, and mixing of liquids, all of which are essential liquid movement manipulations for large-scale parallel biological or biochemical analysis.

CHAPTER 6

CONCLUSION

6.1 Summary of the Thesis Work

This thesis work has demonstrated a new platform of electrostatically-actuated reconfigurable PDMS ‘wet’ micro actuators for high-density microfluidics. This technology was based on radio-frequency electrostatic actuation that overcame force shielding from the electric double layer. Potential electrochemistry involved in a typical electrical-coupled microfluidic system was avoided due to low actuation voltage. The developed metal-coated PDMS micro devices have demonstrated successful operation in a liquid environment at a low actuation pull-in voltage. The most important accomplishments of this thesis work include:

1. *Design and analysis of low voltage electrostatically-actuated micro actuator using in a ‘wet’ environment:* First, this thesis has developed a class of electrostatically-actuated low voltage elastomer-metal ‘wet’ micro actuator. Electrostatics is the most commonly used actuation mechanism in MEMS devices, but only limited to ‘dry’ environment applications. The developed microfluidic device has successfully demonstrated electrostatic actuation of pure metal and metal-coated PDMS plate by using radio-frequency signals. When actuated, the

top of the channel collapsed by electrical pull-in and sealed the gap. We used a 5 MHz signal which was sufficient to prevent electrical double layer screening of electrostatic force.

The desired pull-in voltage amplitude was successfully lowered to less than 20 V by effective design of the device geometry, material selection and fabrication control. We successfully developed fabrication techniques for manufacturing metal-coated PDMS membrane and release device by critical point drying to avoid device collapse by Laplace pressure. The fabricated device had low pull-in voltage. Only 13 V is needed for a metal-coated PDMS device, and as a result this voltage is low enough to be supplied by commercial available IC electronics.

Another important contribution of this work is the proposed technology has created a modified PDMS process compatible with conventional PDMS microfluidics. PDMS is the most used elastomer material in microfluidics due to its unique material property and fast prototyping by so-called “soft lithography” process. The PDMS process developed in this thesis work presented a method for manufacturing an electrical conductive PDMS which is excellent for using as structure materials for MEMS and microfluidic devices.

2. *Electrostatic PDMS micro valves and pumps*: The second part of this thesis work presented electrically-actuated micro valves and peristaltic pumps. A few improvements were made with a new device design: (1) the area of a single valve was reduced by 75% without increasing the pull-in voltage and (2) a new

PDMS (Dow Corning® WL-5351) was used for fabricating a thinner PDMS structure. These improvements successfully made the device scale from microfluidics down to nanofluidic regime. The fabricated micro valves and peristaltic pumps were characterized by using inverted fluorescent and white-light microscopy, and microspheres were used for flow rate measurement.

Since the micro valves and pumps only required low pull-in voltage to operate, AD-815 high speed IC amplifier was used to provide a 5 MHz 15 - 20 V peak-to-peak actuation signals. This signal was digitally synthesized by a user-programmable USB-interface micro controller and photovoltaic high-frequency relays. This on-chip control circuitry made possible building portable microfluidic systems. The low actuation voltage also prevented electrochemistry, such as electrolysis, from happening during actuation. In addition, the fabricated peristaltic pump was able to transport various liquid because the working mechanism was purely an electro-mechanical operation so the possible cross contamination made by chemical reaction was avoided.

3. *Reconfigurable elastomer microfluidics for high-density application:* The last part of this thesis work developed a new platform for reconfigurable distributed microfluidics by integrating the technologies developed in Chapters 3 and 4: electrostatically-actuated reconfigurable elastomer microfluidics for high-density applications. This reconfigurable microfluidic system was achieved by grouping individual self-actuating electrostatic micro valves for a very large scale integration. Since the each single valve could be controlled independently, the actuation sequence of the valves was executed by a program, coded accord-

ing to a user-predefined pattern, downloaded to a micro controller for signal synthesis, and sent to each valve devices. This developed reconfigurable system had several advantages such as (1) the system required no external pneumatic connection to operate (2) the voltage consumption was low enough to be powered by on-chip electronics. In addition, the design was changed to hexagon configuration because of several advantages: (1) more uniform membrane deflection (2) shorter liquid transport path, and (3) compact footprint.

This system demonstrated use as a reconfigurable discrete micro valve array. This included one-valve and two-valve circulation, full vertical and horizontal actuation. This system was also used for fluid switch for reconfigurable liquid transport. This was achieved by using the valve chambers on the liquid transport path as a peristaltic pump and closing the surrounding valve chambers as channel walls. Two typical patterns, flow splitter and flow bypass was demonstrated. The maximum flow rate was 4.4 valve volumes per minute. Further, this work illustrated the system could be operated as a mixer of liquids, which was 5X faster than mixing by pure diffusion. All these liquid manipulation and control capabilities of this reconfigurable distributed microfluidic system are essential for rapid parallel high-density biomedical, physical and chemical analysis.

6.2 Future Work Directions

The reconfigurable microfluidic systems demonstrated in this thesis provide a new platform to simultaneously manipulate multiple liquids for parallel analysis. The opera-

tion principle is simple and straightforward and the control is pure electrical with no external pneumatics. While this technology is promising for advancing microfluidic research testbed, the developed system is still on its prototyping stages and still has plenty of room for improvement in various aspects. Here we suggested a few possible directions for future work:

1. *Pursuit of '1 V' pull-in voltage:* The lowest pull-in voltage of the electrostatic microfluidic system developed in this thesis work was 13 V, which was not what was desired originally. The key to lower the pull-in voltage is to decrease the channel gap, increase the capacitor plate area, and reduce the structure rigidity. Our theoretical analysis proved that it was possible to build an electrostatic actuator with 1 V pull-in voltage, but fabrication hurdles prevented this from happening. The current process technique used photoresist as channel mold that was later released by soaking in acetone and thus the devices needed to be dried for releasing. This drying process was critical because the Laplace pressure generated by surface tension during the drying process tends to collapse the top capacitor membrane. Though critical point drying has been used to avoid this collapsing problem, it still did not solve the problem completely because PDMS is compressible so that the structure is too fragile for the high pressure (1350 psi, necessary to reach the super critical point of CO₂) generated during CPD process. To avoid this, we suggest using materials that can be dry-etched, such as poly-silicon or molybdenum (MO), as the sacrificial layer so that the PDMS micro structure can stand alone during the releasing process. This way it is possible to reduce the capacitor to sub-micron order and thus realize 1 V pull-in

voltage.

2. *Large-scale integration for high-density parallel analysis:* Another future work of this thesis is to realize a large-scale integrated system for parallel analysis. The electrostatic reconfigurable elastomer microfluidic system developed in Chapter 5 is ready for large-scale integration by grouping numerous seven-valve devices and extending as necessary, as shown in Figure 6.1. The integrated system can have multiple inlets and outlets for each sample, buffer and waste. By using the proposed actuation patterns, it is able to use this system to inject different samples, pre-mix and then pump to different valve chambers for simultaneous parallel analysis. This technology offers promise for high-density microfluidics to be used in biomedical applications such as cell culture, or analytical chemistry.

The developed microsystem is also compatible with other sensing technologies. For example, surface acoustic wave (SAW) sensor is a well-known technology for measuring material properties such as density and viscosity, which is known to be indicators of various pathological changes [85]. It is possible to install multiple one-port SAW sensors onto the reconfigurable microfluidic system as an active liquid sensor array, as shown in Figure 6.2. Each individual SAW sensor can be designed for different frequency band for specific sensing needs.

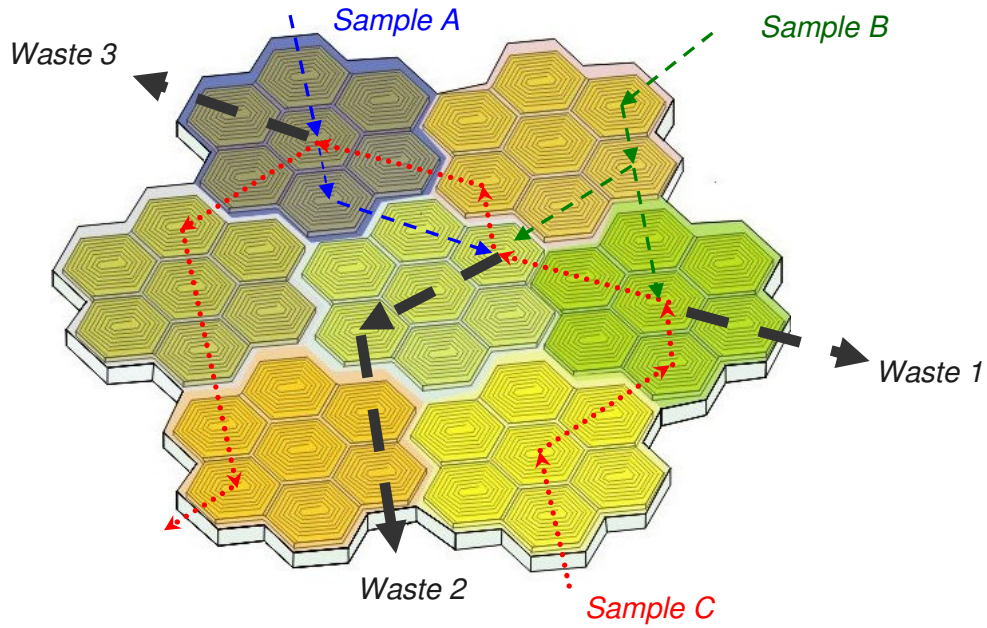


Figure 6.1: An example of reconfigurable VLSI microfluidic device with multiple inlets and outlets for samples/buffers (red, green, and blue lines) and wastes (grey lines). An integrated device has the capability to manipulate multiple liquids simultaneously, mix selectively, and transport pre-mixed liquids to different position for parallel analysis.

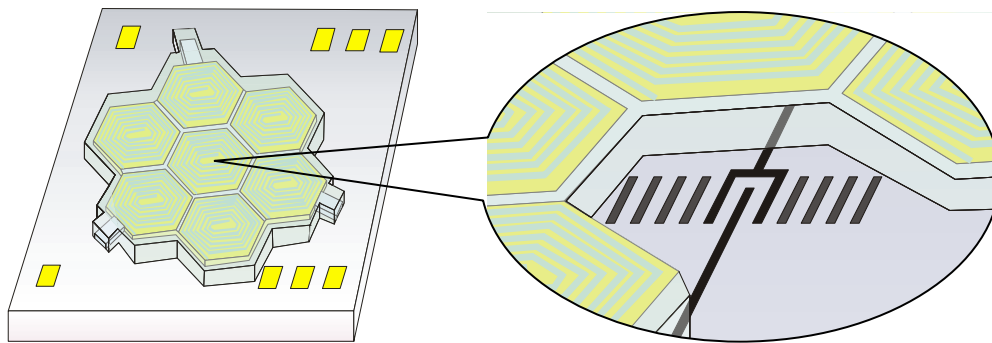


Figure 6.2: A conceptual view of reconfigurable liquid surface acoustic sensor (SAW) sensor array. The SAW sensor in the call-out is a one-port design.

6.3 Concluding Remarks

In conclusion, the work presented in this thesis has addressed many issues on electrostatics-coupled microfluidics that significantly add more dimensions to microfluidic research testbed. The issues include realizing radio-frequency electrostatic actuation for wet environment applications, self-actuating PDMS micro actuators with no external pneumatics, and high-density reconfigurable elastomer microfluidics. This work also presented a low power consumption microfluidic system that can be powered by on-chip electronics which is a key requirement for building portable microfluidic devices. In addition, this technology is not only compatible with conventional PDMS microfluidics but also scalable to the nanofluidic regime. By large-scale integration, this work demonstrates a promising technology that is suitable for rapid parallel biomedical, physical and chemical analysis. This thesis work, together with many other microfluidic research progresses in this field, proclaims that reconfigurable electrostatic elastomer microfluidics have the potential to advance to next generation micro total analysis systems.

APPENDICES

APPENDIX A

ELECTROKINETIC PUMPS

A.1 Introduction

Pumps are essential in our daily life. Our hearts pump blood throughout our body. A pumping station stores water in water towers that supply a municipality. Pumps inflate tires, basketballs, and balloons. Throughout history, pumps have been the most important devices to drive fluids to flow. As such, humans have invented and developed various types of pumps, and these pumps are omnipresent.

For the past two decades, Micro-Electrical-Mechanical-Systems (MEMS) has been a research field of intense scientific and engineering interest due to rapid advances in micro fabrication techniques. Micro pumps are one the first few devices being greatly investigated due to the importance for application in almost all fluidic devices^{1,2}. The exploration of micro pumps has recently accelerated due to interest in chemical, biochemical and biological analysis or more generally, Micro Total Analysis Systems (μ TAS)³. Such analysis systems not only possesses advantages in size and portability of the devices but also benefits from shorter analysis times, smaller sample sizes and massively parallel analysis. With a vast improvement in functionality, microfluidic devices have been fabricated to accurate fluid control within small quantities ranging from micro-liters to pico-

¹ P. Woias, Microfluidics and BioMEMS, Proceeding of SPIE Vol. 4560 (2001) 39

² D. J. Laser, and J. G. Santiago, J. of Micromechanics and Microengineering Vol.14 (2004) R35

³ A. Manz, S. J. Harrison, E. M. J. Verpoorte, J. C. Fettinger, A. Paulua, H. Ludi, and H. M. Widmer J. chromatogr. A Vol. 593 (1992) 253

liters to address the need for precise on-chip fluid control systems. At the heart of this fluid control system is a whole new generation of micro pumps.

Various micro pumps have been developed according to different working principles. Based on these operating principles, micro pumps can be classified in two major categories: mechanical micro pumps and non-mechanical micro pumps⁴. Mechanical micro pumps usually consist of moving parts, and energy generated in the movement of these moving parts leads to the liquid movement. On the contrary, there are generally no moving parts in a non-mechanical micro pump. The liquid movement is mostly resulted from due to direct energy transfer such as chemical or electrical energy.

A typical mechanical micro pump is the reciprocating displacement micro pump. The check-valve micro pump is the most general reciprocating micro pump; it consists of a driving unit (a diaphragm or a membrane) that generates a stroke into a pump chamber with a fixed dead volume. Two passive valves control the inlet and outlet of the micro pump^{5,6,7}. Another type of reciprocating displacement micro pump is the peristaltic micro pump. In contrast to the check-valve micro pump, the movement of liquid in a peristaltic micro pump is created by squeezing the liquid in the pump chamber so it flows; no valve is required^{8,9,10}. There are some other mechanical micro pumps utilizing different

⁴ N. Nguyen, X. Huang, and T. K. Chuan, *J. Fluids Engineering* Vol. 124 (2002) 384

⁵ M. Richter, R. Linnemann, and P. Woias, *Sensor Actuat A-Phys* Vol. 68 (1998) 480

⁶ R. Zengerle, J. Ulrich, S. Kluge, M. Richter and A. Richter, *Sensor Actuat A-Phys* Vol. 50 (1995) 81

⁷ E. Meng, X.-Q. Wang, H. Mark, and Y.-C. Tai, *Proc. MEMS 2000*, pp62

⁸ J. G. Smits, *Sensors Actuat.* Vol. 15 (1988) 153

⁹ C. Grosjean, and Y.-C. Tai, *Inter. Conf. On Solid-State Sensors and Actuators* (1999) 1776

¹⁰ C. Cabuz, E. I. Cabuz, W. R. Herb, T. Rolfer, and D. Zook, *Inter. Conf. On Solid-State Sensors and Actuators* (1999) 1890

operating principles such as rotary micro pumps¹¹ and ultrasonic micro pumps^{12,13}.

As to the non-mechanical micro pumps, electrohydrodynamic pumps operate using the electrostatic force to drive dielectric fluids. An electrode array is sequentially switched so that the interaction of the electrostatic force and the ions in the solution causes the fluid to flow^{14,15,16}. Alternatively, electrokinetic pumps (also known as electroosmotic pumps, EK pumps, or EO pumps) function when an electrical field is acting on a conductive liquid that is in contact with a solid surface^{17,18,19}. This mechanism is termed electroosmosis. Details of the electrokinetic pumps will be addressed in subsequent sections.

A.2 Electrokinetic Pumping

The electrokinetic pump has several advantages over other types of micro pumps. First, there is no moving part in an electrokinetic pump so theoretically there would be no mechanical power loss. Secondly, unlike most pumps, the output of the electrokinetic pump is a continuous flow (non-pulsatile), and the flow rate is proportional to the current through the pump body, and can easily be adjusted by controlling a voltage or current source. At the same time, electrokinetic pumps have a response time (to a change in ap-

¹¹ J. Doepper, M. Clemens, W. Ehrfeld, S. Jung, K. P. Kaemper, and H. Lehr, *J. Micromech. Microeng* Vol. 7 (1997) 230

¹² R. M. Moroney, R. M. White, and R. T. Howe, *IEEE 4th Int. Workshop on MEMS* (1991) 408

¹³ N. T. Nyugen, A. H. Meng, J. Black, R. M. White, *Sensors Actuat. A-Phys* Vol. 79 (2000) 115

¹⁴ A. Richter, A. Plettner, K. A. Hofmann and H. Sandmaier, *Sensor Actuat A-Phys* Vol. 29 (1991) 159

¹⁵ G. Fuhr, T. Schnelle, and B. Wagner, *J. Micromech. Microeng.* Vol. 4 (1994) 217

¹⁶ J. Darabi, M. M. Ohadi, and D. DeVoe, *J. Microelectromech. Syst.* Vol. 10 (2001) 98

¹⁷ P. H. Paul, D. W. Arnold, and D. J Rakestraw, *Proc. Micro Total Analysis Systems* 1998

¹⁸ C.-H. Chan, and J. G. Santiago, *J. Microelectromech. Syst.* Vol. 11 (2002) 672

¹⁹ Y. Takamura, *Proc. Micro Total Analysis Systems* 2001

plied current) on the order of microseconds, which probably makes them the fastest-response hydraulic devices ever constructed. In addition, electrokinetic pumps can be constructed in various configurations depending on the particular performance objective, which offers a wide potentiality of applications.

The capability for liquid transport via electroosmotic flow has long been known²⁰, but not until the late 1990's was the ability of generating high electroosmotic pressure reported. In 1998, Paul et al reported electrokinetic pumps capable of very high pressures in excess of 10,000 psi²¹. Since then applications of electrokinetic pumps for high performance liquid chromatography (HPLC)²² and heat exchange²³ have been presented, and exploration of different applications continues to develop.

A.2.1 Operation Principle

The operating principle of electrokinetic pumps is based on the movement of liquid due to an electric potential gradient: this phenomenon is termed electroosmosis. Electroosmosis is one of the electrokinetic phenomena²⁴. The other electrokinetic phenomena are electrophoresis, streaming potential, and sedimentation potential. The definitions of these electrokinetic phenomena are:

- (1) Electroosmosis: the movement of liquid relative to a stationary charged surface under an electric field.
- (2) Electrophoresis: the movement of a charged species relative to a stationary liquid

²⁰ C. L. Rice, R. Whitehead, J. Phys. Chem. 69 (1965) 4017

²¹ P. H. Paul, D. W. Arnold, D. J. Rakestraw, Proc. of Micro Total Analysis Systems (1998) 49

²² Y. Fintschenko, A. van den Berg, J. Chromotogr. A 819 (1998) 3

²³ L. Jiang et al, IEEE Trans. Comp. Pack. Tech. 25, no.3 (2002) 347

²⁴ R. F. Probstein, Physicochemical Hydrodynamics- An Introduction, 2nd Ed (1994), John Wiley & Sons

under an electric field.

- (3) Streaming potential: the electric field established due to the movement of liquid relative to a stationary charged surface; opposite to electroosmosis.
- (4) Sedimentation potential: the electric field established due to movement of charged species relative to a stationary liquid; opposite to electrophoresis.

The electrokinetic pump operates using a very simple mechanism: electro-osmotic flow is induced down a very narrow microfluidic channel. Pressure can be developed at the outlet until the pressure-driven back flow rate is equal and opposite of the electro-osmotic flow rate. Figure A.1 shows a schematic and operating principle of an electrokinetic pump.

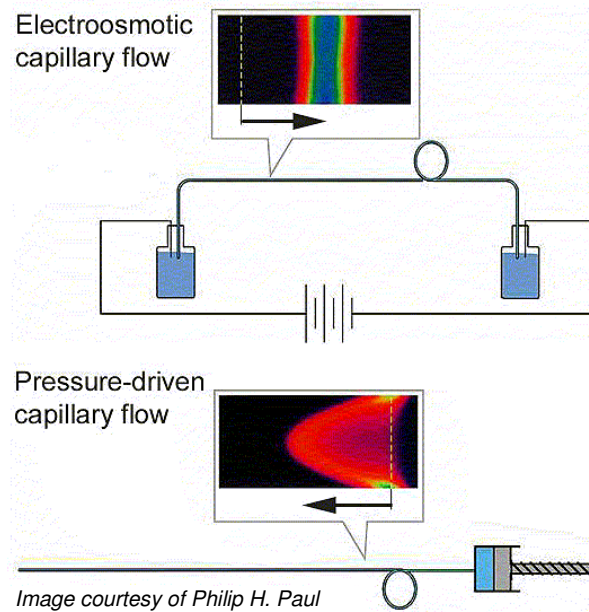


Figure A.1: The operating principle of electrokinetic pumps: When an electrical potential gradient is applied across the two reservoirs, the electroosmotic flow (EOF) is induced toward the negative direction of the E-field. The electroosmotic flow will cause a pressure increase in the down stream, which leads to a counter flow driven by pressure (PDF). Superposition of the profiles of the EOF and PDF yields the overall movement profile.

The electroosmosis phenomenon arises from complex electrical, chemical, and mechanical mechanisms. A general theoretical analysis of electrokinetic pumps is discussed in this section: a model of electroosmotic flow in planar micro channels is addressed. The relationship between counter pressure and voltage can be developed by linearly superposing the electroosmotic flow with the pressure-driven counter flow. Calculations of time constants for buffer depletion and bubble generation are presented for the time-scale evaluation.

A.2.2 Electrical Double Layer

The interface between the liquid and the surface of micro channels is composed of several layers. For example, the surface of borosilicate glass is negatively charged, and this negatively charged surface would attract counterions (cations) from the bulk solution to the surface and hence forms an electrical double layer (EDL). One characteristic of the EDL is that the inner layer (solid surface side) is stationary and the outer surface (liquid side) is mobile. The electric potential of this mobile layer is called zeta potential. From *Debye-Hückel theory*²⁵ one can evaluate the thickness of the EDL.

The electric potential ψ governed by the one dimensional Poisson equation is stated as

$$\frac{\partial^2 \psi}{\partial x^2} = -\rho_c / \epsilon \quad (\text{A.1})$$

where ρ_c is the electric charge density ($C \cdot m^{-3}$), and ϵ is the relative permittivity of the liquid. x is the Cartesian coordinate normal to the surface of the channel, as shown in Figure A.2.

²⁵ P. W. Debye, and E. Hückel, Phys. Z. Vol. 24, (1923) 185

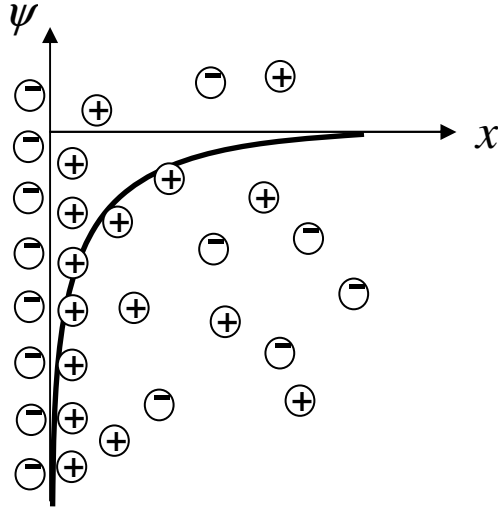


Figure A.2: Distribution of electric potential ψ by a negatively charged surface

The charge density distribution ρ_c follows the Boltzmann statistics:

$$\rho_c = e \cdot \sum_i c_i \cdot z_i \cdot \exp\left(\frac{-z_i \cdot e \cdot \psi}{k_B \cdot T}\right) \quad (\text{A.2})$$

Here e is the elementary charge, c_i and z_i are the molar concentration and charge number of the species i , k_B is the Boltzmann constant ($1.381 \times 10^{-23} \text{ JK}^{-1}$) and T is the temperature (K). Debye-Hückel theory provides an analytical solution for the case of low surface potentials such that $ze\psi/k_B T \ll 1$, and thus the exponential term in the Boltzmann equation, can be expanded as $1 + (-z_i \cdot e \cdot \psi / k_B \cdot T)$. Hence the Boltzmann equation can be rewritten as

$$\rho_c = e \cdot \sum_i c_i \cdot z_i \cdot \left(1 + \frac{-z_i \cdot e \cdot \psi}{k_B \cdot T}\right) = e \cdot \sum_i \left(\frac{-z_i^2 \cdot e \cdot c_i \cdot \psi}{k_B \cdot T}\right) = \frac{e^2 \cdot \psi}{k_B \cdot T} \sum_i (-z_i^2 \cdot c_i) \quad (\text{A.3})$$

Combine Equations (A.1) and (A.3) and yield

$$\frac{\partial^2 \psi}{\partial x^2} = \frac{1}{\lambda_D^2} \cdot \psi \quad (\text{A.4})$$

where $\lambda_D = \sqrt{\frac{k_B \cdot T \cdot \epsilon}{e^2 \cdot \sum_i z_i^2 \cdot c_i}}$ is the Debye length, which provides an estimate of the thick-

ness of the electrical double layer. Integrating Equation (A.4) and applying the boundary condition $\psi = \zeta$ (zeta potential) at $x=0$ and $d\psi/dx=0$ as $x \rightarrow \infty$ one can formulate the potential ψ as

$$\psi = \zeta \cdot \exp\left(-x/\lambda_D\right) \quad (\text{A.5})$$

From Equation (A-5) it is found that the potential decays exponentially with distance away from the channel surface.

A.2.3 Electroosmotic Flow in a Planar Micro/Nano Channel

As described in the previous section the EDL is composed of a stationary layer and a mobile layer. When an electrical field is applied, the mobile layer (positively charged) starts to move along the direction of the field and the drag force causes movement of the liquid inside the micro channel. For simplicity here we consider a one-dimensional model describing electroosmosis: electroosmotic flow flowing through a planar slit. As shown in Figure A.3, a uniform electric field is applied toward the positive y direction. Since the surface is negatively charged, the direction of EOF would be along the positive y direction as well. The equation of motion is stated as

$$\rho \frac{D\vec{u}}{Dt} = -\vec{\nabla}P + \rho_c \cdot \vec{E} + \eta \cdot \nabla^2 \vec{u} \quad (\text{A.6})$$

where \vec{u} is the velocity of EOF, ρ is the density and η is the dynamic viscosity of the liquid. Assuming there is no pressure gradient, $\vec{\nabla}P$, the electric field would be the only driving force for the liquid to move. Generally speaking, the Reynolds number is very small in micro scale devices, which implies that the viscosity dominates the flow so the inertia term can be neglected. Also note that the case considered here is $h \ll w$ and $h \ll l$, the flow field can be described as one-dimensional and the equation of motion can be rewritten as

$$\rho_c \cdot E_y + \eta \frac{d^2 u_y}{dz^2} = 0 \quad (\text{A.7})$$

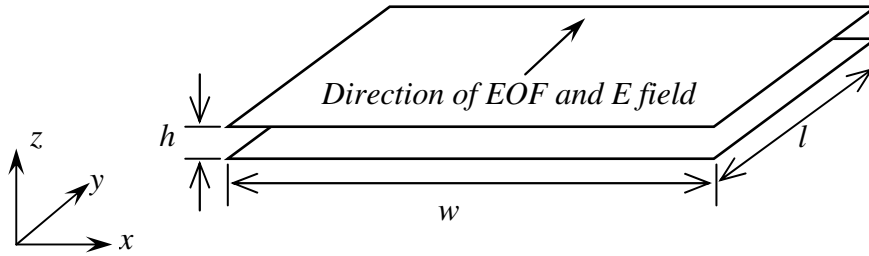


Figure A.3: Configuration of EOF in a planar slit: The E-field is along positive y direction so the EOF is moving toward the positive y direction as well. For the case of a planar slit, it is noted that $h \ll w$ and $h \ll l$.

The charge density in Equation (A.7) can be replaced with the potential using the Poisson equation, such that

$$-\epsilon \cdot E_y \cdot \frac{\partial^2 \psi}{\partial z^2} + \eta \frac{d^2 u_y}{dz^2} = 0 \quad (\text{A.8})$$

Integrating Equation (A.8) twice with respect to z; applying the boundary condition

$u_y = 0$ and $\psi = \zeta$ at, $z = [0, h]$ yields the EOF velocity profile

$$u_y = \frac{\varepsilon \cdot E_y}{\eta} \cdot (\psi - \zeta) \quad (\text{A.9})$$

The volume flow rate Q_{EOF} of EOF could be obtained by integrating Equation (A.9) from $z = 0$ to $z = h$ and is expressed as

$$Q_{EOF} = -\frac{\varepsilon \cdot \zeta \cdot E_y}{\eta} \cdot A \quad (\text{A.10})$$

where A is the cross-sectional area of the planar slit channel. The negative sign is because the zeta potential of the surface is negative (negatively charged surface). Dividing the EOF flow rate by the cross-section area yields the average velocity of the electroosmotic flow, and is expressed as

$$\bar{u}_{EOF} = -\frac{\varepsilon \cdot \zeta \cdot E_y}{\eta} \quad (\text{A.11})$$

This equation is also known as the Helmholtz-Smoluchowski equation.

A.2.4 Counter Pressure and Pressure Driven Flow

Laminar flow profiles in various channel shapes have long been understood. The reader is referred to standard fluid mechanics textbooks for detailed derivations. The average flow rate of a plane Poiseuille flow is

$$Q_{PlanePDF} = \frac{-h^2}{12 \cdot \eta} \cdot \nabla P \cdot A \quad (\text{A.12})$$

Pressure driven flow in a round pipe is termed circular Poiseuille flow, and its average flow rate is

$$Q_{CircularPDF} = \frac{-d^2}{32 \cdot \eta} \cdot \nabla P \cdot A \quad (A.13)$$

where d is the diameter of the pipe. For an electrokinetic pump, it is known that the maximum pressure is attained when the flow rate of the electroosmotic flow equals that of the counter Poiseuille flow, which leads to the relationship between the max pressure and the electric field

$$P_{max} = \frac{12\varepsilon \cdot \zeta}{h^2} \Delta\phi \quad (A.14)$$

in a planar slit, or

$$P_{max} = \frac{32\varepsilon \cdot \zeta}{d^2} \Delta\phi \quad (A.15)$$

in a circular pipe. Here $\Delta\phi$ is the potential difference across the micro channel. From Equations (A.14) and (A.15) it is observed that the channel diameter or channel height is a powerful scaling factor in obtaining the maximum pressure. For example, it is theoretically possible to achieve 10 psi/volt if the diameter is 200 nm.

A.2.4 Efficiency of Electrokinetic Pumps

The efficiency χ of electrokinetic pumps can be expressed as

$$\chi = \frac{P \cdot Q}{I \cdot V} \quad (A.16)$$

where P is the counter pressure, Q is the flow rate, V is the applied voltage, and I is the current. J. Y. Min et al²⁶ reported a model for computing efficiency of electrokinetic pumping in various configurations including circular, planar slit and rectangular and sug-

²⁶ J. Y. Min, E. F. Hasselbrink, S. J. Kim, Sens. Act. B 98 (2004) 368

gested that an efficiency of 15% is theoretically possible. S. K. Griffiths²⁷ presented the efficiency of electrokinetic pumping at a condition of maximum work by employing the full Poisson-Boltzmann equations and observed that the efficiency of this maximum work depends on normalized zeta potential, normalized Debye length thickness, and the nominal ratio of convective to conductive currents. This ratio is termed the *Levine number*.

A.3 Overview of Challenges with Electrokinetic Pumping

Although electrokinetic pumping is a promising pumping technology capable of generating small flow rate and pumping against high counter pressure, several significant challenges remain. The electrodes immersed in the liquid cause electrolysis of the working liquid, which results in generation of gas bubbles and pH changes, and hence deteriorates the performance of the electrokinetic pumps. The material properties of the working liquid (pH, conductivity, composition) will change due to the direct chemical reactions between the liquid and electrodes. This observation implies the need for isolation of working and pumping liquid and currently hampers widespread application of electrokinetic pumping.

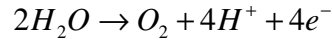
A.3.1 Electrolysis, Bubble Generation and pH Evolution

Electrolysis is the process by which electric current passed through a substance causes a chemical change, via the gaining (reduction) or losing (oxidation) of electrons. Since electroosmotic flow can only be induced under an electric field, electrolysis is not

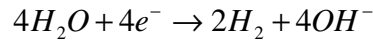
²⁷ S. K. Griffiths, R. H. Nilson, *Electrophoresis* (2005) 351

avoidable in the electrokinetic pump. One obvious result of electrolysis is the generation of oxygen at the anode and hydrogen at the cathode. In this section quantification of bubble generation and pH evolution is addressed in detail.

Consider an electrokinetic pump with platinum wire as working electrodes and de-ionized water as working liquid. When applying a DC voltage across the electrodes, a current flow through the channel of the electrokinetic pump. At this point the chemical reaction at the anode is



and the reaction at the cathode is



which indicates that oxygen will be generated at the anode and hydrogen will be generated at the cathode. As also can be seen from these two equations, production of protons causes a pH decrease at the anode and hydroxyl ions results in a pH increase.

The volume of generated gas can be obtained readily; however, the estimation of a time constant for bubble generation is a more effective way for evaluation. The time constant for bubble generation can be calculated according to Faraday and Henry's laws: Faraday's law relates the electrical current to the moles of generated chemical product, and Henry's law provides the quantity of gas that can be stored in a liquid for which the volume is known. Note that specific chemical reactions between electrodes and electrolyte are part of a complicated process and consist of several different types of electron-exchange mechanism. For simplicity, here we consider only faradaic processes; i.e., the

rate of production of oxygen and hydrogen is proportional to the current. Hence the rate of gas production can be expressed as

$$\dot{V}_{gas} = \frac{r_{gas/e} \cdot I \cdot \rho_{gas}}{F} \quad (\text{A.17})$$

where \dot{V}_{gas} is time rate of volume of gas generated at the electrode, ρ_{gas} is the coefficient of gas volume per mole (24.5 liter/mole), and $r_{gas/e}$ is the ratio of the stoichiometric coefficient of the gas and the electron ($r_{gas/e} = 0.25$ for oxygen, and $r_{gas/e} = 0.5$ for hydrogen). I is the electrical current and F is the Faraday's constant ($96500 \text{ C} \cdot \text{mol}^{-1}$).

Since both hydrogen and oxygen dissolve readily in water, neither oxygen generated at the anode nor hydrogen at the cathode forms gas bubbles immediately. Generally gas bubbles are formed when the molar concentration of a gas in a liquid exceeds its solubility. The solubility of gas in a liquid is governed by Henry's Law, which states

$$[A]_{aq} = \kappa_h \cdot p(A)_{gas} \quad (\text{A.18})$$

Here $[A]_{aq}$ is the molar concentration of gas solved in the liquid, $p(A)_{gas}$ is the partial pressure of gas A, and κ_h is the Henry's constant (for hydrogen $\kappa_h = 0.00078 \text{ M/atm}$; for oxygen $\kappa_h = 0.0012 \text{ M/atm}$)²⁸. The time constant of gas generation τ_G can be then obtained

$$\tau_G = \frac{[A]_{aq} \cdot \bar{V}}{\dot{V}_{gas}} \quad (\text{A.19})$$

²⁸ R. Sander (1999) Compilation of Henry's Law Constants for Inorganic and Organic Species of Potential Importance in environmental Chemistry (Version 3)
<http://www.mpch-mainz.mpg.de/~sander/res/henry.html>

Electrolysis also leads to pH changes. As described in Section A.2, the velocity of electroosmotic flow is proportional to the zeta potential of the electric double layer. For silica or borosilicate glass, the zeta potential is about -75 mV at pH 7 and increases gradually as pH decreases²⁹. As pH approaches 3, the zeta potential is almost zero, which results in suppression of electroosmotic flow. To avoid drastic change of pH, a buffer solution is generally used as the working liquid for electrokinetic pumping, but the capacity of buffer solutions is limited and will be consumed up eventually.

The exact pH can be calculated if the reaction of electrode and electrolyte is known. However a more effective way for pH estimation is to calculate the time constant of pH change by one unit (either increase or decrease) in a faradaic process, and this time constant can be formulated as

$$\tau_{pH} = \frac{\bar{V} \cdot c \cdot F}{2 \cdot I} \quad (\text{A.20})$$

Again F is the Faraday Constant ($96500 \text{ C} \cdot \text{mol}^{-1}$) and \bar{V} is the volume of the buffer solution in the electrode reservoir. c is the molar concentration of the buffer. The “2” in the denominator is because the pH change might be either an increase or a decrease— that is, this equation presumes that the buffer starts at its midpoint. It is found that the time constant is proportional to the amount of buffer and its molar concentration. Unfortunately, the buffer concentration is also proportional to its conductivity, and so increasing the buffer concentration also increases the current. Thus there is no improvement in the time constant to be gained by increasing the buffer concentration if the same buffer solution is used as the pump working fluid.

²⁹ B. J. Kirby, E. F. Hasselbrink, *Electrophoresis* Vol.25 (2004) 187

A.3.2 Isolation of Pumping and Working Liquid

Another drawback of electrokinetic pumping is the lack of isolation between working liquid and pumping liquid. Unlike mechanical micro pumps, the working liquid in the electrokinetic pump is directly involved in the pumping mechanism (chemically reacting with the electrodes). The material properties and composition of the working liquid alter due to reactions with the electrodes, which is unsuitable for most biomedical or lab-on-a-chip applications. This remains a challenge in designing for certain applications.

A.3.3 Solution Strategies

The application hurdles discussed above lead to a major challenge for electrokinetic pumping devices: longevity. For short-term operation (within minutes) and moderate current (generally on the order from μA to mA), the performance of electrokinetic pumping is rarely significantly affected by bubble formation and pH evolution since the time constant is relatively small. However performance gradually degrades when operating pumps for extended periods of time. In addition, the composition and material properties of the working liquid also significantly change after long-term pumping.

There are several ways to prevent or ameliorate the effects of bubble formation in electrokinetic pump designs. One straightforward idea is to separate the electrode chamber and the pumping chamber with a salt bridge. The salt bridge can be an ion exchange membrane or porous polymer monolith. The salt bridge needs to be of high hydraulic resistance (to minimize flow leakage from pumping chamber into the electrode chamber, or vice versa), and to be of low electrical resistance (allowing the electrical current to pass through without difficulty). Another method is to utilize gasless electrodes, and this is

usually related to electrolyte choice. That is, a number of ionic species can be added to the solution that can exchange electrons with a metal wire without producing gas. A simple example is the ferro-/ferricyanide redox couple which can exchange electrons according to $\text{Fe}_{\text{III}}(\text{CN})_6^{3-} + e^- \leftrightarrow \text{Fe}_{\text{II}}(\text{CN})_6^{4-}$. While searching for appropriate combinations of electrode and electrolytes, one must keep in mind that not all electrolytes are suitable in electrokinetic pumping. The working liquid needs to have a pH around 6~10 in order to strongly support EOF on glass, and be at least weakly buffered to resist pH drift.

An alternative way for ameliorating the electrolysis problem is to operating the electrokinetic pump in AC (alternating current) mode. AC mode pumping ensures slower pH evolution and bubble formation because the protons and oxygen generated at the anode, and hydroxyl ions and hydrogen generated at the cathode will react with the electrode when the direction of current is opposite. However, for general usage purposes, the AC output flow needs to be rectified into continuous net DC flow. A typical solution is utilizing a four-way bridge rectifier. Figure A.4 shows the schematic of the integrated electrokinetic pump and rectifier system. This bridge rectifier can be achieved by a valve array composed of four check valves. There are several candidates for this check-valve rectifier system, and one of them is the mobile polymer monolith valve³⁰. Such check-valves can be constructed with the aid of in-situ photo-polymerization inside a micro channel, through which the geometry of the polymer monolith can be made conformal to the shape of the micro channel. The photo polymerization process for this mobile polymer monolith is the same as that for the micro salt bridge, and greatly simplifies the fabrication process. This approach is likely to solve the pH evolution problem, but is unlikely to solve the

³⁰ E. F. Hasselbrink, T. J. Shepodd, J. E. Rehm, *Anal. Chem.* Vol. 74 (2002) 4913

bubble generation problem completely. Thus employing this approach with gasless electrodes would probably be the most ideal (and technologically most challenging) solution.

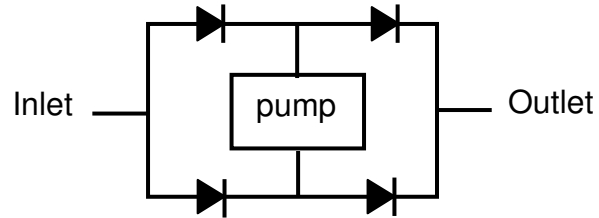


Figure A.4: Schematic of integration of an AC electrokinetic pump and a bridge rectifier check-valve system: The AC flow output from the electrokinetic pump is rectified into net DC flow by the check-valve system.

A.4 Meso-scale Electrokinetic Pumps

A meso-scale electrokinetic pump was developed and constructed for demonstrating the working principle of electrokinetic pumping prior to realizing it at the micro scale. This device found immediate applications as an actuator and pump for biomedical devices. The meso-scale electrokinetic pump is shown in figure A.5.

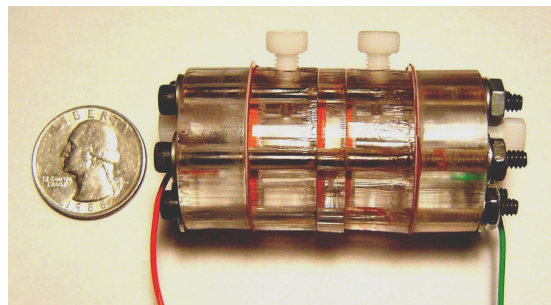


Figure A.5: A meso-scale electrokinetic pump constructed in a PMMA casing.

A.4.1 Design

The goal in designing this electrokinetic pump was to demonstrate the principle of electrokinetic pumping and characterize the relations between electroosmotic pressure, flow rate and applied electric field. For the purpose of functioning as an actuator, the requirements were set to a maximum pressure (P) of 60 psi and a volume flow rate (Q) of 1 $\mu\text{L}/\text{sec}$. The maximum allowable energy consumption was set to 1 mW while the applied voltage was set between 10 - 30 volts; the corresponding current was expected on the order of mA.

From Equations (A.14) and (A.15), it is known that the ratio of pressure/voltage significantly depends on the pore size, and this relation is shown in Figure A.6 (a). As can be seen, the pressure/voltage ratio ranges from 4 to 10 psi/volt when the pore size is varied from 250 to 160 nm, which offers a range of candidate materials to meet our requirement of pumping against 60 psi counter pressure for < 30 volts. The corresponding flow rate can be obtained by Equation (A.10). Figure A.6 (b) shows that the velocity of electroosmotic flow is from 50 to 350 $\mu\text{m}/\text{sec}$ when a range of 10 to 60 volts/cm is applied; hence for a 1 cm^2 cross-sectional area, the flow rate is from 5 to 35 $\mu\text{L}/\text{sec}$. Note that the relative permittivity is 78, and the zeta potential is -80 mV for this calculation.

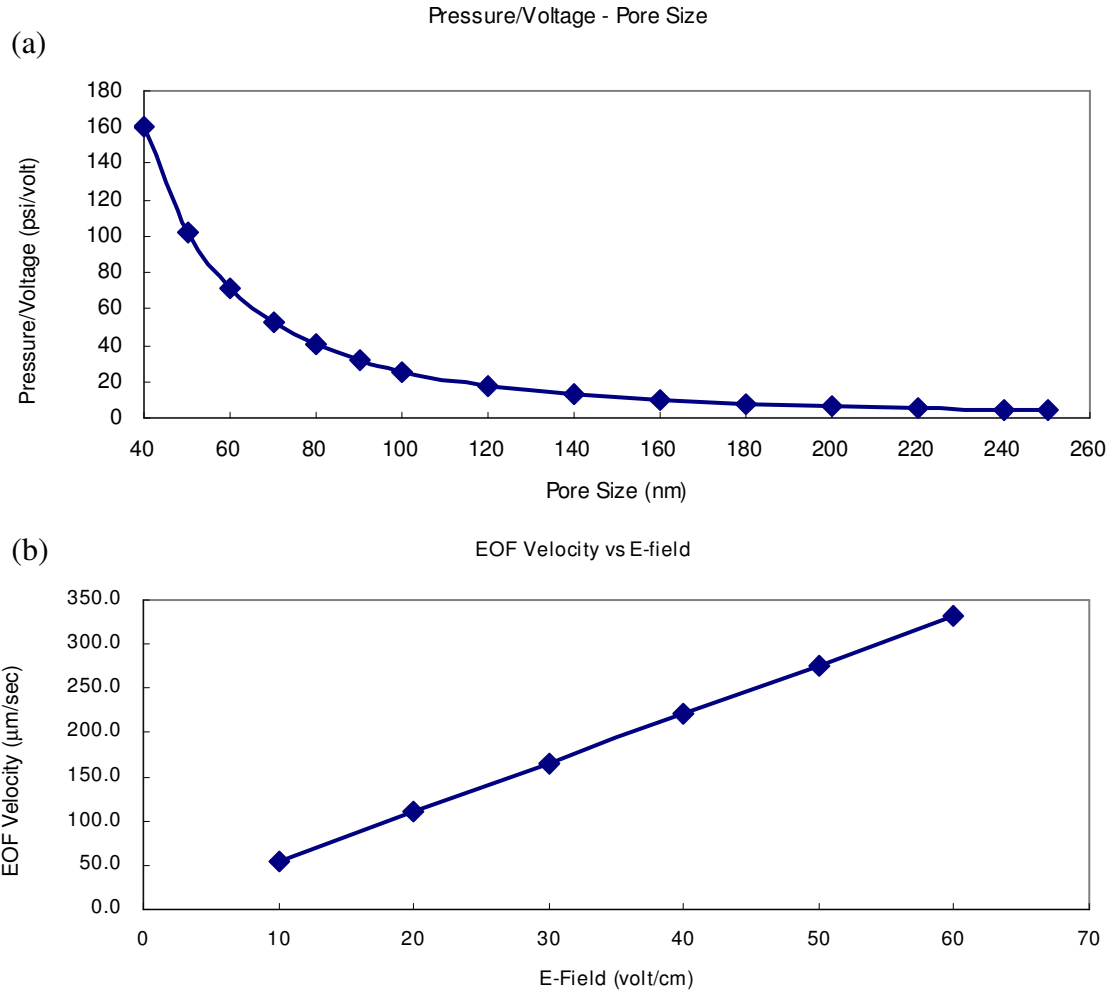


Figure A.6: (a) Ratio of pressure and voltage vs. pore size. The ratio is proportional to the inverse of square of the pore size. (b) EOF velocity vs. electrical field.

A.4.2 Composition and Fabrication

The meso-scale electrokinetic pump is composed of three parts: porous frit, an electrode, and an ion exchange membrane. All these parts are encased in a PMMA housing. Figure A.7 shows the PMMA casing and the porous frit.

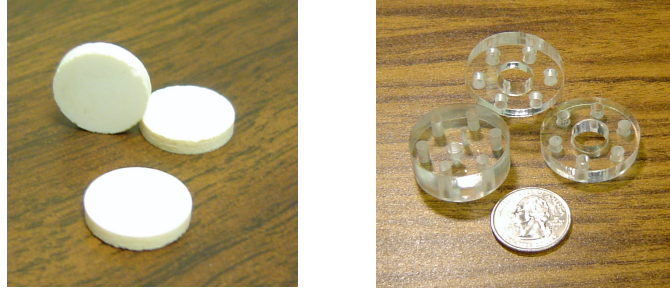


Figure A.7: LEFT: The porous frit “Porous Vycor.” The average pore size is 200 nm. RIGHT: PMMA machined by a laser cutter serves as the casings of the meso-scale electrokinetic pump.

1. Porous material: This porous material is where electroosmotic flow is generated. A circular porous frit (“Porous Vycor”, Advanced Glass & Ceramics, MA) is employed for the current electrokinetic pump. This porous frit is composed of 99.99% silica, with 1 mm thickness and 1 cm diameter. The average pore size is 200 nm and the porosity is 26% (porosity: ratio of void to overall cross-sectional area). The porous material can also be formed in micro channels by packed beads or porous polymer instead.
2. Electrodes: The electrode needs to be chemically inert so that it will not directly react with the electrolyte easily. Noble metals such as platinum or palladium are appropriate for this purpose. Palladium is especially good for the cathode due to its ability to absorb hydrogen.
3. Ion exchange membrane: The ion exchange membrane is placed between the electrode chamber and the porous frit to keep bubbles from entering the pump body while still allowing electric current to pass.

The shape and pattern of the PMMA casing was designed with the aid of CAD software. By using a computer controlled laser cutter the PMMA is easily machined. Figure A.8 shows a schematic of the composition of an electrokinetic pump.

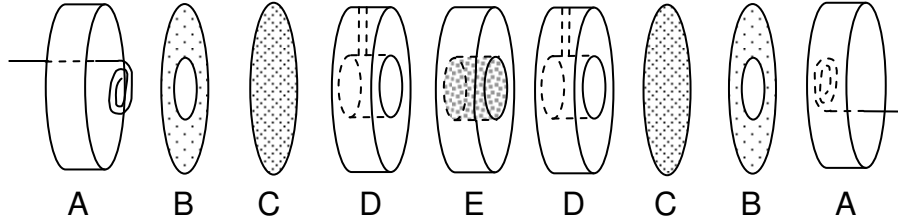


Figure A.8: Composition of a meso-scale electrokinetic pump: A) electrodes; B) spacer; C) ion exchange membrane; D) pump inlet and outlet; E) porous frit. Part A, D, E is constructed in PMMA casings.

A.4.3 Experiment Results and Discussion

The characterization of electrokinetic pumps included flow rate measurement and pressure measurements. The experimental apparatus for EK pump characterization is shown in figure A.9. Before actual measurement, the pump needed to be filled and flushed by filtered DI water using a syringe pump, and all gas bubbles had to be completely driven out of the pump during this process. Two pressure transducers (Honeywell 40PC series) were installed right before and after the electrokinetic pump for pressure measurement, and were controlled by a 12 bit DAQPad 6020E I/O board (National Instruments). The flow rate was obtained by measuring the weight difference from the scale (Mettler Toledo, precision 0.1mg) with a known time interval. Compressed nitrogen served as the pressure source for the counter pressure.

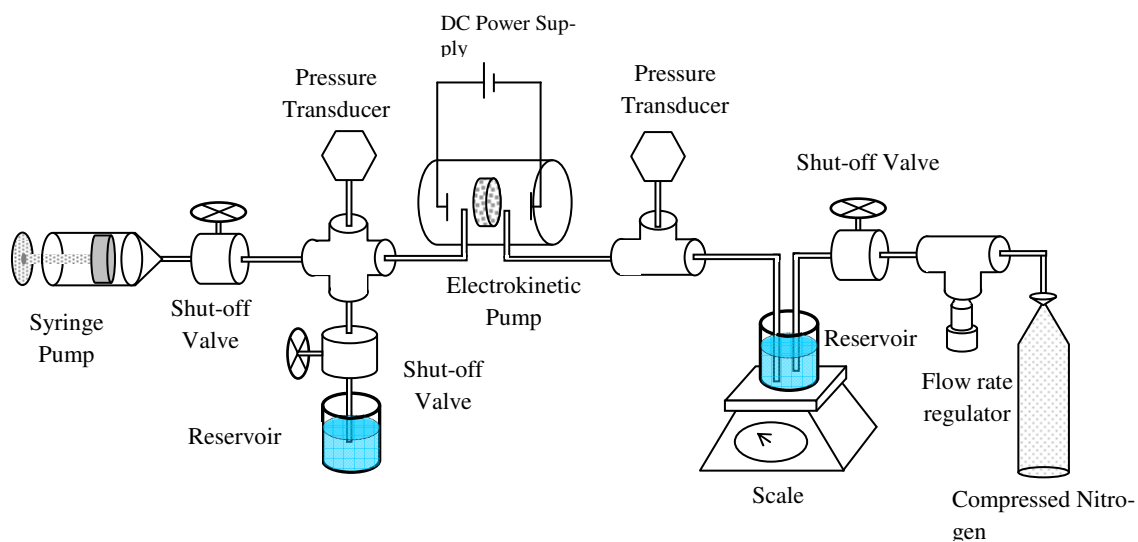


Figure A.9: Experiment apparatus for characterization of the electrokinetic pump. The electrokinetic pump was connected to a DC power supply. The fluidic inlet was connected to a cross which linked the pressure transducer, reservoir and syringe pump. During flushing the reservoir shut valve was off so the liquid passed through the pump body. The outlet was connected to a pressure transducer and a reservoir that was placed on a scale for measuring the flow rate. The counter pressure could be adjusted by the regulator for pressure-flow rate measurement.

The theoretical estimation and experiment results of relations between the counter pressure and the flow rate are shown in Figure A.10. It is found that under an E-field of 3.33 volt/cm, the flow rate of the free flow mode (no counter pressure) was 10 nL/sec, and linearly decreased when the counter pressure increased. The max pressure attained by this pump was 30psi, and was linear with applied voltage with a slope of about 3 psi/volt.

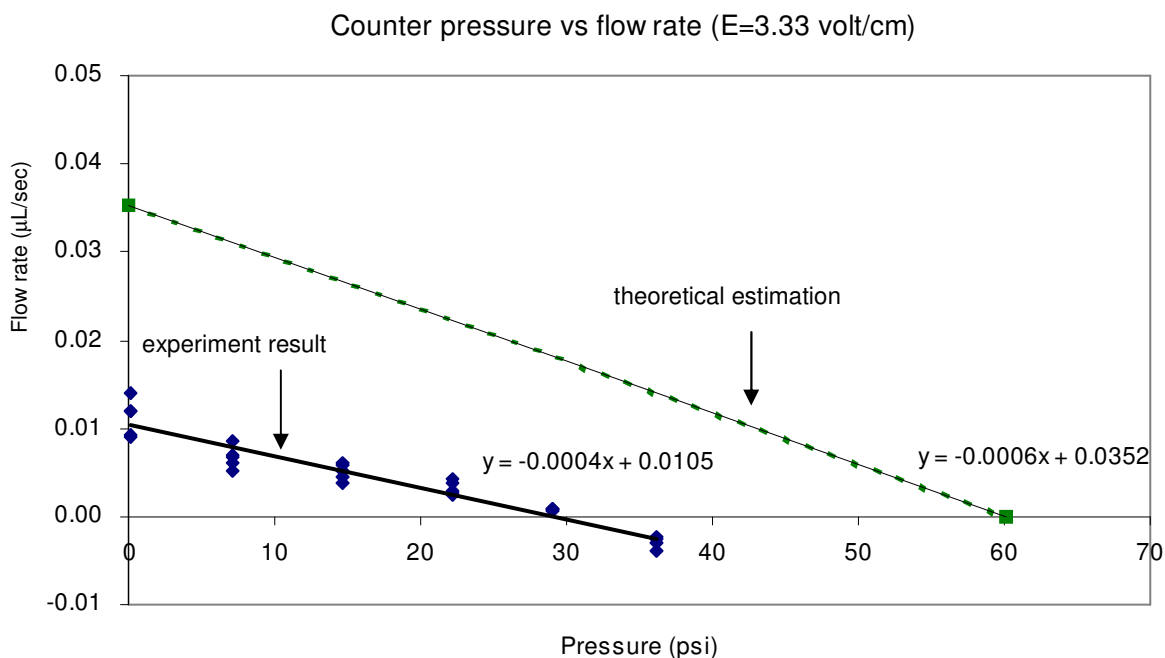


Figure A.10: The relationship of counter pressure and the E-field. In free flow mode (no counter pressure) the EOF flow rate is about 10 nL/sec. The flow rate linearly decreased when the counter pressure increased and no liquid is detected when counter pressure is 30 psi. The electric field is 3.33 volt/cm and the spacing of the electrodes is 3 cm. The ratio of pressure to the voltage is 3 psi/volt. The experiment result of EOF flow rate is smaller than theoretical estimation by 2 to 3 times.

It is noted that the flow rate is smaller than the theoretical estimation. The reasons for the flow rate deduction might be from:

1. Formation factors of the porous frit: The arbitrariness of nano channels in the sintered porous frit increases the hydraulic resistance and hence reduces the EOF flow rate.
2. Possible potential drops of the ion exchange membrane: Voltage drops when the

current pass through the ion exchange membrane, which leads to a deduction of E-field across the porous frit.

3. Polarization of electrodes: When current transmits through electrodes to electrolyte, the relation of voltage and current is not simply linear like an ohmic impedance. The voltage must exceed a certain quantity to make the current detectable. This voltage value is termed overpotential and the phenomenon is called polarization of electrodes³¹. This effect is more significant the current becomes larger. Polarization of electrodes lowers the effect of electrical field through the electrokinetic pump.

A.5 A Micro scale Electrokinetic Pump

One advantage of electrokinetic pumping is the scalability into the micro scale. Here we present a micro fabricated electrokinetic pump and proposed a research for applications in drug delivery systems.

A.5.1 Design

A schematic of the micro scale electrokinetic pump is shown in Figure A.11. The substrate was borosilicate glass. The dimension of the inlet and outlet micro channels was: 2.0 cm in width, 0.45 cm in length, and 35 μm in depth. The depth of the nano channel was 200 nm, the length is 1 mm and the width was the same as the inlet/outlet channels. The width of the observing zone was 500 μm and also 35 μm deep. This micro scale elec-

³¹ H. B. Oldham, and J. C. Myland, *Fundamentals of Electrochemical Science* (1994), Academic Press

trokinetic pump was designed for a flow rate of 10 nL/min. For such a low flow rate the weighing method used for measuring the flow rate of meso-scale EK pump was no longer appropriate. Hence, a new detection method, bleached dye imaging for flow rate measurement, was employed here. Since most bleachable fluorescent dye is not zwitterionic (neutral or zero net charge), an observation zone on the micro electrokinetic pump needed to be arranged away from the electric field for measurement of pure EOF velocity during the design stage.

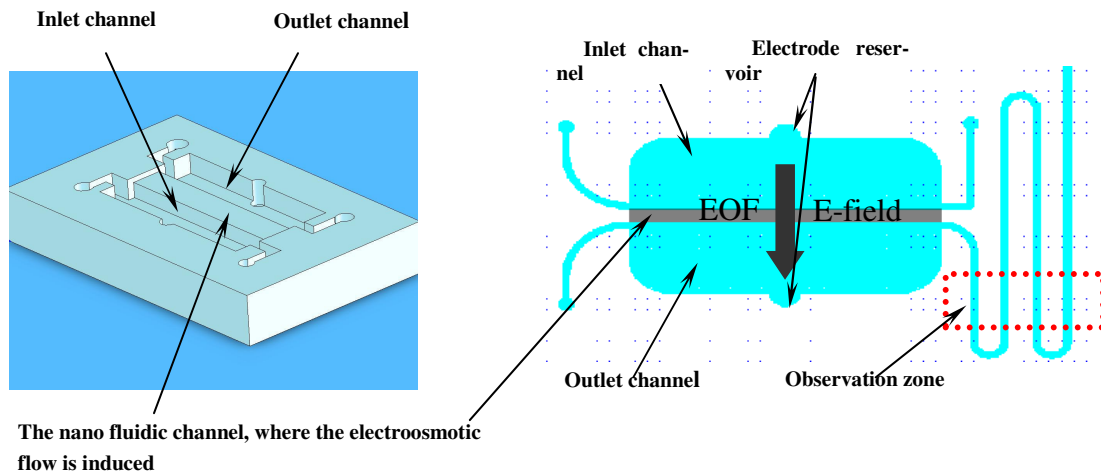


Figure A.11: The schematic of micro-scale electrokinetic pumps. LEFT: A 3-D view of the unpackaged electrokinetic pump. RIGHT: The top view of the electrokinetic pump. The electrodes were placed on the sides of the micro channels, and the electrical field acted across the nano channel. The observation zone was located away from the pump body to reduce the effect from the electrical field.

A.5.2 Fabrication

Standard MEMS process was used to manufacture the electrokinetic pumps. The process used two masks. Borosilicate glass substrates (4 inch diameter, 1 mm thickness, S.

I. Howard Glass, MA) were used for this application because glass transparency allows for subsequent microscopy observation. All the micro fabrication was processed in the Lurie Nanofabrication Facility (LNF) at the University of Michigan.

Figure A.12 shows the fabrication process flow. The glass substrates were first piranha cleaned for 15 minutes, rinsed with DI water and then dried in a spin rinse dryer (Semitool). Since the nano and micro channels were machined by wet etching (dilute BHF and dilute HF, respectively), a metal layer (Chrome, thickness 3000Å) was deposited on the glass substrate to serve as a protective layer. Details of parameters for subsequent lithography and wet-etching process are listed in Table A.1.

Table A.1
Parameters of Wet-Etching for Micro and Nano Channels

	NANO CHANNELS	MICRO CHANNELS
Dehydration bake temp/time	5 min/115° C	5min/115° C
PR/spin rpm/time	S1813/4000rpm/30sec	AZ9260/4000rpm/30sec
Softbake temperature/time	115° C/70sec	110° C/3min
UV Exposure	6.5 sec	50sec
Developer/time	MF-319/66sec	AZ-400K/150sec
Hardbake temperature/time	N/A	115° C/3min 20sec
Etchant	BHF: DI = 1:1	HF: DI = 1:9
Etch rate	~120 nm/min	~1 μm/min
Default etching depth	200 nm	35 μm

Holes connecting to the micro channels were drilled prior to bonding. There are different ways for drilling holes on a glass substrate. Traditional drill press is handy and fast for drilling holes, but the glass substrate is so brittle that it breaks easily if the substrate is too thin (less than 0.7 mm). One way to solve this problem is to drill several times: start with the smallest drill (less than 0.5 mm diameter) first. Since the drill bit is very small, the energy transferred from the drill bit will not be strong enough to cause the substrate to

crack. After the first small hole is drilled, it can be expanded by a larger drill bit and finally to the required size.

An alternative way for drilling holes on a glass substrate is electrochemical drilling. The glass substrate was immersed horizontally in a 49% sodium hydroxide (NaOH) solution. A stainless iron needle was attached to the cathode connected to a power supply, and the tip of the needle was aligned right on top of the location where to be drilled (the tip has to be in contact with the substrate surface). The anode coming out of the power supply was immersed in the NaOH solution. When turning on the power supply, some sparkles could be observed between the needle tip and the substrate, and the glass should be drilled through within one minute. Although this drilling method is effective and easy, after drilling several holes the NaOH solution became extremely dirty due to lots of debris and chemical products floating on the NaOH solution so that alignment of the tip was especially difficult. In addition, corrosiveness of NaOH increased manipulation difficulties.

After drilling holes the patterned glass substrate was ready to bond with another unprocessed wafer. Before the actual bonding process, the glass substrates needed to be cleaned in piranha solution again for removal particles on the substrate surface. The glass substrates were then hydrolyzed in a 49% KOH at 85°C for 15 minutes. After rinsing and drying, the glass substrates could be pre-bonded by exerting a uniform pressure on the substrate and stuck to each other without difficulty. This pre-bonded glass wafer was then annealed in an oven at 550°C for 5 hours. A fabricated device is shown in Figure A.13. Detailed Process flow is in Appendix C.

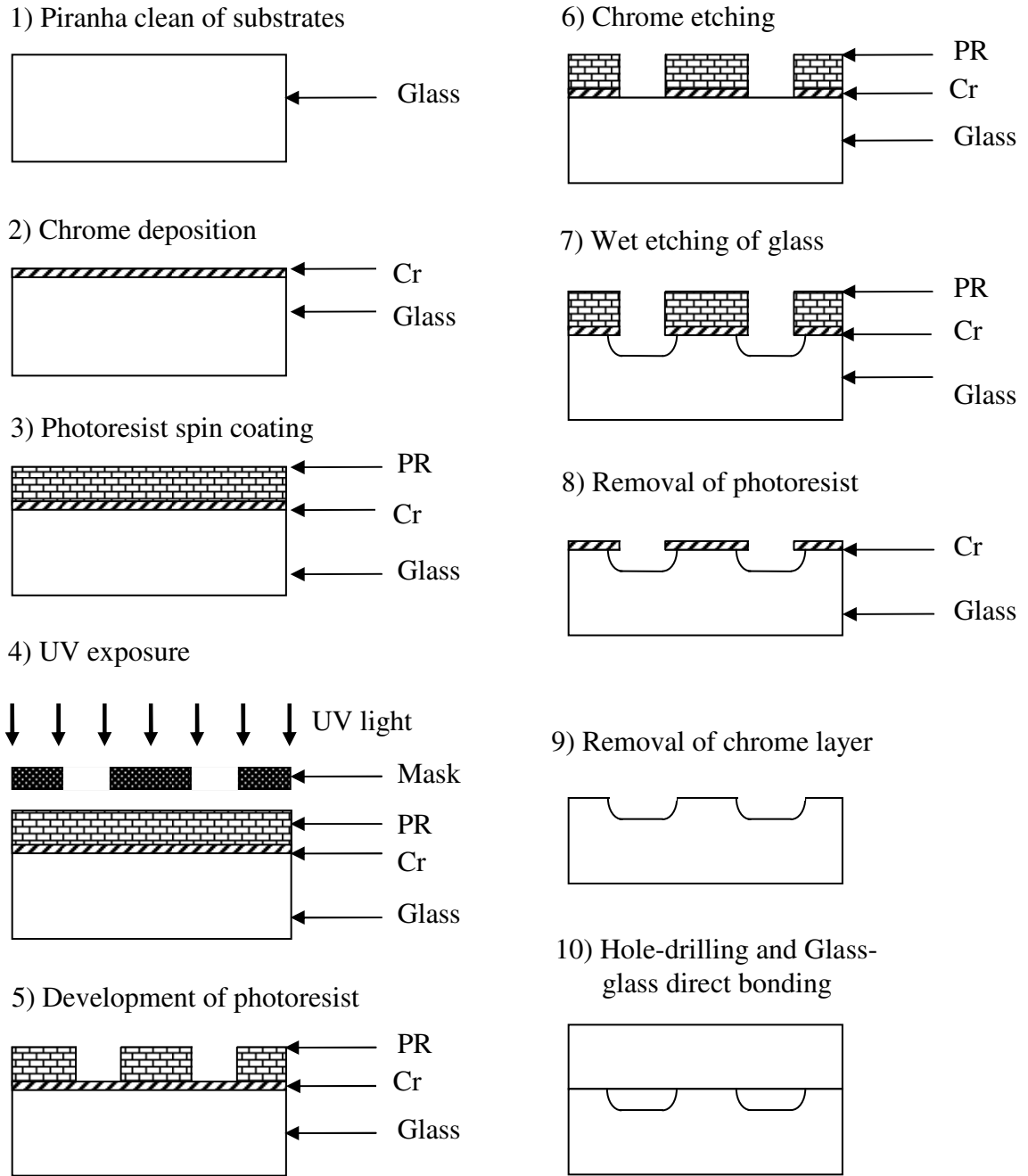


Figure A.12: Process flow of fabrication procedure for the electrokinetic pumps. Shallow etching (micro channels) was processed prior to deep etching for better photoresist coating. (Procedure 3 to 8 repeated for fabrication of deeper channels.) Holes needed to be drilled before glass-glass direct bonding.

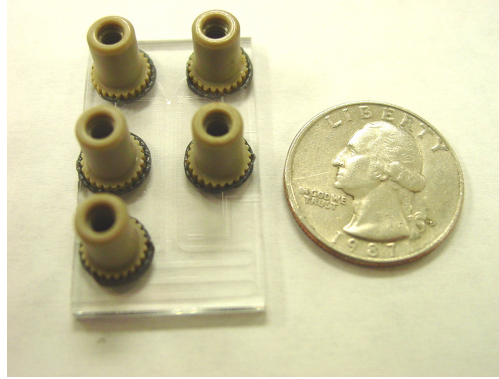


Figure A.13: A micro-scale electrokinetic pump.

A.5.3 Experiment Results and Discussion

As described in the previous section, the precision and detection limit of the scale is 0.1 mg which is very close to the expected flow rate of micro scale electrokinetic pump. Hence the experimental apparatus needed to be modified from that for the meso-scale electrokinetic pump. The new flow rate measurement method employed for the micro-scale electrokinetic pump was bleached-dye imaging.

A.5.3.1 Bleached-dye Imaging Flow rate Measurement

Fluorescence microscopy is an important detection technique for biology applications. Among different fluorescence imaging techniques caged-dye and bleached-dye imaging methods are most applicable for flow visualization^{32,33}. Figure A.14 shows the principle of these two imaging methods. An optical-contrast region is constructed on the microfluidic chip by exposing the region of interest to a laser or a focused light. Informa-

³² E. F. Hasselbrink, and S. Madhavan-Reese, internal report (not published)

³³ B. P. Mosier, J. I. Molho, and J. G. Santiago, Experiments in Fluids Vol. 33 (2002) 545

tion is hence revealed by comparing this optical-contrast region to other region (not exposed to the laser). For caged-dye imaging, the dye is initially non-fluorescent until being photo-activated by UV light. In the case of bleached-dye imaging, the dye is initially fluorescent and after selectively exposed to a focused light the dye in this exposed region is bleached and hence provides a contrast zone. The wavelength of the light for photo bleaching depends on the properties of the fluorescent dye.

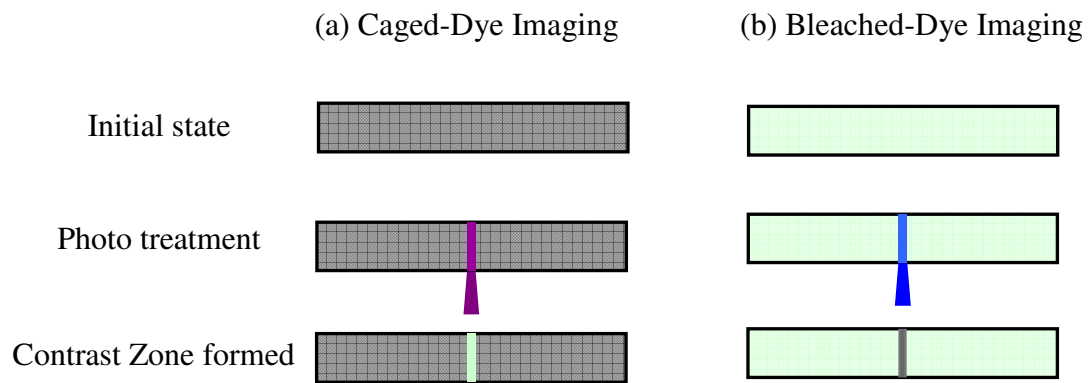


Figure A.14: Caged-dye and bleached-dye imaging method. (a) Caged-dye imaging. The fluorescent-dye becomes fluorescent after UV activation. (b) Bleached dye imaging. The fluorescent-dye is initially fluorescent and then become non-fluorescent after bleached by a focus light.

Figure A.15 shows the apparatus for the bleached dye imaging method. The fluorescent dye used here was fluorescein sodium salt for its easiness of photo bleaching. The 488 nm light from Ar-ion laser (Melles Griot) was guided toward and focused through a 4X objective (Olympus) onto the observation zone of the microfluidic chip located on the platform of an inverse fluorescent microscope (Olympus IX-51). In the observation zone, the fluorescent dye in the buffer solution was exposed to the 488nm light and bleached. It

became non-fluorescent and formed a dark region in the microfluidic channel. As a voltage was added across the micro electrokinetic pump, the flow started to move (electroosmosis) and so did this dark region. The displacement of this dark region was recorded by an 8-bit CCD camera (SONY XC-ST50). By controlling the frequency of the camera we could obtain the velocity of the EOF.

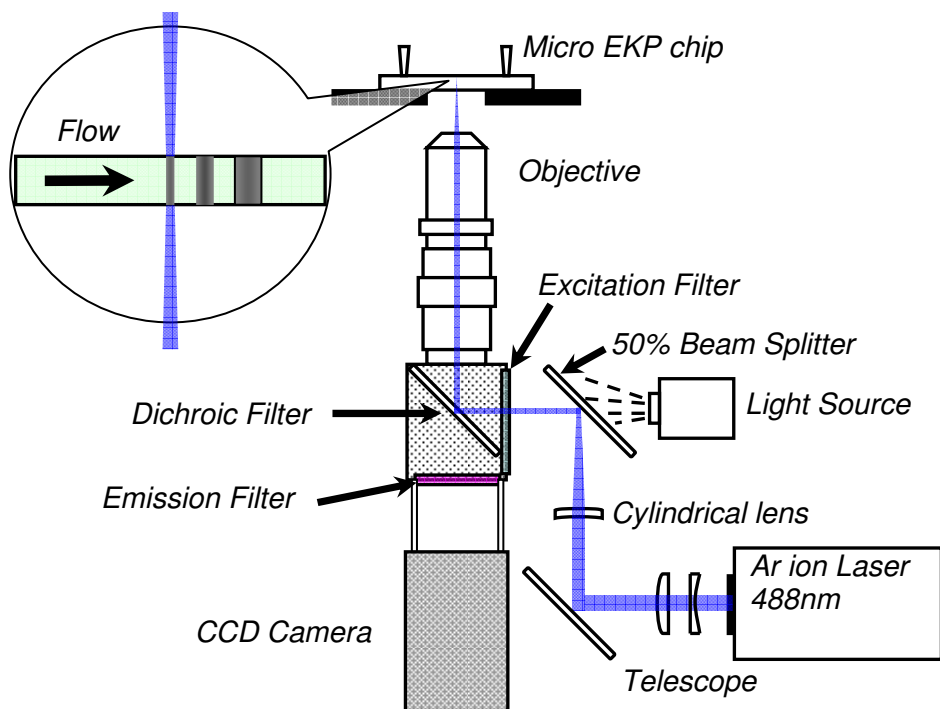


Figure A.15: Apparatus of bleached dye imaging method. Sodium fluorescein was used for the measurement. The light coming out of the Ar-ion laser was shaped into a thin rectangle after passing through the telescope and the cylindrical lens. The default frequency of the CCD camera was 30 Hz and was controlled by an image acquisition card (National Instrument).

A.5.3.2 Pump Performance

The velocity was obtained by measuring the displacement of the dark region within a

known time interval. The results showed that the flow rate of the micro scale EKP was about 2 nL/sec under free flow mode (no counter pressure) when supplied with 10 volts. The flow rate increased monotonically while the voltage increases. Figure A.16 shows a sequence of images of the EOF motion under various voltage applications. As can be seen the dark region kept still when the voltage is zero, which ensured no other driving force was in effect for the movement of the liquid. The measured EOF velocity and voltage, and the theoretical estimation (zeta potential = -80 mV) are presented in Figure A.17.

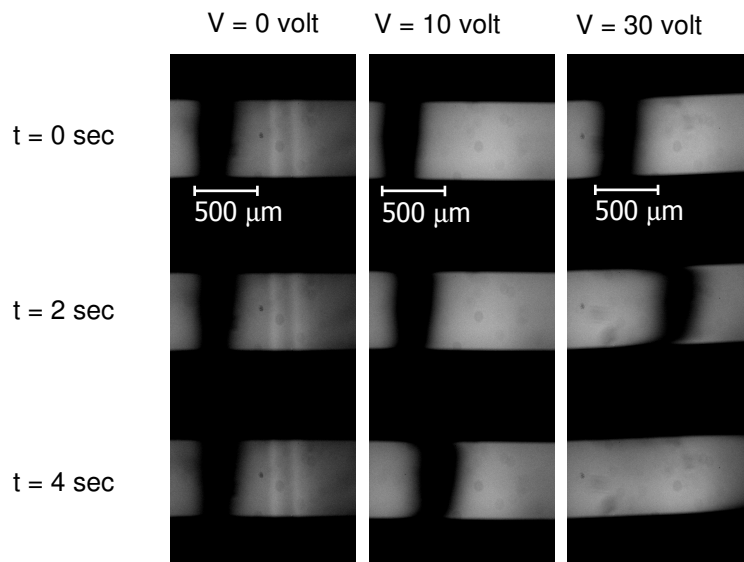


Figure A.16: Flow motion recorded by bleached-dye imaging method. The displacement of the dark region was almost non-detectable when there was no voltage applied. And velocity of this dark region was proportional to the voltage applied.

One major challenge of electrokinetic pumping is longevity. Current electrokinetic pumps suffer from stable long-term pumping due to electrolysis. Bubble generation causes an unstable and inconsistent flow rate output, while pH evolution directly affects

the zeta potential of the channel surface and hence degrade the performance; eventually the pumps stops when pH reaches about 3. Figure A.18 shows that the performance of a meso-scale electrokinetic pump degraded when pumping continuously more than 3 minutes. For solving all these problems improvement of electrodes is the first priority for advancing this pumping technique. Alternatively AC electrokinetic pumping is another solution as long as the AC flow can be rectified into net DC flow. In addition, using porous frit is an easy and accessible way for electrokinetic pumping, however the different formation factors of these frits cause inconsistent pumping performance. For more stable pumping the electrokinetic pumps has to be micro fabricated instead of direct porous frit installation.

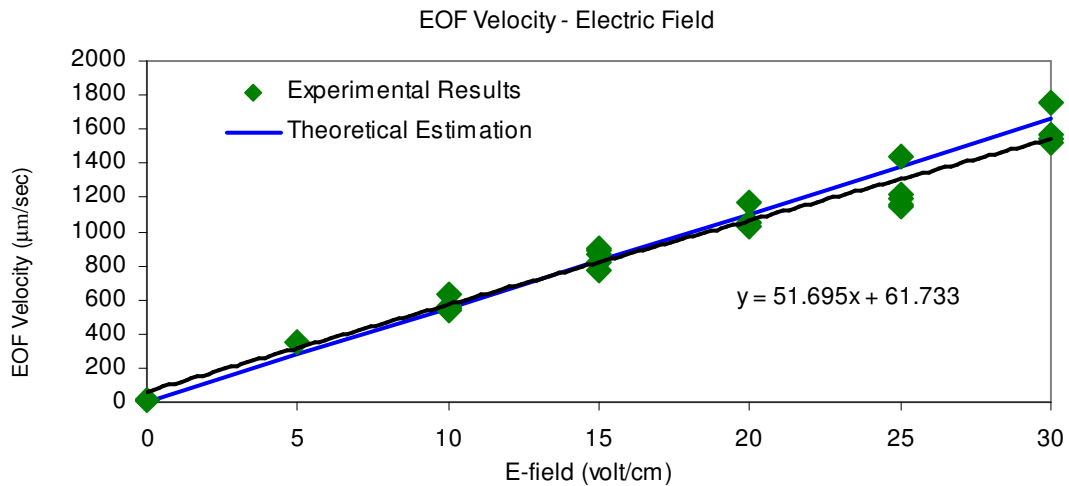


Figure A.17: Theoretical estimation and experimental result of EOF velocity vs. electrical field. The zeta potential used in theoretical calculation is 80 mV, viscosity is 0.001 Pa · s and relative permittivity is 78. The EOF velocity monotonically increased when the applied electrical field was increasing.

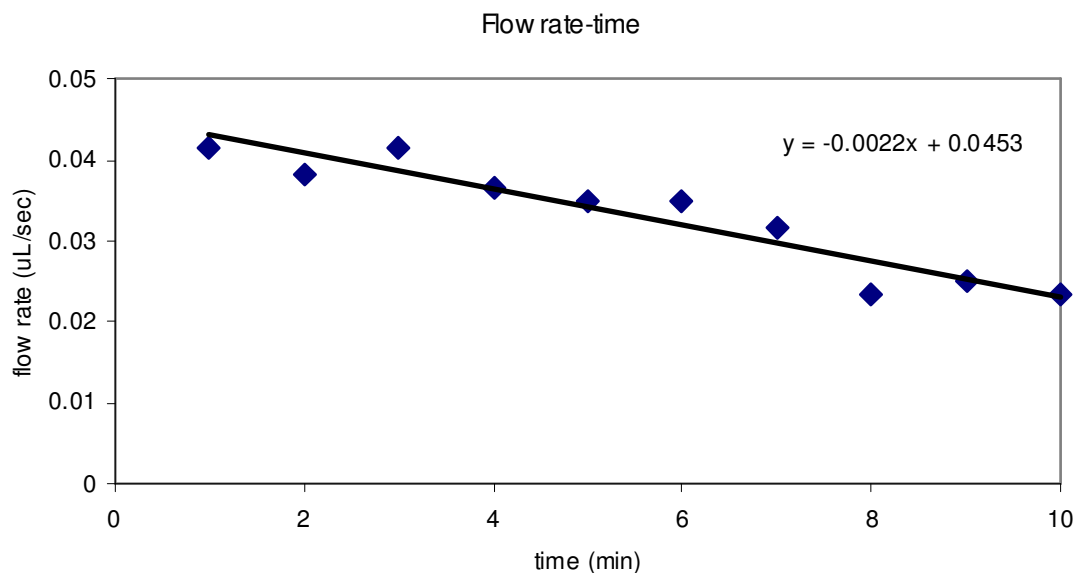


Figure A.18: EOF flow rate vs. time. The EOF flow rate decreased after pumping for about 3 minutes. The working liquid is 5 mM phosphate buffer. The E-field is 10 volt/cm.

Another possible improvement is the choice of bleachable fluorescent dye. Though fluorescein sodium is easier to bleach, it is negatively charged and thus affected by the electric field. This leads to unwanted electrophoresis of the fluorescent dye. The measured EOF velocity correlated with electrophoresis (movement of the ion) of the fluorescein sodium. Therefore searching for zwitterionic bleachable fluorescent dyes remains a challenge for more accurate EOF measurements. The adoption of caged-dye imaging is another way to avoid this problem, but caged-dyes are generally hard to access.

A.6 Mobile Polymer Monolith Valve

Various types of MEMS valves have been developed^{34,35,36} for different applications. However for integrating a micro check-valve with an electrokinetic pump, several factors need to be carefully considered. The fabrication of the candidate check-valve needs to be compatible with the process of the electrokinetic pump on a glass substrate. To reduce dead volume and unwanted hydraulic resistance, the microfluidic channels of the check-valve must remain in the plane of the pump, so that out-of-plane conduits are avoided. The check-valve also needs to resist high pressures (exceeding 200 psi) when closed due to the high pressure generated by the electrokinetic pump. For the above reasons, it is found out that check-valve composed of mobile polymer monolith²⁹ is an excellent match for integrating with an electrokinetic pump.

Figure A.19 shows the schematic³⁰ and actual MEMS device of the polymer monolith check-valves. As can be seen, the movement of the polymer plug is along the flow direction. When the flow direction is from left to right (configured as figure 3.1), the liquid flows through the bypass channel so the check valve is open. If the flow direction is opposite (from right to left), the polymer plug blocks the main channel so the valve is closed. Such micro check-valve is reported to be able to hold pressure as high as 4,500 psi²⁹ (30 MPA), which makes a perfect counterpart to the electrokinetic pump.

³⁴ X.-Q. Wang, Q. Lin, Y.-C. Tai, Proceedings, IEEE 12th International Micro Electro Mechanical Systems Conference (MEMS 99) 177

³⁵ A. P. Papavasiliou, D. Liepmann, and A. P. Pisano, Proc. of IMECE International Mechanical Engineering Congress and Exposition (1999), 1

³⁶ D. C. S. Bien, S. J. N. Mitchell, and H. S. Gamble, J. Micromech. Microeng. Vol. 13 (2003) 557

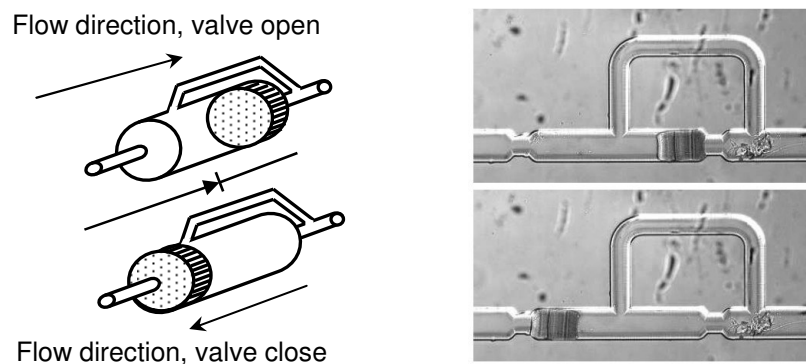


Figure A.19: LEFT: Schematic of the mobile monolith check-valve³⁰. The flow is only allowed to move one way. RIGHT: A micro-fabricated check-valve. The micro channel is machined by wet etching on a glass substrate. The polymer plug in the top figure is seated against the right end, and the liquid is able to flow through the bypass channel. The polymer plug in the bottom figure blocks the main channel, allowing no flow to pass through.

The polymer monolith is formed in-situ using UV laser (355nm) photopolymerization of a polymer solution in a specific region within the micro channel. The polymer solution consists of: monomer, crosslinker, solvent, photoinitiator, and inhibitor. The state of the polymer solution changes and begins to polymerize and cross-link when the initiator in the solution is exposed to the UV light. The inhibitor prevents the runaway polymerization by absorbing the photoinitiator. After polymerization unwanted solution is flushed away by the solvent. The material property (porosity, elastic modulus etc) of the polymer monolith is highly dependent on the ratio of these ingredients. Water may be added to the polymer solution to increase the pore size. When there is no water in the solution the pore size of the polymer monolith is generally on the order of nano meters, and the polymer becomes micro porous when water is added. Nano-porous polymer

monolith is generally stiffer than the micro-porous polymer, and can be used as a salt bridge.

In our work acrylate polymer is used for the purpose of the mobile plug of the micro check-valve. The recipe basically follows that developed in the Sandia National Laboratory²⁹, however slight changes in the composition ratio is made. The ingredients of the solution are shown in Table A.2. Detailed recipe of photo-polymerization is described in Appendix C.

Table A.2
Ingredients of Polymer Solution

INGREDIENTS	CHEMICAL NAME
Monomer	2,2,2-trifluoroethyl acrylate (TFEA)
Crosslinker	1,3-butanediol diacrylate (BDDA)
Solvent	2-methoxyethanol
Photoinitiator	2,2'-azobisisobutyronitrile (AIBN)
Inhibitor	4-methoxyphenol

The experimental apparatus for photo-polymerization is shown as figure A.20³⁷. The polymer solution is pre-loaded in the microfluidic chip. The trigger source of the polymerization is a 355 nm Nd-Yag laser operating at 10 Hz directed onto the microfluidic chip through a 4X objective (Olympus), and the area of the exposed region on the microfluidic chip is about 3 mm by 3 mm. An intensity sensor is attached to the end of the end of the optical loop for measurement of the power of the UV light. A CCD camera (SONY ST-

³⁷ A. Brask, M.-P. Chang, and E. F. Hasselbrink, "AC Electroosmotic Pump with Microvalves", internal report (not published)

XC50) is connected to the microscope (Olympus IX-51) for real time monitoring the polymerization process.

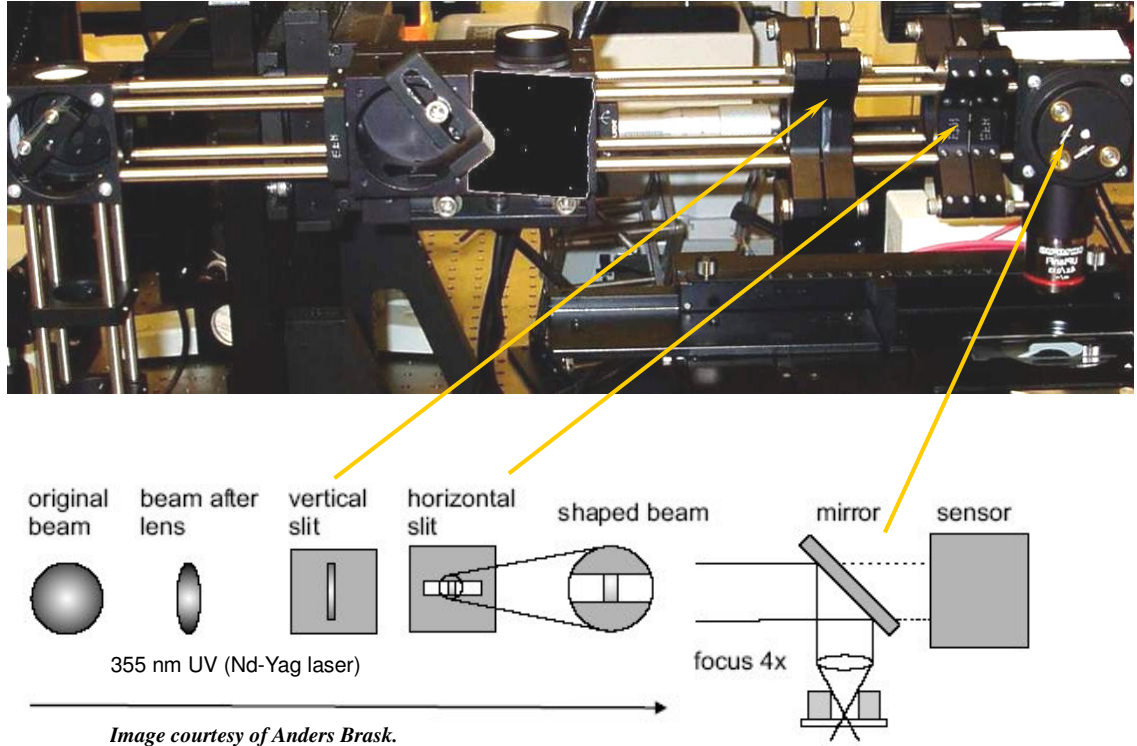


Figure A.20: Experiment apparatus of in-situ photo-polymerization. A 355 nm UV light is directed through a vertical and a horizontal slit, shaped into a rectangle and focused on a microfluidic chip seated on a microscope (Olympus IX-51).

Characterization of the micro check-valve includes (1) pressure to open the mobile polymer monolith: the polymer plug is not movable initially unless a certain open pressure is applied (2) diodicity: the ratio of hydraulic resistance of close to open mode and (3) pressure and flow rate in close and open modes. Hydraulic resistance can be obtained by measuring the pressure and flow rate of the pressure driven flow passing through the mi-

cro check-valve. The experiment apparatus for measuring the hydraulic resistance is in shown in Figure A.21.

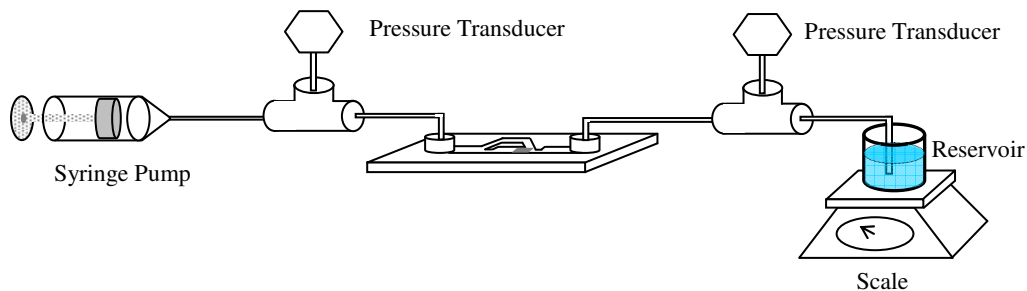


Figure A.21: Experiment apparatus of hydraulic resistance measurement. The syringe pump presses the liquid through the micro check-valve in both close and open mode. The pressure is recorded by the two pressure transducers and the flow rate is measured through a scale. The hydraulic resistance is the ratio of pressure and flow rate.

A.7 Micro fabricated Salt Bridges

As described in Section A.6, a nano-porous polymer monolith can be used as a micro- salt bridge. The nano-porous polymer allows ion to pass through but not bulk flow or bubbles. For effective ion transition, the electrical resistance needs to be low, while the hydraulic resistance needs to be high to block bulk flow. The salt bridge needs to be hydrophilic as well. A post array is fabricated onto the micro channels to support the micro salt bridge against the pressure generate by the electrokinetic pump. Figure A.22 shows the prototype of the micro salt bridge.

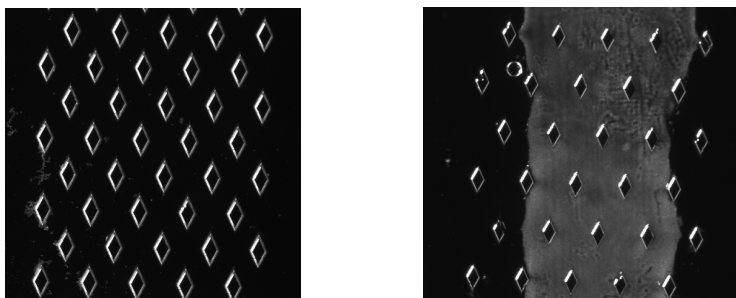


Figure A.22: Prototype of porous polymer monolith as a salt bridge. LEFT: a post array is placed in the micro channel to support the salt bridge against the high pressure. RIGHT: polymer monolith developed in the micro channel. The width of the polymer strip is 0.5 mm.

Fabrication procedure of the micro salt bridge is almost the same as that of the mobile polymer monolith, but the ingredients of the polymer solution is slightly different³⁸. The monomer used here is zwitterionic to ensure the polymer formed to be hydrophilic. The recipe basically follows [38].

In order to describe the performance of the micro salt bridge, characterization experiment will include (1) hydraulic resistance measurement (2) electrical resistance measurement and (3) ageing effect measurement. Procedure of hydraulic resistance measurement is the same as measuring the hydraulic resistance of a micro check-valve. Electrical resistance is obtained by measuring the voltage drop and the current across the salt bridge. For long-term electrokinetic pumping, the performance is dependent on the history of the micro salt bridge so influence by ageing (variation of hydraulic and electrical resistance with respect to time) needs to be investigated.

³⁸ S. Song, T. J. Shepodd, A. K. Singh, B. J. Kirby, Proc. Micro-TAS (2003) 421

A.8 Conclusion

The work has demonstrated successful electrokinetic pumping realized in various configurations. Meso and micro scale electrokinetic pumps have been constructed and characterized for proving the principle of electrokinetic pumping.

APPENDIX B

PULL-IN VOLTAGE WITH WATER DIELECTRIC

This appendix introduces the derivation of the pull-in voltage with water (or any liquid dielectric) and oxide (or any other dielectric) as dielectric. Consider a capacitor plate system as shown in Figure B.1. The top plate is mobile, holding by a spring with spring constant k . The bottom plate is fixed, insulated by a layer of oxide with thickness t_{ox} and separate with the top plate by an initial gap distance g (water thickness). ϵ_{ox} is the relative permittivity of the solid insulating layer, ϵ_L is the relative permittivity of the water between the plates, A is the area of overlap between the two capacitive plates, and ϵ_0 is the absolute permittivity. When the two plates is supplied by a bias V , the mobile has a displacement x , and hence the electrostatic force F_{elec} is expressed as

$$F_{elec} = \frac{-\epsilon_0 AV^2}{2 \left(\frac{t_{ox}}{\epsilon_{ox}} + \frac{g-x}{\epsilon_{rL}} \right)} \quad (B.1)$$

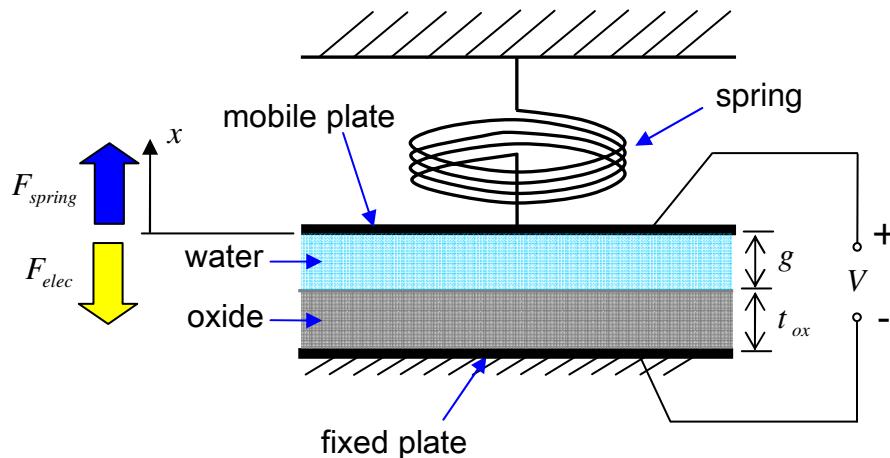


Figure B.1: Perspective-view schematic of a plate-spring system for electrostatic pull-in. The top mobile plate is held by a spring while the bottom plate is fixed.

And the spring force F_{spring} on the top capacitor plate is

$$F_{spring} = k \cdot x \quad (\text{B.2})$$

The electrostatic force and spring force are equal and opposite, so the force equilibrium equation can be written as

$$F_{elec} + F_{spring} = 0; \frac{-\epsilon_0 AV^2}{2 \left(\frac{t_{ox}}{\epsilon_{ox}} + \frac{g-x}{\epsilon_{rL}} \right)} + kx = 0 \quad (\text{B.3})$$

Solve Equation (B.3) for voltage V , and yield

$$V = \sqrt{\frac{2kx}{\epsilon_{rL}\epsilon_0 A} \left[(g-x) - \frac{t_{ox}\epsilon_{rL}}{\epsilon_{ox}} \right]} \quad (\text{B.4})$$

To find the pull-in voltage, we need to find the location of extremum of (B.4) by differentiating it with respect to x

$$\frac{\partial V}{\partial x} = 0 \quad (\text{B.5})$$

Solve (B.5) and yield

$$x = \frac{1}{3} \left(g + \frac{t_{ox}\epsilon_{rL}}{\epsilon_{ox}} \right) \quad (\text{B.6})$$

Substitute (B.6) into (B.4), and the pull-in voltage V_{PI} can be then presented as

$$V_{PI} = \sqrt{\frac{8k \left(g + t_{ox}\epsilon_{rL}/\epsilon_{ox} \right)}{27\epsilon_0\epsilon_{rL}A}} \quad (\text{B.7})$$

APPENDIX C

FABRICATION FLOW AND EXPERIMENTAL PROTOCOL

C.1 Fabrication Process Flow of PDMS Micro Actuators

This is the fabrication flow for electrostatically-actuated PDMS micro actuators presented in Chapters 2, 3, and 4.

1. Starting Wafers Preparation

Borosilicate Glass Wafers, 0.5-mm Thickness, 100-mm Diameter
Scribe wafer numbers on process and control wafers
Piranha Clean ($\text{H}_2\text{O}_2 : \text{H}_2\text{SO}_4 = 1 : 1$), 15 min

2. Pattern Alignment Mark (*Mask 1: ALGN, Dark Field*)

2.1. Spin Adhesion Promoter HMDS

Equipment: Solitec Spinner
Spin Time: 15 sec @ 4000 rpm

2.2. Spin Photoresist 1827, ~ 3 μm

Equipment: Solitec Spinner
Spin Time: 5 sec @ 500 rpm; 30 sec @ 4000 rpm
Softbake Time: 1 min 15 sec @ 110°C, Hotplate

2.3. Expose

Aligner: MA6, Contact Aligner
Contact Mode: Hard
Power : 20 mW
Exposure Time: 11 sec

2.4. Develop

Developer: MF319
Develop Time: 1 min 10 sec

2.5. DI Water Rinse

Rinse Time: 2 min

Spin Rinse Dry

2.6. Descum

Equipment: March Asher

O₂ Flow: 17 sccm

Pressure: 250 mTorr

Power: 100 W

Time: 100 sec

2.7. Ti-Pt Deposition

Equipment: Ener-Jet Evaporator

Thickness: Ti: 150 Å

Pt: 1000 Å

2.8. Ti-Pt Lift-Off

Acetone soaking, overnight

IPA soaking, 2 min

DI water rinse, 2 min

Spin Rinse Dry

3. Pattern ITO Electrodes (*Mask 2: ITO, Dark Field*)

3.1. Spin Adhesion Promoter HMDS

Equipment: Solitec Spinner

Spin Time: 15 sec @ 4000 rpm

3.2. Spin Photoresist 1827, ~ 3 μm

Equipment: Solitec Spinner

Spin Time: 5 sec @ 500 rpm; 30 sec @ 4000 rpm

Softbake Time: 1 min 15 sec @ 110°C, Hotplate

3.3. Expose

Aligner: MA6, Contact Aligner

Contact Mode: Hard

Power : 20 mW

Exposure Time: 11 sec

3.4. Develop

Developer: MF319

Develop Time: 1 min 10 sec

3.5. DI Water Rinse

Rinse Time: 2 min

Spin Rinse Dry

3.6. Descum

Equipment: March Asher

O₂ Flow: 17 sccm

Pressure: 250 mTorr

Power: 100 W

Time: 100 sec

3.7. ITO Deposition

Equipment: Ener-Jet Sputter

Thickness: 1500 Å

3.8. ITO Lift-Off

Hot PR remover 1112A soaking, 1 hour

DI water rinse, 2 min

Acetone soaking, 20 min

DI water rinse, 2 min

Spin Rinse Dry

3.9. Rapid Thermo Anneal

Equipment: Jet-first 150 RTP

Recipe: Bansal_ITO

Temperature: 750 °C

Time: 2 min

4. Pattern Oxide Isolation Layers (*Mask 3: OXETCH*, Dark Field)

4.1. High Temperature PECVD Oxide, 4500 Å

Equipment: GSI PECVD

Recipe: Oxide_Carrier
Temperature: 750 °C

4.2. Rapid Thermo Anneal

Equipment: Jet-first 150 RTP
Recipe: Bansal_Oxide
Temperature: 650 °C
Time: 2 min

4.3. Spin Adhesion Promoter HMDS

Equipment: Solitec Spinner
Spin Time: 15 sec @ 4000 rpm

4.4. Spin Photoresist 1827, ~ 3 μm

Equipment: Solitec Spinner
Spin Time: 5 sec @ 500 rpm; 30 sec @ 4000 rpm
Softbake Time: 1 min 15 sec @ 110°C, Hotplate

4.5. Expose

Aligner: MA6, Contact Aligner
Contact Mode: Hard
Power : 20 mW
Exposure Time: 11 sec

4.6. Develop

Developer: MF319
Develop Time: 1 min 10 sec

4.7. DI Water Rinse

Rinse Time: 2 min
Spin Rinse Dry

4.8. Descum

Equipment: March Asher
O₂ Flow: 17 sccm
Pressure: 250 mTorr
Power: 100 W
Time: 100 sec

4.9. Oxide Wet Etch

Etchant: Buffered HF
Etch rate: ~ 3000 Å/min
DI Water Rinse, 2 min
Spin Rinse Dry
Check Contact Conductivity

5. Photoresist Mold for Micro Channel (*Mask 4: CHAN, Bright Field*): *This step includes procedures for (A) 1827, 5 μm and (B) 9260, 10 μm channel molds.*

5.1.A Spin Adhesion Promoter HMDS

Equipment: Solitec Spinner
Spin Time: 15 sec @ 4000 rpm

5.2.A Spin Photoresist 1827, ~ 5 μm

Equipment: Solitec Spinner
Spin Time: 5 sec @ 500 rpm; 30 sec @ 2000 rpm
Softbake Time: 1 min 15 sec @ 110°C, Hotplate

5.3.A Expose 1827

Aligner: MA6, Contact Aligner
Contact Mode: Hard
Power : 20 mW
Exposure Time: 21 sec

5.4.A Develop

Developer: MF319
Develop Time: 1 min 30 sec

5.5.A DI Water Rinse

Rinse Time: 2 min
Spin Rinse Dry

5.6.A Descum

Equipment: March Asher
O₂ Flow: 17 sccm
Pressure: 250 mTorr
Power: 100 W

Time: 100 sec

OR

5.1.B Spin Adhesion Promoter HMDS

Equipment: Solitec Spinner
Spin Time: 15 sec @ 4000 rpm

5.2.B Spin Photoresist 9260, ~ 10 μ m

Equipment: Solitec Spinner
Spin Time: 5 sec @ 500 rpm; 30 sec @ 2000 rpm
Softbake Time: 3min 20 sec @ 110°C, Hotplate

5.3.B Expose 9260

Aligner: MA6, Contact Aligner
Contact Mode: Hard
Power : 20 mW
Exposure Time: 55 sec

5.4.B Develop

Developer: AZ@400K : DI = 1 : 3
Develop Time: 2 min 30 sec

5.5.B DI Water Rinse

Rinse Time: 2 min
Spin Rinse Dry

5.6.B Descum

Equipment: March Asher
O₂ Flow: 17 sccm
Pressure: 250 mTorr
Power: 100 W
Time: 100 sec

6. Pattern Cr-Au Layer (*Mask 5: MEETCH*, Bright Field)

6.1. Cr/Au Deposition

Equipment: Ener-Jet Sputter

Thickness: Cr: 150 Å
Au: 5000 Å

6.2. Spin Adhesion Promoter HMDS

Equipment: Solitec Spinner
Spin Time: 15 sec @ 4000 rpm

6.3. Spin Photoresist 1813, ~ 1.5 μm

Equipment: Solitec Spinner
Spin Time: 5 sec @ 500 rpm; 30 sec @ 4000 rpm
Softbake Time: 1 min 10 sec @ 110°C, Hotplate

6.4. Expose

Aligner: MA6, Contact Aligner
Contact Mode: Hard
Power : 20 mW
Exposure Time: 6.5 sec

6.5. Develop

Developer: MF319
Develop Time: 1 min 6 sec

6.6. DI Water Rinse

Rinse Time: 2 min
Spin Rinse Dry

6.7. Descum

Equipment: March Asher
O₂ Flow: 17 sccm
Pressure: 250 mTorr
Power: 100 W
Time: 100 sec

6.8. Gold Etch

Etchant: Pre-mixed gold etchant
Etch Rate: > 3000 Å/min
DI Water Rinse: 2 min
Spin Rinse Dry

6.9. Expose

Aligner: MA6, Contact Aligner
Contact Mode: Hard
Exposure Type : Flood
Power : 20 mW
Exposure Time: 15 sec

6.10. Develop

Developer: MF319
Develop Time: 1 min 30 sec

6.11. DI Water Rinse

Rinse Time: 2 min
Spin Rinse Dry

7. Dice Wafer

7.1. Spin Adhesion Promoter HMDS

Equipment: Solitec Spinner
Spin Time: 15 sec @ 4000 rpm

7.2. Spin Photoresist 1813, ~ 1.5 μm

Equipment: Solitec Spinner
Spin Time: 5 sec @ 500 rpm; 30 sec @ 4000 rpm
Softbake Time: 1 min 10 sec @ 110°C, Hotplate

7.3. Dicing

Equipment: MA 1006 Dicing Saw
Blade: 777

7.4. Expose

Aligner: MA6, Contact Aligner
Contact Mode: Hard
Exposure Type : Flood
Power : 20 mW
Exposure Time: 15 sec

7.5. Develop

Developer: MF319
Develop Time: 1 min 30 sec

7.6. DI Water Rinse

Rinse Time: 2 min
Die Level Blow Dry

8. Cr Etching

8.1. Cr Etch

Etchant: Pre-mixed chrome etchant
Etch Time: 3 sec
DI Water Rinse: 2 min
Die Level Blow Dry

9. Deposit Photo-Patternable Spin-on PDMS: *This step includes both procedures for (A) WL-5351, 6.7 μm and (B) WL-5150, 16 μm PDMS films.*

9.1.A Descum

Equipment: March Asher
O₂ Flow: 17 sccm
Pressure: 250 mTorr
Power: 100 W
Time: 100 sec

9.2.A Deposit Photo-Patternable PDMS

Equipment: Solitec Spinner
Spin Time: 30 sec @ 5000 rpm

9.3.A Expose

Aligner: MA6, Contact Aligner
Contact Mode: Hard
Exposure Type : Flood
Power : 20 mW
Exposure Time: 92 sec

9.4.A Thermo Cure

Equipment: Nitrogen Oven
Temperature: 110 °C
Time: 30 min

OR

9.1.B Descum

Equipment: March Asher
O₂ Flow: 17 sccm
Pressure: 250 mTorr
Power: 100 W
Time: 100 sec

9.2.B Deposit Photo-Patternable PDMS

Equipment: Solitec Spinner
Spin Time: 30 sec @ 4000 rpm

9.3.B Expose

Aligner: MA6, Contact Aligner
Contact Mode: Hard
Exposure Type : Flood
Power : 20 mW
Exposure Time: 92 sec

9.4.B Thermo Cure

Equipment: Nitrogen Oven
Temperature: 65 °C
Time: 4 hours

10. Release Device

10.1. Acetone Soaking

Time: Overnight (at least more than 8 hours)

10.2. Methanol Soaking

Time: 2 hours

10.3. Supercritical CO₂ Dry

Equipment: Samdri 915B

10.4. Dehydrate Bake

Equipment: Hotplate

Temperature: 100°C

Time: 2 min

C.2 Fabrication Process Flow of Electrokinetic Pumps

This is the fabrication flow for electrokinetic micro pumps presented in Appendix A.

1. Starting Wafers Preparation

Wafer Supplier: S.I.Howard Glass (<http://www.howardglass.com>)

4" diameter, 0.4 mm thickness, 1 flat, borosilicate glass wafer

Scribe wafer numbers on process and control wafers

Piranha Clean ($\text{H}_2\text{O}_2 : \text{H}_2\text{SO}_4 = 1 : 1$), 15 min

2. Chrome Mask Deposition

2.1. Cr/Au Deposition

Equipment: Ener-Jet Sputter

Thickness: Cr: 3000 Å

3. Shallow Channel Etch

3.1. Spin Adhesion Promoter HMDS

Equipment: Solitec Spinner

Spin Time: 15 sec @ 4000 rpm

3.2. Spin Photoresist 1813, ~ 1.5 μm

Equipment: Solitec Spinner

Spin Time: 5 sec @ 500 rpm; 30 sec @ 4000 rpm

Softbake Time: 1 min 10 sec @ 110°C, Hotplate

3.3. Expose

Aligner: MA6, Contact Aligner
Contact Mode: Hard
Power : 20 mW
Exposure Time: 6.5 sec

3.4. Develop

Developer: MF319
Develop Time: 1 min 10 sec

3.5. DI Water Rinse

Rinse Time: 2 min
Spin Rinse Dry

3.6. Descum

Equipment: March Asher
O₂ Flow: 17 sccm
Pressure: 250 mTorr
Power: 100 W
Time: 100 sec

3.7. Cr Etch

Etchant: Pre-mixed chrome etchant
Etch Rate: ~ 1000 Å/min
DI Water Rinse: 2 min
Spin Rinse Dry
Eye Inspection

3.8. Glass Etch

Etchant: BHF : DI = 1 : 1
Etch Rate: ~ 100 Å/min
DI Water Rinse: 2 min
Spin Rinse Dry

3.9. Surface Profilometry

Equipment: Dektak 6M Surface Profilometer

4. Deep Channel Etch

4.1. Spin Adhesion Promoter HMDS

Equipment: Solitec Spinner
Spin Time: 15 sec @ 4000 rpm

4.2. Spin Photoresist 9260, ~ 6 μm

Equipment: Solitec Spinner
Spin Time: 5 sec @ 500 rpm; 30 sec @ 4000 rpm
Softbake Time: 3 min 20 sec @ 110°C, Hotplate

4.3. Expose

Aligner: MA6, Contact Aligner
Contact Mode: Hard
Power : 20 mW
Exposure Time: 40 sec

4.4. Develop

Developer: AZ@400K : DI = 1 : 3
Develop Time: 2 min 30 sec

4.5. DI Water Rinse

Rinse Time: 2 min
Spin Rinse Dry

4.6. Descum

Equipment: March Asher
O₂ Flow: 17 sccm
Pressure: 250 mTorr
Power: 100 W
Time: 100 sec

4.7. Cr Etch

Etchant: Pre-mixed chrome etchant
Etch Rate: ~ 1000 Å/min
DI Water Rinse: 2 min
Spin Rinse Dry
Eye Inspection

4.8. Glass Etch

Etchant: HF : HCl : DI = 1 : 1 : 9

Etch Rate: ~ 1 $\mu\text{m}/\text{min}$
Target Depth: 20 μm
DI Water Rinse: 2 min
Spin Rinse Dry

4.9. Surface Profilometry

Equipment: Dektak 6M Surface Profilometer

5. Bonding

5.1. Wafer Clean

Piranha Clean (H_2O_2 : H_2SO_4 = 1 : 1), 15 min

5.2. KOH (49%) Soaking

Temperature: 85°C
Time: 12 min
DI Water Rinse
Spin Rinse Dry

5.3. Pre-Bond

Align Wafers
Press with finger force

6. Thermo Cure

6.1. Anneal

Equipment: DS263 Oven
5°C ramp rate/minute to 120°C, dwell 30 minutes
5°C ramp rate/minute to 475°C, dwell 120 minutes
3°C ramp rate/minute to 550°C, dwell 300 minutes
5°C ramp rate/minute to 475°C, dwell 60 minutes
15°C ramp rate/minutes to 20°C, end program

C.3 Protocols of Laser Polymerization

This is the experiment procedure of laser polymerization in Appendix A.

Polymer Solution Preparation

- Chemicals listings
 1. BDDA (1,3 butanediol diacrylate): 250 μ L (cross linker/frozen)
 2. TFEA (2,2,2-trifluoroethyl acrylate): 350 μ L (monomer/frozen)
 3. 2-methoxyethanol: 400 μ L (solvent/solvent storage cabinet)
 4. AIBN (2,2'-azobisisobutyronitrile): 16 mg (initiator/refrigerated)
 5. 4-methoxyphenol: 8 mg (inhibitor (radical scavenger)/refrigerated)
- Double check the recipe intended to use (microvalve_polymers.xls)
- Making the solvent solution (2-methoxyethanol, AIBN, 4-methoxyphenol)
 1. Take the AIBN and 4-methoxyphenol (both are powder) out of the refrigerator.
 2. Put a paper weigh plate on the balance, add AIBN and 4-methoxyphenol to the amount wanted
 3. Use the pipette to add 2-methoxyethanol to the amount wanted, stir gently until AIBN and 4-methoxyphenol completely dissolved
 4. Store the solution in a vial, and label it
- Mix the labeled solvent with BDDA and TFEA to the desired amount and ratio.

Sample Preparation and Optical Setup

- Attach the nanoports onto the micro valve chip. Cure at 135 degree C.
- Place the monomer solution vial on a holder (to avoid spilling)
- Inject the chip with the monomer solution on one port. Observe to make sure the channels are filled with solutions. Start the timer when observing solution flowing through the channels. Fill the other three ports with solution and tighten the plug.
- Set up the optical path and attach the objective lens (4X) in the end with the adaptor. Be extremely careful when detaching and attaching the objective lens.
- Turn on the power of the microscope.
- Open IPLab® software:
 1. Select the camera first (Hamatsu).

2. “Acquire Image.” Select the “focus” configuration.
 3. Set the “Exposure time” around 50~100.
- Make sure the shutter of the Laser is closed. Start the Laser. Wait for about 1 minute to let the laser warmed up.
 - Define the position and size of the exposed region. Mark the region with a rectangular on the screen. Usually the exposed area is set 1.5 times larger the plug size we intended.
 - Once the position is defined, do not move or touch the optical path/lens or the defined region might be changed.
 - Measure the source intensity of the laser. From experience 0.8 mJ/pulse will be appropriate.
 - Use a sample chip for a test run. Record how long since the solution has been injected. Start the laser and another timer. Carefully observe if any thing formed in the exposed region and record the time when the polymer begins to form. Stop the laser around 1 minute. (Or, stop the laser when the plug growth rate decreases.)
 - Test the valve-open pressure. If fine, run the same polymerization process on a practical chip. Follow the layout protocol in case confused with the geometry. Repeat the same procedure for all four valves.
 - Measure the full and reduced source intensity (FS, RS), and the full end intensity (FE). The reduced end intensity will be: $RE=FE*RS/FS$.

BIBLIOGRAPHY

BIBLIOGRAPHY

- [1] A. Manz, D. J. Harrison, E. M. J. Verpoorte, J. C. Fettinger, A. Paulus, H. Ludi and H. M. Widmer, "Planar chips technology for miniaturization and integration of separation techniques into monitoring systems: capillary electrophoresis on a chip," *Journal of Chromatography A*, vol. 593, pp. 253-258, 1992.
- [2] V. Studer, G. Hang, A. Pandolfi, M. Ortiz, W. F. Anderson and S. R. Quake, "Scaling properties of a low-actuation pressure microfluidic valve," *Journal of Applied Physics*, vol. 95, pp. 393-398, 2004.
- [3] J. J. Loverich, I. Kanno and H. Kotera, "Concepts for a new class of all polymer micropumps," *Lab on a Chip*, vol. 6, pp. 1147-1154, 2006.
- [4] C. R. Tamanaha, L. J. Whitman and R. J. Colton, "Hybrid macro-micro fluidics system for a chip-based biosensor," *Journal of Micromechanics and Microengineering*, vol. 12, pp. 7-17, 2002.
- [5] M. A. Unger, H. P. Chou, T. Thorsen, A. Scherer and S. R. Quake, "Monolithic microfabricated valves and pumps by multilayer soft lithography," *Science*, vol. 288, pp. 113-116, 2000.
- [6] R. A. Mathies, E. T. Lagally, T. Kamei, W. H. Grover, C. N. Liu, J. R. Scherer and R. A. Street, "Capillary array electrophoresis bioprocessors," in *Proceedings of 2002 Solid-State Sensor, Actuator, and Microsystems Workshop (Hilton Head Island, SC)*, June 2-6, pp. 112-117, 2002.
- [7] W. H. Grover, A. M. Skelley, C. N. Liu, E. T. Lagally and R. A. Mathies, "Monolithic membrane valves and diaphragm pumps for practical large-scale integration into glass microfluidic devices," *Sensors Actuators B*, vol. 89, pp. 315-323, 2003.
- [8] S.-K. Fan, P. P. de Guzman and C. J. Kim, "EWOD driving of droplet on $N \times M$ grid using single-layer electrode patterns," in *Proceedings of 2002 Solid-State Sensor, Actuator, and Microsystems Workshop (Hilton Head Island, SC)*, June 2-6, pp. 134-137, 2002.
- [9] W. H. Grover, R. H. C. Ivester, E. C. Jensen and R. A. Mathies, "Development and multiplexed control of latching pneumatic valves using microfluidic logical structures," *Lab on a Chip*, vol. 6, pp. 623-631, 2006.
- [10] T. Thorsen, S. J. Maerkl and S. R. Quake, "Microfluidic Large Scale Integration," *Science*, vol. 298, pp. 580-582, 2002.
- [11] N. A. Cellar and R. T. Kennedy, "A capillary-PDMS hybrid chip for separations-based sensing of neurotransmitters *in vivo*," *Lab on a Chip*, vol. 6, pp. 1205-1212, 2006.

- [12] K. R. Zavadil, M. A. Rising, and P. C. Galambos, "Limits of electrochemical processes at Si electrodes used at high field for aqueous microfluidic MEMS applications," in *Proceedings of Electrochemical Society Microfabricated Systems and MEMS VI, Series PV2002-6*, Pennington, NJ, pp. 144-152, 2002.
- [13] J. W. Judy, "Microelectromechanical systems (MEMS): fabrication, design and applications," *Smart Matter Structure*, vol. 10, pp. 1115-1134, 2001.
- [14] T. L. Sounart, T. A. Michalske and K. R. Zavadil, "Frequency-Dependent Electrostatic Actuation in Microfluidic MEMS," *ASME/IEEE Journal of Microelectromechanical Systems*, vol. 14, pp. 125-133, 2005.
- [15] B. Legrand, A.-S. Rollier, D. Collard and L. Buchailot, "Suppression of the pull-in instability for parallel-plate electrostatic actuators operated in dielectric liquids," *Applied Physics Letters*, vol. 88, pp. 034105-1-034105-3, 2006.
- [16] W. C. Young, *Roark's Formulas for Stress and Strain*, McGraw-Hill International Edition, 1989.
- [17] T. Bansal, M.-P. Chang, M. M. Maharbiz, "'Wet' AC Actuated Microfluidic Micropore Array for Patterning Diffusible Gradients During Cell Culture," in *Proceedings of Tenth International Conference on Miniaturized Systems for Chemistry and Life Sciences (MicroTAS)*, Tokyo, Japan, November, pp. 1181-1183, 2006.
- [18] T. Bansal, J. K. Singhal and M. M. Maharbiz, unpublished manuscript.
- [19] H. A. Stone, A. D. Strook and A. Ajdari, "Engineering flows in small devices- microfluidics toward a lab-on-a-chip," *Annual Review of Fluid Mechanics*, vol. 36, pp. 381-411, 2004.
- [20] T. Bansal, M.-P. Chang and M. M. Maharbiz, "A class of low voltage, elastomer-metal 'wet' actuators for use in high-density microfluidics," *Lab on a Chip*, vol. 7, pp. 164-166, 2007.
- [21] R. F. Probstein, *Physicochemical Hydrodynamics- An Introduction, 2nd Ed*, John Wiley & Sons, 1994.
- [22] A.-S. Rollier, B. Legrand, D. Collard and L. Buchailot, "The stability and pull-in voltage of electrostatic parallel-plate actuators in liquid solutions," *Journal of Micromechanics and Microengineering*, vol. 16, pp. 794-801, 2006.
- [23] M. Gad-el-Hak, *The MEMS Handbook*, CRC Press, 2002.
- [24] P.-C. Hsu, C. H. Mastrangelo and K. D. Wise, "A high sensitivity polysilicon diaphragm condenser microphone," in *Proceedings of IEEE: 11th International Conference on Micro Electro Mechanical Systems (MEMS)*, Heidelberg, Germany, pp. 580-585, 1998.

- [25] C. H. Mastrangelo, "Adhesion-related failure mechanism in micromechanical devices," *Tribology Letters*, vol. 3, pp. 223-237, 1997
- [26] Dow Corning® WL-5150 and WL-5351 product information.
- [27] C.-W. Baek, Y.-K. Kim, Y. Ahn and Y.-H. Kim, "Measurement of the mechanical properties of electroplated gold thin films using micromachined beam structures," *Sensors and Actuators A*, vol. 117, pp. 17-27, 2005.
- [28] R. Maboudian and R. Howe, "Critical review: adhesion in surface micromechanical structures", *Journal of Vacuum Science and Technology*, vol. 15, pp. 1-20, 1997.
- [29] Meng-Ping Chang, Tushar Bansal, and Michel M. Maharbiz, "Electrically-actuated PDMS microvalves and pumps for VLSI microfluidics," in *Proceedings of Eleventh International Conference on Miniaturized Systems for Chemistry and Life Sciences (MicroTAS)*, Paris, France, October 2007.
- [30] J. Xie, J. Shih, Q. Lin, B. Yang and Y.-C. Tai, "Surface micromachined electrostatically actuated micro peristaltic pump," *Lab on a Chip*, vol. 4, pp. 495-501, 2004.
- [31] R. Rathnasingham, D. R. Kipke, S. C. Bledsoe, J. D. McLaren, "Characterization of implantable microfabricated fluid delivery devices," *IEEE Transactions on Biomedical Engineering*, Vol 51, pp. 138-145, 2004.
- [32] D. R. Reyes, D. Iossifidis, P.-A. Auroux, and A. Manz, "Micro Total Analysis Systems. 1. Introduction, Theory, and Technology," *Analytical Chemistry*, vol. 74, pp. 2623-2636, 2002.
- [33] S. J. Lee and S. Y. Lee, "Micro total analysis system (μ -TAS) in biotechnology," *Applied Microbiology and Biotechnology*, vol. 64, pp. 289-299, 2004.
- [34] M.G. Pollack, A.D. Shendorov and R.B. Fair, "Electrowetting-based actuation of droplets for integrated microfluidics," *Lab on a Chip*, vol. 2, pp. 96-101, 2002.
- [35] Sung K. Cho, H. Moon and C.-J. Kim, "Creating, transporting, cutting, and merging liquid droplets by electrowetting-based actuation for digital microfluidic circuits," *ASME/IEEE Journal of Microelectromechanical Systems*, vol. 12, pp. 70-80, 2003.
- [36] W. Gu, X. Zhu, N. Futai, B. S. Cho and S. Takayama, "Computerized microfluidic cell culture using elastomeric channels and Braille displays" in *Proceedings of National Academy of Science (USA)*, vol. 101, pp. 15861-15866, 2004.
- [37] A. S. Basu and Y. B. Gianchandani, "A 128-bit digitally programmable microfluidic platform for non-contact droplet actuation using Marangoni flows," in *Proceedings of International Conference on Sensors, Actuators, and Microsystems (Transducers)*, Lyon, France, pp. 771-774, June 2007.

- [38] H. Takao, K. Miyamura, H. Ebi, M. Ashiki, K. Sawada and K. Ishida, "A MEMS microvalve with PDMS diaphragm and two-chamber configuration of thermo-pneumatic actuator for integrated blood test system on silicon," *Sensors Actuators A*, vol. 119, pp. 468-475, 2005.
- [39] B. Bae, H. Kee, S. Kim, Y. Lee, T. Sim, Y. Kim and K. Park, "In vitro experiment of the pressure regulating valve for a glaucoma implant," *Journal of Micromechanics and Microengineering*, vol. 13, pp. 613-619, 2003.
- [40] P. Shao, Z. Rummeler and W. K. Schomburg, "Polymer micro piezo valve with a small dead volume," *Journal of Micromechanics and Microengineering*, vol. 14, pp. 305-309, 2004.
- [41] E. Meng, X.-Q. Wang, H. Mak and Y.-C. Tai, "A check-valved silicone diaphragm pump," in *Proceedings of IEEE: 13th International Conference on Micro Electro Mechanical Systems (MEMS)*, Miyazaki, Japan, pp. 62-67, January, 2000.
- [42] <http://www.merriam-webster.com/dictionary/valve>
- [43] S. C. Terry, J. H. Jerman and J. B. Angel, "A gas chromatographic air analyzer fabricated on a silicon wafer," *IEEE Transactions on Electron Devices*, vol. ED-26, pp. 1880-1887, 1979.
- [44] A. Brask, "Electroosmotic Micropumps," Ph.D dissertation, Technical University of Denmark, 2005.
- [45] H. Takao and M. Ishida "Microfluidic integrated circuits for signal processing using analogous relationship between pneumatic microvalve and MOSFET," *ASME/IEEE Journal of Microelectromechanical Systems*, vol. 12, pp. 497-505, 2003.
- [46] M. Esashi, "Silicon micromachining for integrated microsystems," *Vacuum*, vol. 47 pp. 469-474, 1996.
- [47] A. Luque, J. M. Quero, C. Hibert, P. Fluckiger, and A. M. Ganan-Calvo, "Integrable silicon microfluidic valve with pneumatic actuation," *Sensors and Actuators A*, vol. 118, pp. 144-151, 2005.
- [48] T. Ohori, S. Shoji, K. Miura and A. Yotsumoto, "Partly disposable three-way microvalve for a medical micro total analysis system," *Sensors and Actuators A*, vol. 64, pp. 57-62, 1998.
- [49] J. S. Go and S. Shoji S, "A disposable, dead volume-free and leak-free in-plane PDMS microvalve," *Sensors and Actuators A*, vol. 114, pp. 438-444, 2004.
- [50] S. Lee, W. Jeong and D. J. Beebe, "Microfluidic valve with cored glass microneedle for microinjection," *Lab on a Chip*, vol. 3, pp. 164-167, 2003.

- [51] J. Y. Baek, J. Y. Park, J. I. Ju, T. S. Lee and S. H. Lee, "A pneumatically controllable flexible and polymeric microfluidic valve fabricated via *in situ* development," *Journal of Micromechanics and Microengineering*, vol. 15, pp. 1015-1020, 2005.
- [52] K. Hosokawa and R. Maeda, "A pneumatically-actuated three-way microvalve fabricated with polydimethylsiloxane using the membrane transfer technique," *Journal of Micromechanics and Microengineering*, vol. 10, pp. 415-420, 2000.
- [53] E. T. Lagally, P. C. Simpson and R. A. Mathies, "Monolithic integrated microfluidic DNA amplification and capillary electrophoresis analysis system," *Sensors and Actuators B*, vol. 63, pp. 138-146, 2000.
- [54] M. T. Taylor, P. Nguyen, J. Ching and K. E. Petersen, "Simulation of microfluidic pumping in a genomic DNA blood-processing cassette," *Journal of Micromechanics and Microengineering*, vol. 13, pp. 201-208, 2003.
- [55] P. K. Yuen, L. J. Kricka and P. Wilding, "Semi-disposable microvalves for use with microfabricated devices or microchips," *Journal of Micromechanics and Microengineering*, vol. 10, pp. 401-409, 2000.
- [56] D. Baechi, R. Buser and J. Dual, "A high density microchannel network with integrated valves and photodiodes," *Sensors and Actuators A*, vol. 95, pp. 77-83, 2002.
- [57] J.-H. Kim, K.-H. Na, C. J. Kang, D. Jeon and Y.-S. Kim, "A disposable thermopneumatic-actuated microvalve stacked with PDMS layers and ITO-coated glass," *Microelectronic Engineering*, vol. 73-74, pp. 864-869, 2004.
- [58] K. W. Oh, R. Rong and C. H. Ahn, "Miniaturization of pinch-type valves and pumps for practical micro total analysis system integration," *Journal of Micromechanics and Microengineering*, vol. 15, pp. 2449-2455, 2005.
- [59] K. Yanagisawa, H. Kuwano and A. Tapo, "An electromagnetically driven microvalve," in *Proceedings of International Conference on Sensors, Actuators, and Microsystems (Transducers)*, pp. 102-105, 1993.
- [60] J.-W. Choi, K. W. Oh, A. Han, C. A. Wijayawardhana, C. Lannes, S. Bhansali, K. T. Schlueter, W. R. Heineman, H. B. Halsal, J. H. Nevin, A. J. Helmicki, H. T. Henderson, and C. H. Ahn, "Development and characterization of microfluidic devices and systems for magnetic bead-based biochemical detection," *Biomedical Microdevices*, vol. 3, pp. 191-200, 2001.
- [61] M. Shikida, K. Sato, S. Tanaka, Y. Kawamura and Y. Fujisaki, "Electrostatically driven gas valve with high conductance," *ASME/IEEE Journal of Microelectromechanical Systems*, vol. 3, pp. 76-80, 1994.
- [62] K. W. Oh, R. Rong and C. H. Ahn, "In-line micro ball valve through polymer tubing," in *Proceedings of 5th International Conference on Miniaturized Systems for Chemistry and Life Sciences (MicroTAS)*, Monterey, CA, USA, pp. 407-408, 2001.

- [63] C. Fu, Z. Rumlmer and W. Chomburg, "Magnetically driven micro ball valves fabricated by multilayer adhesive film bonding," *Journal of Micromechanics and Microengineering*, vol. 13, pp. S96-S102, 2003.
- [64] A. Meckes, J. Behrens, O. Kayser, W. Benecke, T. Becker and G. Muller, "Microfluidic system for the integration and cyclic operation of gas sensors," *Sensors and Actuators A*, vol. 76, pp. 478-483, 1999.
- [65] M. Stehr, S. Messner, H. Sandmaier and R. Zengerle, "The VAMP—a new device for handling liquids or gases," *Sensors and Actuators A*, vol. 57, pp. 153-157, 1996.
- [66] C. E. Tamanaha, L. J. Whitman and R. J. Colton, "Hybrid macro–micro fluidics system for a chip-based biosensor," *Journal of Micromechanics and Microengineering*, vol. 12, pp. N7-N17, 2002.
- [67] K. W. Oh and C. H. Ahn, "A review of microvalves," *Journal of Micromechanics and Microengineering*, vol. 16, pp. R13-R39, 2006.
- [68] D. F. Herrick, *Media Management in the Age of Giants: Business Dynamics of Journalism*, Blackwell Publishing, 2003.
- [69] A. R. Wheeler, H. Moon, C.-J. Kim, J. A. Loo, R. L. Garrell, "Electrowetting-based microfluidics for analysis of peptides and proteins by matrix-assisted laser desorption/ionization mass spectrometry," *Analytical Chemistry*, vol. 76, pp. 4833-4838, 2004.
- [70] <http://www.merriam-webster.com/dictionary/pump>
- [71] J. G. Smits, "Piezoelectric micropump with 3 valves working peristaltically," *Sensors and Actuators A*, vol. 21, pp. 203–206, 1990.
- [72] D. J. Laser and J. G. Santiago, "A review of micropumps," *Journal of Micromechanics and Microengineering*, vol. 14, pp. R35-R64, 2004.
- [73] J. M. Berg, R. Andersona, M. Anayaa, B. Lahlouhb, M. Holtzb and T. Dallas, "A two-stage discrete peristaltic micropump," *Sensors and Actuators A*, vol. 104, pp. 6-10, 2003.
- [74] A. Wego and L. Pagel, "A self-filling micropump based on PCB technology," *Sensors and Actuators A*, vol. 88, pp. 220–226, 2001.
- [75] W. K. Schomburg, J. Vollmer, B. Bustgens, J. Fahrenberg, H. Hein and W. Menz, "Microfluidic components in LIGA technique," *Journal of Micromechanics and Microengineering*, vol. 4, pp. 186–91, 1994.
- [76] H. J. Yoon, W. Y. Sim and S. S. Yang, "The fabrication and test of a phase-change micropump," in *Proceedings of ASME International Mechanical Engineering Congress and Exposition*, New York, New York, USA, November 2001.

- [77] C. Grosjean and Y. C. Tai, "A thermopneumatic peristaltic micropump," in *Proceedings of International Conference on Sensors, Actuators, and Microsystems (Transducers)*, Sendai, Japan, 1999.
- [78] S. Boehm, W. Olthuis and P. Bergveld, "A plastic micropump constructed with conventional techniques and materials," *Sensors and Actuators A*, vol. 77, pp. 223–228, 1999.
- [79] K.-S. Yun, I.-J. Cho, J.-U. Bu, C.-J. Kim and E. Yoon, "A surface-tension driven micropump for low-voltage and low-power operations," *ASME/IEEE Journal of Microelectromechanical Systems*, vol. 11, pp. 454–461, 2002.
- [80] S. Shoji and M. Esashi, "Microflow devices and systems," *Journal of Micromechanics and Microengineering*, vol. 4, pp. 157–171, 1994.
- [81] N. Nguyen, X. Huang and T. K. Chuan, "MEMS-micropumps: a review," *Journal of Fluids Engineering*, vol. 124, pp. 384-392, 2002.
- [82] P. Woias, "Micropumps – summarizing the first two decades," in *Proceeding of SPIE*, vol. 4560, pp. 39-52, 2001.
- [83] Y. Xia and G. M. Whitesides, "Soft lithography," *Annual Review of Materials Science*, vol. 28, pp. 153-184, 1998.
- [84] P.-Y. Chiou, Z. Chang and M. C. Wu, "Droplet manipulation with light on optoelectrowetting device," *ASME/IEEE Journal of Microelectromechanical Systems*, vol. 17, pp. 133-138, 2008.
- [85] T.-T. Wu and M.-P. Chang, "Surface waves in layered piezoelectric medium loaded with viscous liquid", *Japanese Journal of Applied Physics*, vol. 41, pp. 5451-5457, 2002.
- [86] P. M. Osterberg and S. D. Senturia, "M-TEST: A test chip for MEMS material property measurement using electrostatically actuated test structures," *ASME/IEEE Journal of Microelectromechanical Systems*, vol. 6, pp. 107–118, 1997.
- [87] R. T. Borno, J. D. Steinmeyer and M. M. Maharbiz, "Transpiration actuation: the design, fabrication, and characterization of biomimetic microactuators driven by the surface tension of water," *Journal of Micromechanics and Microengineering*, vol. 16, pp. 2375-2383, 2006.
- [88] Salil P. Desai, Brian M. Taff and Joel Voldman, "A photopatternable silicone for BIOMEMS applications," in *Proceedings of Eleventh International Conference on Miniaturized Systems for Chemistry and Life Sciences (MicroTAS)*, Paris, France, October 2007.
- [89] Antony D. Clegg, Neil V. Rees, Oleksiy V. Klymenko, Barry A. Coles and Richard G. Compton, "Marcus theory of outer-sphere heterogeneous electron transfer reac-

tions: High precision steady-state measurements of the standard electrochemical rate constant for ferrocene derivatives in alkyl cyanide solvents," *Journal of Electroanalytical Chemistry*, vol. 580, pp. 78-86, 2005.

- [90] G. E. Nyfors, "Method for measuring properties of flowing fluids, and a metering device and a sensor used for performing this method," U.S. Patent 6,826,964, Dec. 7, 2004.
- [91] Ruba T. Borno, Ph.D. Thesis, University of Michigan, 2008.
- [92] E. Pasero, M. Riccardi, T. B. Meindl, "Multi-frequency capacitive measurement device and a method of operating the same," U.S. Patent 7,205,780, Apr. 17, 2007.